Porous Silicon Nanowires for Hydrogen Generation: Mechanism and Photocatalytic Studies

Dissertation

zur Erlangung des akademischen Grades doctor rerum naturalium
(Dr. rer. nat)

vorgelegt dem Rat der Chemisch-Geowissenschaftlichen Fakultät

der Friedrich-Schiller-Universität Jena

von Master of Science Tingsen Ming

geboren am 25.12.1982 in Hubei, China

Gutachter:

1. Prof. Dr. Benjamin Dietzek / Friedrich-Schiller-Universität Jena

2. Prof. Dr. Dr. (h.c.) Sanjay Mathur / Universität zu Köln

Tag der öffentlichen Verteidigung: March 04, 2020

Table of Content

1. Introduction

1.1 Motivation

Energy has become an important topic with the increasing reliance on non-renewable traditional fossil fuels, such as petroleum, coal, etc. [1] Primary energy consumption in the world in 2050 will be more than double than in 2013. [2] Moreover, carbon-based fuels currently supply nearly 80% of the energy in the world, which causes great damage to the environment. For these reasons, solar energy utilization has become a research hotspot due to its inexhaustible energy source including converting solar energy into, *e.g.* chemical fuels such as hydrogen electricity in photovoltaics, or degradation of organic pollutants. [3-5]

Hydrogen as high combustion fuel can effectively alleviate the energy issue. [6] Differently from carbon-based fuels, the combustion product of hydrogen is water. Therefore, hydrogen is an ideal fuel to replace traditional fossil fuels such as coal, oil and natural gas. Also, hydrogen can be used in furnaces, internal combustion engines, turbines, and jet engines. Fuel cell vehicles as an emerging vehicle that generally use oxygen from the air and compressed hydrogen to power the motor, emit only water and heat. [7] At present, the main industrial method for the production of hydrogen is a catalytic steam-hydrocarbon process, in which gaseous or vaporized hydrocarbons are treated with steam at high pressure over a nickel catalyst at 650-950 ºC to produce carbon oxides and hydrogen.

$$CH_4 + H_2O \longrightarrow CO + 3H_2 \qquad (1)$$

$$CO + H_2O \longrightarrow CO_2 + H_2 \qquad (2)$$

In this process, toxic gases CO and CO_2 are also produced with H_2, which are harmful to the environment. Electrolysis of water is another important method used in industry to produce hydrogen. However, this method consumes huge amounts of electric energy. Hence, to find an environmentally friendly, cheap and efficient method to produce hydrogen is important and meaningful. Utilizing solar energy and photocatalysis to produce hydrogen has attracted a growing interest recently because it does not consume any carbon-based fossil fuels and emits zero toxic gases. Therefore, the implementation of photocatalysis processes to generate “green” hydrogen has gained an enormously growing interest in research.

A lot of photocatalysts, to this time, for hydrogen generation have been proposed, however, they still can't be implemented in mass production due to the low photocatalytic efficiencies. Most of the currently used photocatalysts can only absorb ultraviolet light due to the wide bandgap semiconductor nature. Ultraviolet light contributes about 10% of the total solar energy, while in comparison, visible light contributes about 45-50%.[8] Hence, the developing of photocatalysts in response to visible light is an important topic. Although a lot of development for adjusting the bandgap structure of the photocatalyst has been realized to harvest visible light, there is still a long way to go to produce hydrogen at an industrial level. Another important issue is the chemical stability of photocatalysts. Chemical compounds in the solution can influence the chemical compositions and structure of the photocatalyst and reduce the photocatalytic efficiency. Therefore, photocatalysts should be stable in various acid and/or alkali conditions which will allow the production of hydrogen continuously. Based on the before mentioned milestones, the main aims of this thesis are:

1. To evaluate the silicon nanowire arrays as an efficient surface for hydrogen generation.
2. To find a strategy to enhance hydrogen generation and stability in water-based solutions.
3. To investigate the mechanism of hydrogen generation based on silicon nanowires.

1.2 Background of photocatalysis

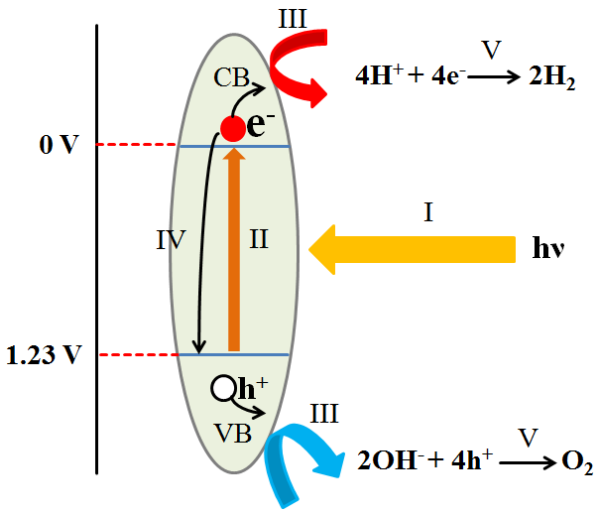

Figure 1.1 Schematical representation of solar water splitting process using a semiconductor as photocatalyst.

The schematical representation of solar water splitting by a photocatalyst is shown in Figure 1.1. There are five main processes occurring during the water splitting of the photocatalysis: (I) light absorption, (II) electron and hole generation, (III) electron and hole separation, (IV) electron and hole recombination and (V) oxidation and reduction (redox) reactions. When a semiconductor absorbs the photons with energy greater than the bandgap energy (Eg), electrons are excited to the conduction band, generating the holes in the valence band. The separated electrons and holes then migrate through the semiconductor to the semiconductor/electrolyte interface, where redox reactions to generate hydrogen and oxygen. However, not all the photo-generated charge carriers can be collected and finally contribute to the fuel generation. In fact, a portion of the photo-generated charge carriers is subjected to the recombination in the bulk and at the surface, dissipating their energy thermally by the creation of phonons and heat. Charge recombination is believed to be a major loss of the excited charge carriers and a critical factor that limits the solar-to-chemical energy conversion efficiency for semiconductor photocatalysts. The important requirement for an effective water spitting is that the photon energy (system excitation energy) should be higher than the bandgap (E_g) of the semiconductor, [9] as water reduction requires the bottom of the conduction band (CB) to be more negative than the redox potential of H^+/H_2 (0 V, vs. NHE pH 0). Simultaneously, holes can oxidize the water to form O_2 if the top level of the valence band (VB) is more positive than the redox potential of O_2/H_2O (1.23 V, vs. NHE pH 0). [10] It is worth mentioning that considering the energy loss of conversion from solar energy to photocatalyst, the energy of splitting water is increased 1.23 eV to 2.0-2.2 eV. [11] Even for an ideal system, U_{loss} (the actual energy loss per molecule in the overall conversion process) cannot go to zero because, as noted above, the energy of the ensemble of excited states is thermodynamically internal energy and not Gibbs energy. Entropic considerations dictate that U_{loss} has a minimum value of 0.3-0.4 eV, depending on the value of U (total energy). In real systems, U_{loss} will be considerably higher. It means that photon energy should be at least 1.6 eV in idealistic case, but in realistic systems, a reasonable estimate of U_{loss} is 0.8-1 eV.

There are two ways to split water to produce hydrogen by applying a photocatalysis process: direct photocatalysis and photoelectrochemical cell (PEC). For direct photocatalysis, photocatalysts split water directly under light without any additional energy, except solar. For PEC hydrogen generation approach, a photoanode in PEC cell is playing an important role by water molecule splitting and PEC system is required additional energy input, which can be “green energy” like PV generate solar (solar to hydrogen transformation) energy or other

conventional energy sources. Usually, a bias voltage in PEC is applied to increase the yield of water splitting.

The schematic model of splitting water directly using a photocatalyst is shown in Figure 1.2. The photocatalysts are dispersed in a pool with water and irradiated under sunlight or simulated sunlight, hole and electrons are generated under the light. Photo-generated electrons reduce water to produce hydrogen. On the other hand, water molecular is oxidized by photo-generated holes to form oxygen. The processes of direct water splitting by photocatalyst are shown in Figure 1.1.

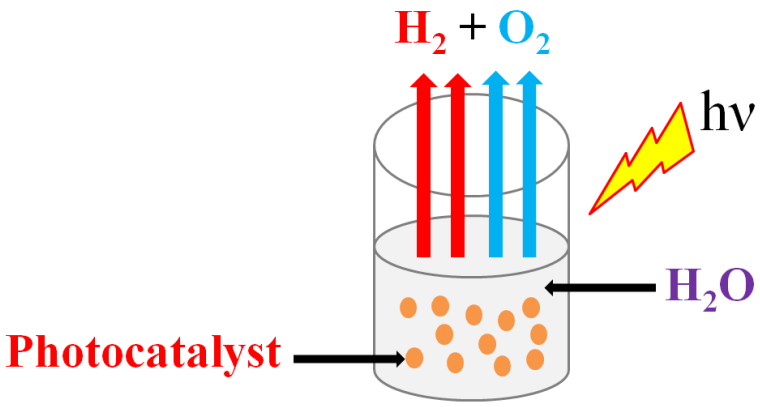

Figure 1.2 Schematic representation of water splitting during direct photocatalysis.

Since Honda and Fujishima have reported water splitting using a TiO_2 electrode in 1970, [12] numerous researchers started to investigate PEC catalytic water splitting. Titanium oxide (TiO_2) as a typical semiconductor photocatalyst was widely reported in the application of PEC water splitting due to the wide bandgap (3.2 eV). [13] However, the absorption of TiO_2 in visible region is very limited, while it strongly absorbs in the ultraviolet region where the solar photon flux is weaker in comparison to the visible spectral region. In PEC catalytic water splitting, a semiconductor electrode (e.g. TiO_2) is used as photoanode, and the counter electrode is the cathode. When the photoanode is irradiated electrons and holes are generated and form a circuit. The photo-generated electrons reduce water to form H_2 on counter electrode while photo-generated holes oxidize water to form O_2 on the photoanode with some external bias by a power supply or difference pH between a catholyte and an anolyte. The schematic representation of PEC water splitting is shown in Figure 1.3.

External bias in PEC promotes the separation of photo-generated electrons-holes. Hydrogen and oxygen are generated on the counter electrode and photoanode, respectively. Therefore, PEC can split water efficiently. However, this system is complicated and expensive.

Comparing direct photocatalysis and PEC, the first approach is very simple and cheap. hydrogen and oxygen can be separated by liquefaction at low temperatures. Considering the potential application in industry, direct photocatalysis is more promising from economical view, but most limitations are related to the higher recombination of photo-generated electrons-holes and weak photocatalyst light absorption in a visible spectral region.

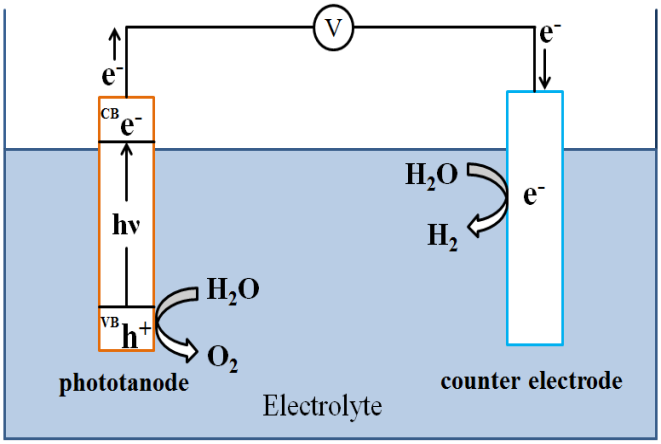

Figure 1.3 Schematic representation of water splitting by PEC.

1.3 Photocatalyst design

As discussed above, the electronic structure of semiconductor photocatalyst is important to split a water molecule. Figure 1.4 shows the band structure of various semiconductor materials regarding the redox potentials (NHE) for water oxidation and reduction. [14] In Figure 1.4 it is clearly visible that the band structure of $KTaO_3$, $SrTiO_3$, TiO_2, ZnS, CdS and SiC fulfill the requirements for overall water splitting. However, these semiconductors can only be activated in UV region which is corresponded only to 10% of total solar energy. Another essential requirement for the photocatalyst is the stability in the water-based media. Some semiconductor photocatalysts can react with water and result in themselves degradation (due to dissolution). For example, S^{2-} in CdS rather than H_2O is oxidized by photo-generated holes. [15] This reaction is called as "photocorrosion" and a disadvantage of a metal sulfide photocatalyst. From this point-of-view, CdS and ZnS are not good photocatalysts for water splitting as. The band gaps of CdSe and Si show that they can be activated by visible light but due to the valence band energy position (to negative), only the generation of hydrogen is energetically suitable. CdSe similar to CdS is also not stable in water due to the photocorrosion effect.[16] Bulk Si has a narrow bandgap, which denotes that the recombination of photo-generated electrons and holes is high and the efficiency of

photocatalysis is low. Some semiconductors like WO_3, Fe_2O_3, etc. can only produce oxygen because the position of CB is more positive than 0 V.

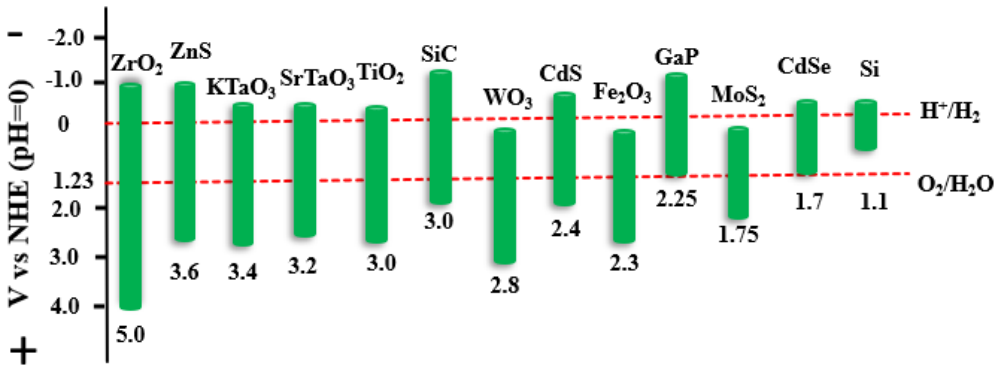

Figure 1.4 Band structures of semiconductors and redox potentials of water splitting.

For these reasons, it is difficult to find ideal photocatalyst which can satisfy all requirements for water splitting in the visible spectral range. Currently, modification of photocatalytic materials is the main way to develop efficient photocatalysts for water splitting, which involves the electronic structure, microstructure, and surface properties of photocatalysts. The main methods to increase efficiency of photocatalysts for water splitting are (1) changing the bandgap of photocatalysts that can only be activated in UV light to response visible light; (2) surface modification of photocatalysts by deposition of co-catalysts or noble metal (second reaction center) promotes more effective charge carriers separation; (3) suppression of photogenerated electrons and holes recombination; (4) sensitization; (5) shrinking the size of photocatalysts to nanoscale.

Tuning of the photocatalyst band gap can utilize the highest proportion of visible photons. Doping is a common method to decrease the wide bandgap photocatalysts. For examples, partly replaced Ti^{4+} in TiO_2 crystal lattice by phosphorus cations (P^{5+}) narrows the bandgap of TiO_2. [17] Platinum-doped α-Fe_2O_3 exhibits better electron conductivity and lower bandgap. [18]

Noble metal (Ag, Au, etc.) nanoparticles decorated photocatalyst has been investigated. [19-21] Noble metal nanoparticles exhibit strong ultraviolet and visible light absorption due to their surface plasmon resonance (SPR), which is produced by the collective oscillations of surface electrons. [22-23] Also, noble metal nanoparticles can capture the photogenerated electrons and reduce the recombination of photogenerated electrons-holes. [24] The metal nanoparticles can play as relay stations to transfer generated photoelectrons to reduce a water molecule. [25] Noble metal also affects the efficiency of charge separation. Nakibli et al. reported that for Ni

decorated CdSe@CdS nanorods, charge moved slowly along the rod toward the interface, but quickly from the interface of the semiconductor to the metal phase. [26]

The surfactants can also suppress the recombination process in the system and improve hydrogen or oxygen production. The methanol or ethanol is a common surfactant that can be employed as hole scavengers (i.e., as electron donors) to produce hydrogen from water. [27] The methanol or ethanol can be oxidized by photogenerated holes and enhance the photogenerated electron-hole separation efficiency. [28] Due to the oxidation of surfactant, the oxygen generation in the system is suppressed. On the other hand, Ag^{+} or Fe^{3+} is employed as electron acceptors to enhance oxygen production. Ag^{+} or Fe^{3+} is reduced by photogenerated electrons and suppresses hydrogen generation. [29-30]

Organic dye sensitization is another method to increase the hydrogen generation. The chromophore, such as an organic dye, is activated under visible light and injects electrons into the CB of a photocatalyst to produce hydrogen by reducing water. But the problem is only the first monolayer of adsorbed dye can efficiently inject electrons into the semiconductor and the light-harvesting efficiency of a single dye monolayer is very weak. [31]

Nanosized photocatalysts have been attracting large interest in recent years as a very promising nanostructure due to their peculiar optical, electrical, surface, etc. properties. For example, silicon nanowires (SiNWs) exhibit a direct bandgap that increases as the wire diameter narrows. [32] Water splitting reaction occurs when charge carriers (electrons and holes) are generated and move to the surface of photocatalyst during their lifetime. For this reason, reducing the recombination of photogenerated carriers is essential to enhance the efficiency of the photocatalyst. The transport of photogenerated carriers is determined by the crystal size, the crystalline structure, the structural defects, and the surface properties of photocatalysts. [33-36] For these reasons, the nanosized photocatalyst is considered as an important approach to improve the photocatalytic activity of the selected system.

1.4 Bulk silicon peculiarities

Silicon is the second most abundant element on the Earth, about 95% of the earth's crustal rocks are made of silica or silicate and aluminosilicate minerals. Moreover, silicon is the most important semiconductor material that is widely used in the diode, transistor, integrated circuit, solar cell, high-temperature resistant materials, etc. The silicon-based technologies are

certainly favored because of material abundance and non-toxicity at a high level of materials control and understanding together with a huge industrial infrastructure to account for low production/processing costs and high production yields. Before discussing the application of silicon in hydrogen generation, it is necessary to clarify the basic characters of silicon as a possible photocatalyst.

Silicon can be divided into crystalline silicon (c-Si) and amorphous silicon (a-Si) ones. c-Si is a crystalline form of silicon. Silicon combines four neighboring silicon atoms by the covalent bond and forms tetrahedral. In c-Si this tetrahedral structure continues over a large range, thus forming a well-ordered crystal lattice. In a-Si, this long-range order is not present. Therefore, the atoms form a continuous random network.

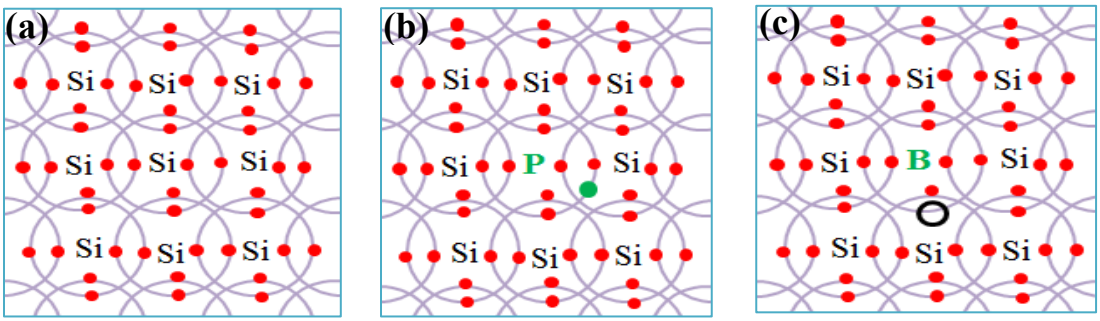

Figure 1.5 Schematic diagram showing valence electrons of (a) silicon intrinsic semiconductor; (b) n-type and (c) p-type silicon semiconductors.

Silicon belongs to group IV of the periodic elements table that each atom has four valence electrons. In the crystalline form, each silicon atom shares an electron with a neighboring silicon atom. In this state, it is silicon intrinsic semiconductor (*fig. 1.5*a). Elements that belong to group V of the periodic elements table such as arsenic (As), phosphorus (P), stibium (Sb) have five electrons in the valence band. When such elements are doped into intrinsic silicon crystal as dopant, four valence electrons of dopants combine with ever one silicon atom and the fifth electron is free to move and serves as a charge carrier. The dopant atom (e.g. phosphorus) contributes an additional electron to the crystal (*fig. 1.5*b). Dopants that emit an electron to the crystal are known as donors and the semiconductor material is called n-type because it creates negative charge carries. On the other hand, elements in group ⅢA, such as boron (B), aluminum (Al), indium (In), gallium (Ga) have three electrons in the valence band. When a silicon atom is replaced by an atom of these elements (e.g. boron) into the crystal, the dopant atom has an insufficient number of electrons to form stable covalent

bonds with the surrounding silicon atoms. As a result, one of the silicon atoms has a vacancy for an electron (*fig. 1.5*c). Dopants that create holes in this way are known as acceptors. This type of extrinsic semiconductor is known as p-type as it creates positive charge carriers.

The concentration of dopant affects many electrical properties of Si. The most important effect is the charge carrier concentration. In general, increasing doping levels leads to higher conductivity (or lower resistivity) due to the higher concentration of carriers. Dopants also can affect the band structure of the semiconductor. For n-doped semiconductors, there are free electrons in the silicon crystal which are not bound and the energy level of the donor is located close to the conduction band, electrons at this energy level are easily excited to the conduction band and contribute to the conductivity. For p-doped semiconductors, acceptor dopants have the property of capturing electrons from the dopant center becomes negatively charged while holes appear in the valence band. [37] The energy level of the acceptor is close to the valence band. Since there are no electrons here, electrons in the valence band are excited. As a result, holes are formed in the valence band, which contributes to the conductivity (*fig. 1.6*). Another effect of dopant is the shift of Fermi energy (E_f). Fermi level refers to the chemical potential of the fermions system when it reaches absolute zero. But in the field of semiconductor physics and electronics, the Fermi level is often used as a synonym for electron or hole chemical potential. For intrinsic silicon, the Fermi energy is in the middle of bandgap. However, an n-type silicon Fermi energy shifts toward conduction band while it moves to valence band in p-type silicon (*fig. 1.6*).

Intrinsic semiconductor silicon exhibits very poor conductivity at room temperature. Currently, almost every commercial Si-wafer is doped with boron, phosphorus or other elements to improve the electrical properties and conductivity.

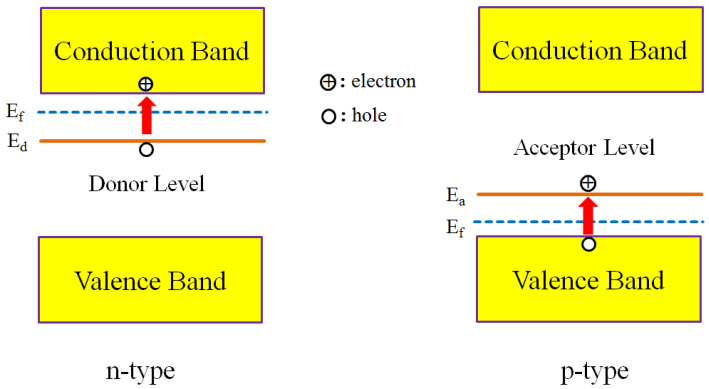

Figure 1.6 Band diagram of the doped semiconductor.

1.5 Silicon nanostructures: top-down and bottom-up approaches

Vertically aligned SiNWs can be fabricated by "bottom-up" and "top-down" approaches. Vapor-liquid-solid (VLS) crystal growth approach is a typical "bottom-up" way to produce SiNWs. Wagner and Ellis initially explain the mechanism of VLS for SiNWs growth in the early 60s of the last century. [38] In VLS to produce SiNWs, catalytical metal (Au, Fe, Ni, etc.) are deposited on the silicon surface and formed as liquid alloy droplet at metal-silicon eutectic temperature (for example, about 373 ºC for Au). [39] Then the precursor gases containing silicon atoms (for example, SiH_4) are introduced to the reaction chamber and the gases adsorb onto the liquid surface, the silane decomposition elemental silicon and hydrogen take place and silicon atoms diffuse into the droplet. When the eutectic droplet is supersaturated with silicon atoms, silicon crystal growth can subsequently occur from nucleated seeds at the liquid-solid interface. [40] SiNWs are usually grown by VLS utilizing chemical vapor deposition (CVD), [41] pulsed laser deposition (PLD), [42] electrochemical deposition [43] or vapor transport at high pressures and temperatures. [44]

For VLS grown SiNWs the additional important question arises where and how much metal catalyst from the eutectic droplet, which initiates the VLS wire growth, resides in the nanowire. However, the enormous impact that even smallest concentrations of gold atoms as a dopant in semiconductor, especially in silicon material, have a huge influence on optoelectronic properties of the SiNWs makes it essential to understand the extent to which Au atoms diffuse in the SiNW and Si (111) substrate and stay incorporated there and on the SiNW surfaces. [45] Essentially after it has been shown that the Au from the catalyst is very mobile and diffuses all over the SiNW surfaces and between SiNWs at temperatures as low as 600°C, leading to Ostwald ripening process of Au nanoparticles at the nanowire sidewalls or even of the nanowire top Au droplet itself. [46-49] To summarize, VLS approach for silicon nanowires, gives high-quality nanowires but requires the implementation of hazardous silane (SiH_4) gases or tetrachlorosilane at high temperature. [50-51] The use of radial or axial p-n hetero-junctions is highly limited due to the inhomogeneous dopant distribution inside the semiconductor material and metal catalyst contamination. [52] Also, it should be mentioned that no significant size effect (due to the quantum confinement) was reported for the SiNWs grown via a bottom-up approach.

Reactive ion etching (RIE) is a well-known "top-down" method to form 1D silicon nanostructures. [53] RIE is a type of dry chemical etching method to prepare SiNWs. RIE uses

chemically reactive plasma to remove material deposited on wafers. The plasma is generated under low pressure (vacuum) by an electromagnetic field. High-energy ions from the plasma attack the wafer surface and react with it. Although these methods are good to prepare SiNWs, however, they are too expensive to prepare SiNWs and need rigid control of experimental conditions, and realization of SiNWs with diameter near to the quantum confinement is limited.

The wet chemical etching (top-down approach) or electroless metal-assisted etching (MAE) has been gained interest recently due to its simplicity and versatility. [54] In recent years MAWCE method has attracted more and more interest. Firstly, MAWCE is a low cost and simple method comparing to VLS and RIE methods and it is easy to prepare various SiNWs with different parameters (e.g. length, diameter, and orientation). Secondly, the MAWCE method enables the formation of porous SiNWs with high surface-to-volume ratio structures, and the roughness surface depends on the doping level and type of silicon. Third, MAWCE method can prepare high quality of SiNWs without any catalyst contamination. MAWCE methods can be divided into a one-step and a two-step approach. [55, 56] In the one-step MAWCE process, the bulk silicon etching takes part in an aqueous etchant solution containing HF and metal salts (e.g. $AgNO_3$), but it was reported that lowly doped SiNWs cannot be reproducibly prepared by a one-step MAWCE approach. [57] From another side in the two-step MAWCE process, the AgNPs are firstly deposited on the surface of the silicon substrate then the etching of bulk silicon occurs in a mixture of diluted hydrofluoric acid (HF) and hydrogen peroxide (H_2O_2) [58] or ferric nitrate [$Fe(NO_3)_3$] [59] solutions.

Silicon nanoparticles (SiNPs) have also been reported as an efficient material for the hydrogen generation from the water-based solutions. [60, 61]. Silicon nanoparticles can be fabricated by gas-phase synthesis, [62] supercritical fluid method, [63] solid heating method, [64] liquid-phase synthetic approach, [65] laser pyrolysis of silane, [66] etc. However, the bandgap of SiNPs changes little comparing to silicon bulk (1.12 eV), [67] which means that the recombination of photogenerated photos and holes is still high and it is difficult to split water molecule to the elemental hydrogen and oxygen. For that reason the further application of silicon nanoparticles in the long-term view as a possible catalyst for hydrogen generation is limited. Also, it should be mentioned that to this time the most tendency for all materials is to be deposited or grown on the surface, just to avoid air pollution by the solid nanoparticles. This aspect is highly important for the modern community.

1.6 Background of metal-assisted wet-chemical etching technique

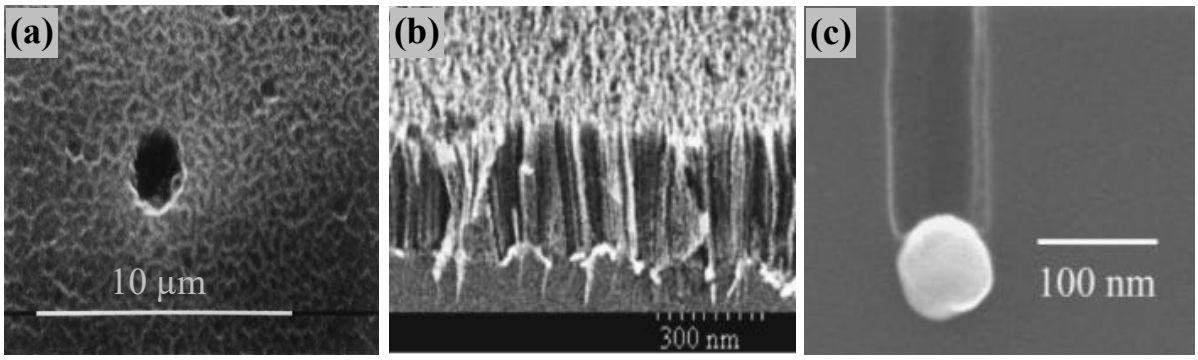

Figure 1.7 (a): SEM plan-view micrographs of a porous silicon layer formed by stain etching of Si (100) in HF: HNO_3: H_2O=1:3:5 solution for 3 min; [68] (b): SEM cross-sectional view of Au-coated Si (100) after etching in HF: H_2O_2: ethanol= (1:1:1) for 30s; [69] (c): cross-sectional view of Si (100) wafer loaded with Ag particles after etching for 30 min at a position about 40 µm from the surface. [70] (Supplement I)

MAWCE was firstly reported by Dimova-Malinovska et al. in 1997. A thin aluminum (Al) film was deposited on the silicon substrate and treated in hydrofluoric acid (HF), nitric acid (HNO_3) and H_2O (v/v/v, 1:3:5) solution after that a porous silicon layer was formed (*fig 1.7*a). [68] However, the SiNWs were not observed (*fig1.7* a). Li et al. have improved this method by

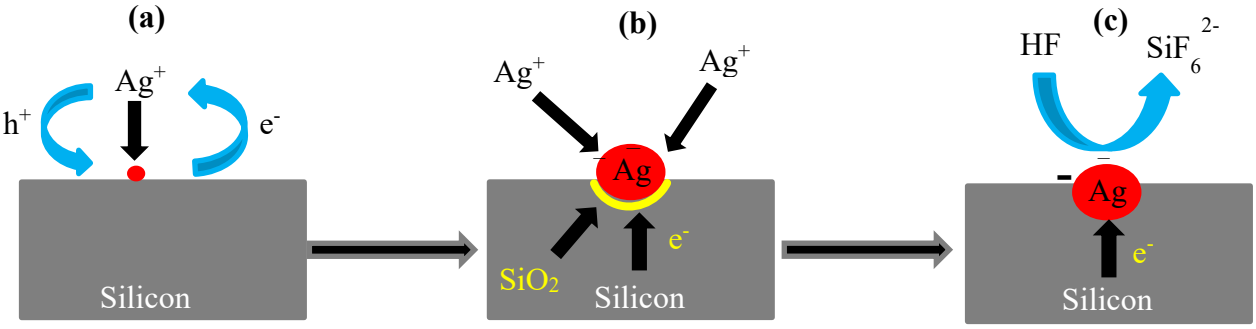

Figure 1.8 Schematically representation of one-step MAWCE method. (a) deposition of Ag seed; (b) growth of Ag seed and oxidation of Si at the interface; (c) Ag particle sink into the silicon substrate.

replacing Al film with a noble metal layer (e.g., Au, Pt) in HF, H_2O_2, and ethanol (v/v/v 1:1:1) solution. [69] The silicon surface was etched deeper and pores propagating anisotropically perpendicular to the surface as presented in Figure 1.7 b. Tsujino K et al. further improved this method by Ag deposition on the surface of silicon in a mixed solution of 10% HF and 30%

H_2O_2 (v/v 10:1) for 30 min in the darkness at room temperature. [70] In this literature, the Ag particles showed unique catalytic property could generate more straight cylindrical nanoholes than Pd, Pt particles (*fig 1.7* c). After that, this method was got more and more attention and development.

Figure 1.8 shows the mechanism of one-step MAWCE method to prepare SiNWs. Firstly, metal nanoparticles are deposited on the surface of the silicon substrate. This process is called "metal displacement". In this step, the silicon substrate captures holes from Ag^+ due to the electrochemical potential of Ag^+/Ag is more positive than the energy of the silicon valence band (E_{VB}). [71] Ag^+ ions are reduced to solid AgNPs (*fig 1.8* a).

$$Ag^+ + e^- = Ag,\ E^0 = 0.79\ V \qquad (1)$$

The holes that are injected into the valence band of Si substrate locally oxidize Si and form a SiO_2 layer between the interface of AgNPs and silicon substrate. SiO_2 layer is dissolved, simultaneously. The reactions are:

$$Si + 2H_2O = SiO_2 + 4H^+ + 4e^-,\ E^0 = 0.91\ V \qquad (2)$$

$$SiO_2 + 6HF = [SiF_6]^{2-} + 2H_2O + 2H^+ \qquad (3)$$

Overall reaction is

$$Si + 6HF^+ + 4Ag^+ = 4Ag + [SiF_6]^{2-} + 6H^+ \qquad (4)$$

This process is called one-step MAWCE method. SiO_2 is dissolved by HF (eq. 3), leading to the formation of pits underneath on the silicon surface to trap the Ag nuclei. The oxidation of one silicon atom donates four electrons, and the reduction of Ag^+ ion consumes only one electron. The excess electrons around Ag nuclei attract more and more Ag^+ and reduce Ag^+ to deposit on the surface of Ag nuclei. Thus, Ag nuclei become bigger with time (*fig 1.8* b). At the same time, because of the dissolution of SiO_2, Ag^+ continues to inject holes to oxidize silicon at the interface of AgNPs and silicon substrate. The etching process described in Eqs 1-3 occurs repeatedly, leading to that Ag particles sink into the silicon substrate (*fig.1.8 c*). It is worth to note that, the points on the surface of silicon are not exactly the same and nucleation preferentially occurs at surface defects sites around the dopants. [72] Thus, the etching rate is not the same and it finally leads to form SiNWs.

As discussed above, in one-step MAWCE method to prepare SiNWs, Ag^+ plays as driving force to etch silicon wafer. Indeed, one-step MAWCE method is reported to prepare SiNWs successfully. However, it is hard to prepare uniform SiNWs due to the growth of Ag nanoparticle and etching takes place at the same time. Moreover, because of the oxidation and dissolution only occur from beneath the AgNPs that are trapped in the formed pits, the AgNPs that do not enter the pits grow into silver grain film and cover the top of SiNWs. [73] Due to more and more Ag^+ ions are consumed, the capacity to capture electrons from silicon substrate become weaker, therefore, the etching rate is smaller. As reported in ref. 71, it took one hour to produce a 5μm length of SiNWs. However, it only needs 10 min to produce a 5μm length of SiNWs arrays by two-step MAWCE method.

$HF/H_2O_2/AgNO_3$ system of one-step method is reported to improve $HF/AgNO_3$ system. [74] In the $HF/H_2O_2/AgNO_3$ system, AgNPs are oxidized to be Ag^+ by H_2O_2 and lead to lateral etching to form porous SiNWs. However, as ref. 74 reported, only medially and lightly doped silicon can be used to prepare SiNWs.

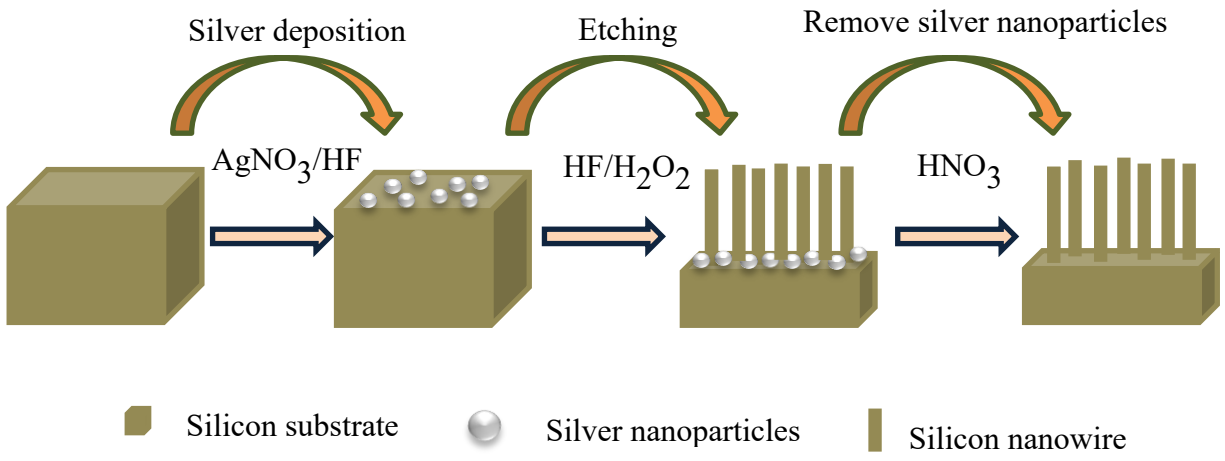

Figure 1.9 Schematic representation of two-step MAWCE to prepare SiNWs.

For these reasons, the two-step MAWCE method is preferred to prepare SiNWs. Generally, the process of two-step MAWCE method to prepare SiNWs can be described as follows (*Fig.1.9*): Firstly, the polished, single-crystal silicon substrate is immersed in the $AgNO_3/HF$ solution. AgNPs will deposit on the surface of the silicon wafer, similar to the one-step MAWCE process. Secondly, the silicon substrate is etched in HF/H_2O_2 solution. After etching, the SiNWs are formed and the AgNPs stay at the bottom of SiNWs. Finally, AgNPs are removed using concentrated HNO_3 (65%). SiNWs are oxidized in the concentrated HNO_3

and form SiO_2 layer on the surface of SiNWs. [75] SiO_2 layer can be removed by treatment with 2% HF solution.

Two-step MAWCE method could prepare uniform and porous SiNWs from lightly to highly doped silicon. When the silicon substrate with Ag nanoparticles is immersed into HF/H_2O_2 solution, the reaction can be presented as follow:

$$2Ag + H_2O_2 + 2H^+ = 2Ag^+ + 2H_2O,\ E^0 = 1.77\ V \qquad (5)$$

The Ag^+ ions capture electrons from the silicon substrate and become AgNPs again (eq. 1). Silicon substrate is locally oxidized by Ag^+ ions and form SiO_2 layer at the interface between AgNPs and the silicon substrate, subsequently (eq. 2). Then the SiO_2 is dissolved by HF in the solution. In the two-step MAWCE process, H_2O_2 replace Ag^+ ions to plays as a driving force. Ag cluster plays as charge transport. Overall, H_2O_2 inject holes to the surface of the silicon substrate, the silicon surface is locally oxidized beneath AgNPs (*fig.1.10*). SiO_2 is dissolved by HF in the solution, subsequently. The overall reaction is:

$$Si + (n/2)\ H_2O_2 + 6HF = nH_2O + H_2SiF_6 + (4-n)/2\ O_2 \uparrow \qquad (6)$$

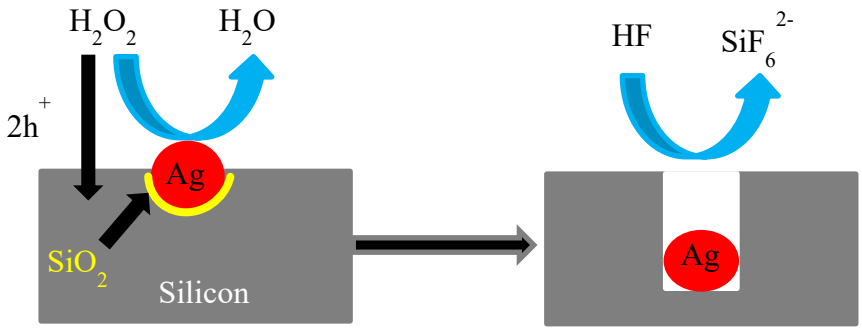

Figure 1.10: Schematical representation of the two-step MAWCE.

It is reported that diffusion penetration of Au atoms had a negative effect on the optics and electrical properties of SiNWs in the VLS process. [76] Low aspect ratio SiNWs surface is obtained by the RIE method. [77] In contrast, Ag nanoparticles can be removed easily after etching in MAWCE process. SiNWs fabricated by MAWCE method has high aspect ratio surface because of the porous nanostructure. [78] It is because Ag^+ ions diffuse out of pit and absorbed by defective sites (*e.g.* doping element) of the sidewall of SiNWs and form new nuclear. These newly formed AgNPs leading to lateral etching pathways, which results in the porous nanostructure. [79] High aspect ratio is important for photocatalyst to utilize solar

efficiently. It denotes more light is absorbed by the SiNWs surface. SiNWs also exhibit excellent absorption of light, especially in the violence range. [80] Usually, the bandgap of SiNWs is increased as wire diameter decreases. [81] Interesting, the bandgap of SiNWs prepared by MAWCE method is wider because the surface is terminated by hydrogen (ref. 94). Moreover, H-terminated surfaces of SiNWs exhibit relatively high stability in air. [82]

In summary, MAWCE is a cheap and efficient method to prepare SiNWs comparison of VLS and RIE methods. Although both one-step and two-step MAWCE can produce SiNWs, the two-step method is more efficient and widely used.

1.7 Silicon nanostructures for the hydrogen generation

SiNWs are widely used in photovoltaic. [83-87] SiNWs are also applied in other fields, for example, SiNWs are used as sensors to measure glucose and detect hydrogen peroxide. [88, 89] SiNWs sensors enable the diagnosis of patients via the exhaled breath. [90] SiNWs exhibit some novel optics and electrical properties, [91, 92] e.g. SiNWs exhibit extraordinary light-trapping ability, [93] the bandgap of SiNWs is increased to 2.5 eV while silicon bulk is 1.12 eV. [94] For these reasons, SiNWs are employed to produce hydrogen in PEC as photoelectrode and photocatalyst [95, 96]

Photocatalytic water splitting or solar hydrogen generation is one of the pillars of modern nanotechnology. Fostering any new advancement in this area, aimed not only at elevations of the process efficiencies but, importantly, also at the developments of environmentally-friendly technological routes, requires high interdisciplinary synergisms and activities across the borders of physics, chemistry and material sciences. The conversation of solar energy to split water and produce hydrogen is an ultimate aspect of the green energy and environment-friendly industry. In this context, silicon (Si) should be an ideal candidate for photocatalysis as it is the second most abundant element in the Earth's crust and possesses a narrow bandgap (Eg ~1.1 eV) to well match the solar spectrum. The silicon-based approaches are certainly favored because of material abundance and non-toxicity at a high level of materials control and understanding together with a huge industrial infrastructure to account for low production/processing costs and high production yields. Here, the unique physic-chemical properties, provided by porous semiconducting nanomaterials have attracted considerable attention over the last years. For that reason, porous silicon nanostructures (nanowires, nanoparticles) have gained enormous interest and are employed as the semiconductor

material toward hydrogen fuel production such as photoelectrochemical (PEC) water splitting [97, 98]. In comparison with the classical water electrolysis process, direct photocatalysis is a simpler and less expensive approach for hydrogen production as it eliminates the need for a conducting substrate and applied bias despite its lower efficiency of charge separation. [99] For the effective water molecule spitting the energy of the photon (excitation energy) should be higher than the bandgap (Eg) of the semiconductor, electrons in the valence band (VB) of semiconductor are excited by photons and transit to the conduction band (CB), the holes are staying at the VB. The photo-generated electrons can move to the surface of the semiconductor. The water molecule is reduced to form hydrogen while the bottom level of the CB is more negative than the redox potential of H^+/H_2 (0 V, vs. NHE), simultaneously, holes can oxide the water to form O_2 while the top level of VB is more positive than the redox potential of O_2/H_2O (1.23 V). From this side of view, the conduction band edge of Si (-0.46 V vs. NHE) is more negative than H^+/H_2 potential (0 V vs. NHE), which makes possible the effective generation of hydrogen by water molecule splitting. However, the indirect bandgap character of bulk silicon (1.12 eV) and high valence band maximum make impossible the oxidation of water molecules and the formation of molecular oxygen. Due to the low bandgap energy, the photo-generated electrons and holes are recombined much faster in comparison to wide bandgap semiconductors. However, the bandgap of nanostructured silicon can be increased by shrinking the silicon dimension. In terms of direct photocatalysis, SiNWs have extensively demonstrated their use in dye degradation and palladium-catalyzed organic reactions including Heck coupling, hydrogenolysis, hydrosilylation, and C-H bond functionalization. [100-101] Theoretical simulations have also indicated that SiNWs should be a promising photocatalyst for direct water splitting, [102] yet its feasibility needs experimental validation. Since the last few years, a growing interest in the formation and application of porous silicon nanostructures as photocatalyst can be recognized from the literature overview. Different porous silicon nanostructures have been synthesized and shown significantly enhanced solar-driven hydrogen evolution. [103-107] Dai et al. reported mesoporous crystalline Si nanoparticles react with KOH can produce hydrogen as high as 882 μmol H_2 h^{-1} g^{-1} Si. [103] Jang et al. prepared 3D multi-stacked hyperporous silicon flakes coupled with a Pt cocatalyst can produce 1031 μmol H_2 h^{-1} g^{-1} Si as photocatalyst for solar-driven hydrogen evolution. [104] Ryu et al. reported silicon nanosheets combined with platinum as a cocatalyst can produce 723 μmol H_2 h^{-1} g^{-1} Si. [105] Liu et al. reported n-type lowly doped SiNWs produced 4.48 μmol H_2 h^{-1} hydrogen in water. [106] Song et al. prepared mesoporous silicon spheres enabling

efficient and stable photocatalytic H_2 evolution (1785 μmol H_2 h^{-1} g^{-1} Si) under visible light without precious metal cocatalysts. [107] However, the long term stability due to the silicon oxidation and main light absorption in the UV spectral region was mentioned as significant disadvantages of silicon photocatalyst. From another side, as it well-known that the noble metal such as silver, gold, etc. in the coupling with semiconductor can improve the charge separation and noble metal-enhanced surface plasmon resonance (SPR) increases the light absorption in visible spectral region and allow the transfer of "hot electrons" to semiconductor, the process known as "hot electrons injection". [108-109]

Bulk silicon can react with water directly, so-called "photodegradation" at room temperature and hydrogen generation can take place, however, this reaction is very weak and self-limited. Moreover, a protective surface layer (native oxide) is rapidly formed and prevents the reaction from proceeding. For these reasons, bulk silicon is not suitable to produce hydrogen or split water molecules to molecular hydrogen and oxygen efficiently. On the other hand, nanosized silicon has been reported to enhance hydrogen production. For example, Erogbogbo et al. synthesized 10 nm diameter silicon nanoparticles (SiNPs) by laser pyrolysis to generate hydrogen 1000 times (2.58 mol H_2 per mol Si) faster than silicon bulk in water without light, heat, or electricity; [110] Ilwhan Oh et.al fabricate SiNWs by metal-catalyzed electroless to enhanced photoelectrochemical hydrogen production superior (SiNW photocathode yielded a photovoltage of 0.42 V) to that of a planar bulk Si. [111]

However, due to the narrow bandgap of silicon nanoparticles, [112] the hydrogen generated by photocatalysis is weak and the main way is oxidation of silicon nanoparticles in water. The oxidation reaction is :

$$Si + 2H_2O \rightarrow SiO_2 + 2H_2 \uparrow \qquad (7)$$

Due to the high "light absorption" ability, special nanostructure and the bandgap of SiNWs fully matches the requirement of water splitting, SiNWs are preferred bulk silicon to be applied for hydrogen generation. SiNWs are mostly used as photoanode to produce hydrogen by photoelectrochemistry (PEC) in the reported literature. Since the oxidation of SiNWs in aqueous electrolytes and oxidation product SiO_2 will result in the termination of hydrogen generation, [113] SiNWs are greatly limited as photoelectrodes in a PEC cell. The main issues of SiNWs to produce hydrogen by PEC are the design of efficient and stable SiNWs photoelectrodes. To resolve these problems, people modified SiNWs with various materials.

For example, Dai et al. decorated SiNWs with noble metal Platinum to enhance the efficiency to collect the photo-generated charges and increase stability against photooxidation. [114] Non-noble metal such as Ti and Ni metal film also have been reported as a protective layer for photocathodes in an acid electrolyte. [115-116] However, such strategies will block the light absorption of SiNWs. At present, transparent metal oxide TiO_2 is the most extensively used protective semiconducting metal oxide for Si photoelectrodes. TiO_2 is stable in various pH solution and have excellent optical transmittance. [117] However, although thick TiO_2 can avoid the permeation of electrolyte, it inhibits charge transfer from the Si to the electrolyte, resulting in poor PEC performance. [118]

Comparing PEC to produce hydrogen, direct solar-driven hydrogen generation on SiNWs is more cheap and promising. SiNWs as photocatalyst directly generate hydrogen is hardly reported. The main reason is photodegradation (corrosion or oxidation). The instability of SiNWs in water seems it is hard to be applied to produce hydrogen as photocatalyst even though its bandgap fully matches the requirement of water splitting. Moreover, people only focus on hydrogen generation and ignore the oxygen generation for SiNWs in water. Although Liu D et al. reported oxygen generation by SiNWs and tried to reveal the mechanism, [96] however, based on our oxygen measurement (Chapter **6.1**), the oxygen cannot be precisely detected by gas chromatography in the atmosphere, especially the amount of oxygen is very small. Therefore, the results of oxygen in ref. 96 remain debatable. And the author ignored the formation of SiO_x that affect the oxygen and hydrogen generation. Therefore, the mechanism of hydrogen generation in water is still not fully resolved. Also, there is no literature reports the effect of silicon type, silicon doping level on hydrogen generation. Therefore, it is necessary to investigate SiNWs as a direct photocatalyst to produce hydrogen and reveal the mechanism. In addition, the strategies to promote SiNWs to produce hydrogen and protect SiNWs are also needed to be investigated. For these reasons, I investigated SiNWs as a direct photocatalyst to produce hydrogen in water during my Ph.D. study. The main scientific tasks which I tried to explore in frame of presented Ph.D. thesis are:

1. The effect of silicon type (n- or -type) and silicon doping level (lowly or highly doped) to the hydrogen generation: which type and doping level SiNWs is the best to produce hydrogen?

2. Is a hydrogen generation on MAWCE SiNWs a light-driven process?

3. The effect of SiNWs decoration with AgNPs and their influence on hydrogen generation.
4. System excitation wavelength influence to the hydrogen generation.
5. Atomic, electronic structure and composition of initial SiNWs array.
6. How is the SiNWs surface change during the hydrogen generation?
7. Is a hydrogen generation on SiNWs a photocatalytic water splitting or enhanced surface oxidation process?

2. Experimental part

2.1 Preparation of SiNWs

Four types of commercial (CrysTec GmbH, Germany) silicon wafers were used to prepare SiNWs using the MAWCE method:

(1) n-type lowly doped Si (100) wafers (phosphor; resistivity: 1-10 Ω*cm;).
(2) n-type highly doped Si (100) wafers (phosphor; resistivity: 0.001-0.003 Ω*cm).
(3) p-type lowly doped Si (100) wafers (Boron; resistivity: 1-10 Ω*cm;).
(4) p-type highly doped Si (100) wafers (Boron; resistivity: < 0.005 Ω*cm;).

1x1 cm^2 silicon wafers were cleaned by ultrasonic rinsing in acetone for 3 min followed by an isopropanol ultrasonic rinsing for another 3 min. Further, the silicon wafer was immersed into 2% HF solution to remove the native oxide layer. Finally, the surface was cleaned in deionized water and blow-dried with inert gas. SiNWs were fabricated by metal-assisted wet-chemical etching based on our previously published work. [119] The process involves two steps: (I) AgNPs are deposited on the silicon wafer surface using aqueous solutions containing initial 0.05 M $AgNO_3$ and 5 M HF in the volume ratio 1:1 (v/v) for 15 s; (II) silicon wafers covered with Ag nanoparticles are immersed in the second etching solution containing 5 M HF and 30% H_2O_2 in the volume ratio 10:1(v/v) for 10 min at room temperature. The subsequent anisotropic etching occurs in the HF/H_2O_2 solution. Afterward, SiNWs arrays were rinsed several times in deionized water and dried at room temperature. SiNWs arrays were treated in a concentrated 65% nitric acid for 10 min to remove Ag nanoparticles from the SiNWs surfaces. After that, the samples were immersed into 2% HF solution to remove the oxide layer that was produced during HNO_3 and H_2O_2 treatments. Finally, the samples were washed by deionized water and dried by nitrogen at room temperature.

2.2 Silver decoration of SiNWs

Three methods were employed to decorate SiNWs with AgNPs: electroless silver deposition (ELD), silver mirror reaction (MR) [120] and native silver.

Electroless silver deposition (ELD) decorates SiNW matrix. The silver formation is based on the deposition of Ag nanoparticles as a result of Ag^+ reduction on the Si wafer surface. Due to the H-terminated surface of the SiNWs after passivation with diluted hydrofluoric

acid, it is necessary to add ethanol to decrease the surface tension. The reaction proceeds in an ethanol-aqueous solution of $AgNO_3$ and HF acid. SiNWs array after removal of native silver with nitric acid was washed with water and blow-dried with nitrogen followed by immediate immersion into initial concentration 0.02M $AgNO_3$: 5M HF: Ethanol (1:1:1) solution for the 60s. After the treatment time of 60s the SiNWs array was rinsed by deionized water and dried by nitrogen at room temperature.

Silver mirror reaction decorates SiNW matrix. In the first silver nanoparticles decoration stage, ammonia (NH_3H_2O) aqueous solution was slowly dropped to 0.1M or 0.05M $AgNO_3$ aqueous solution. $AgNO_3$ aqueous suspension immediately became yellow, the ammonia solution was dropped into silver nitrate solution until the solution became fully transparent without any precipitant or presence of colloidal solution. The silver-ammonia complex ($Ag[NH_3]_2OH$) solution was formed. Further, the SiNWs matrix was immersed to 96% ethanol for 3 s just to increase the hydrophilicity of the nanowires surface following by the immersion into the silver-ammonia complex solution. The reducing agent, acetaldehyde (CH_3CHO, Merck Schuchardt), was added by dropping it into the silver-ammonia complex solution at ambient conditions. SiNWs array was treated for 30 s followed by deionized water rinsing and drying by nitrogen at room temperature.

Native silver decorates SiNW matrix. After etching in the HF/H_2O_2 solution (see chapter 2.1), the SiNWs array was picked out and immediately immersed into 2% HF solution to remove the oxide layer that was produced during the etching. After that, SiNWs arrays were rinsed several times in deionized water and dried by nitrogen at room temperature.

2.3 Surface characterization and instrumentation

To investigate the produced surfaces, it is essential to investigate their microstructure, surface chemical composition, optical properties, etc. The following physical-and physic-chemical characterization methods have been involved in my research: UV-vis spectroscopy, infrared spectroscopy, scanning electron microscope (SEM), transmission electron microscopy (TEM), X-ray diffraction (XRD), atomic force microscope (AFM), BET surface area measurement, X-ray absorption near edge structure (XANES), Ultrasoft X-ray Emission Spectroscopy (USXES). The hydrogen generation on nanostructured silicon surface was carried out by gas chromatography (GC).

UV-vis spectroscopy. Reflectivity is an optical property of the material, which describes how much light is reflected and absorbed from the material in relation to an amount of light incident on the material. For photocatalysts, absorption is a very important parameter indicating the actual utilization of light to drive the photocatalysis process. The reflectance properties of photocatalyst depend on the composition and its physical and chemical states, the surface roughness as well as the geometric structure. Moreover, the bandgap of the semiconductor can be roughly estimated based on the UV-vis spectroscopy and modified Kubelka-Munk's equation. [121] The Kubelka-Munk's method is based on the following equation: [122]

$$F(R)= (1-R)^2/2R \qquad (1)$$

where R is a reflectance. A modified Kubelka-Munk function can be obtained by multiplying the F(R) function by hν, using the corresponding coefficient (n) associated with an electronic transition as follows:

$$(F(R)*h\nu)^n \qquad (2)$$

where n = 1/2 for an indirect semiconductor and n = 2 for a direct semiconductor. The energy of light can be calculated as follows:

$$E(eV) = 1240/\lambda \qquad (3)$$

where λ is the wavelength (nm) of the incident light. By plotting equation (2) versus equation (3), the bandgap (E_g) of semiconductor particles can be roughly estimated.

Figure 2.1 Digital image of JASCO V-670 UV-Vis-NIR spectrophotometer.

In my research, the reflectance spectrum of SiNWs surfaces was carried out in JASCO V-670 UV-Vis-NIR spectrophotometer equipped with a 60 mm integrating sphere (*fig.* 2.1). The detail parameters of measurement are presented as follow:

Infrared spectroscopy. Infrared spectroscopy can be used to identify and study surfaces, powders or liquid/gaseous substances. Any sample in almost any state can be studied by infrared spectroscopy. Irradiating the sample surface with a beam of infrared light (0.75 ~ 1000 μm) having a continuous wavelength, sample molecule absorbs energy and moves to higher energy level from the ground state energy level when the vibration frequency or the rotation frequency of a bond or collection of bonds is the same as the frequency of the infrared light. [123] Transmittances of light reveals how much energy is absorbed in each frequency (or wavelength). Therefore, infrared spectroscopy is an essentially analytical method for determining the molecular structure of the sample and identifying compounds based on information such as relative vibrations and molecular rotations within the molecule. The infrared spectrum is usually divided into three regions: the near-infrared region (0.75 to 2.5 μm), the mid-infrared region (2.5 to 25 μm), and the far-infrared region (25 to 1000 μm). In general, the near-infrared spectrum is generated by doubling frequency and molecules combination frequency; the mid-infrared spectrum belongs to the fundamental frequency vibration spectrum of the molecule; the far-infrared spectrum belongs to the rotational spectrum of the molecule and the vibrational spectrum of some bonds. [124]

Figure 2.2 Digital image of TENSOR 27- high performing FTIR spectrometer.

Infrared spectroscopy is a strong analytical method to investigate the change and composition of SiNWs during the hydrogen generation in water. In my experiments, infrared spectroscopy data were collected using a Tensor 27 from Bruker equipped with an MCT detector. The

measurement was performed in diamond ATR (attenuated total reflectance) mode with a resolution of 1 cm^{-1} (*fig.* 2.2). The wavenumbers are from 600 cm^{-1} to 4000 cm^{-1}.

Scanning electron microscope (SEM). Scanning electron microscopy is a topography and nanofeatures visualization method that the resolution between transmission electron microscope (TEM) and optical microscope. SEM can show the nanostructure images of a sample by scanning the surface with a focused electron beam. microscopic imaging is formed based on the properties of the sample surface. The advantages of a scanning electron microscope are: [125] (1) it has a high magnification of the sample surface and is continuously adjustable between 20 and 200,000 times; (2) it has a large depth of field, a large field of view, and a three-dimensional image, which can directly observe the uneven surface of various samples; (3) preparation of sample is simple. Also, SEM method has some disadvantages: (1) SEM can't be used to measure liquid; (2) analytic possible starting from element with number 11 (sodium); (3) limitation by resolution; (4) special field-emission technique is required for the highly developed surface characterization (nanowires or nanopowders); (5) surface charging.

SEM is widely used in the area of semiconductor material characterization. When a very fine, high-energy incident electron strikes the surface of the sample, the excited region will produce secondary electrons, Auger electrons, characteristic X-rays and continuum X-rays, backscattered electrons, transmitted electrons, and electromagnetic radiation generated in the visible, ultraviolet and infrared region. [126] These generated electrons or electromagnetic waves are specific for each chemical element and can provide not only information on surface morphology but also give quantitative and qualitative information on chemical composition (EDX, electron dispersive X-ray analysis), microstructure (EBSD, electron backscattered diffraction), cathodoluminescence, etc. Scanning electron microscopy mainly utilizes secondary electron signal imaging to observe the surface morphology of the sample. The secondary electrons can produce a magnified image of the sample surface. This image is created as the sample is scanned, ie, a magnified image is obtained by point-by-point imaging. SEM can achieve resolution better than 1 nanometer.

Figure 2.3 Digital image of Carl Zeiss ULTRA 55 scanning electron microscope.

In my experiment, structural analysis of nanostructured silicon surfaces was carried out by Carl Zeiss ULTRA 55 scanning electron microscope (*fig.* 2.3).

Transmission electron microscopy (TEM). When accelerated and concentrated electron beam strikes onto a very thin surface of the sample, the electrons collide with atoms in the sample and change direction, thereby generating solid angle scattering. The size of the scattering angle is related to the density and thickness of the sample. Therefore, images with different brightness and darkness can be formed. The resolution of the transmission electron microscope can reach 0.1 to 0.2 nm (up to single atom dimension), and the magnification is from tens of thousands to millions of times. Therefore, transmission electron microscopy can be used to observe the ultrastructure of the sample, even one column of atoms. For this reason, TEM is regarded as an essential tool for nanoscience in both physics and biology fields. However, sample preparation for TEM is complex. High-quality samples will have a thickness that is comparable to the mean free path of the electrons that travel through the samples, which may be only a few tens of nanometers. [127]

In my experiment, structural analysis of nanostructured silicon surfaces was carried out by JEM-1400 with a high tension of 80 kV and magnification between 100.000 and 500.000 times (*fig.* 2.4).

Figure 2.4 Digital image of JEM-1400 Flash Electron Microscope.

X-ray Diffraction (XRD). X-ray is an electromagnetic wave with a very short wavelength (about 20 to 0.06 angstroms). Crystal can act as a diffraction grating for X-rays. When a beam of X-rays passes through the crystal, diffraction will occur. The superposition of the diffracted waves results in the intensity of the rays to be stronger or weaker in different directions. Therefore, the crystal structure can be determined by analyzing the diffraction pattern. Moreover, the size of particles of crystals can be estimated by X-ray diffraction based on the Scherrer equation. [128] The Scherrer equation can be written as:

$$D=K\lambda/B\cos\theta \qquad (4)$$

Where:

D is the mean size of particles;

K is a dimensionless shape factor, a typical value is about 0.9;

λ is the X-ray wavelength;

B is the line broadening at half the maximum intensity (FWHM), it needs to be converted into radians (rad);

θ is the Bragg angle.

In my experiment, the crystal surface was analyzed by X-ray diffraction (XRD) pattern (X'Pert PRO / PANalytical) (*fig.* 2.5).

Figure 2.5 Digital image of X'Pert PRO / PANalytical X-ray diffraction system.

Atomic Force Microscope (AFM). Anatomic force microscope (AFM) uses a microcantilever to sense and amplify the force between the sharp probe on the cantilever and the atom of the sample under test, thereby achieving the purpose of detection with atomic resolution. Because the atomic force microscope can observe both the conductor and the non-conductor, it can make up for the shortcomings of the scanning tunneling microscope. The mode of operation of an atomic force microscope is categorized in the form of a force between the tip and the sample. There are three main modes of operation: contact mode, non-contact mode, and tapping mode. AFM is widely used in materials science and is a very important surface characterization technique. In addition to the observation of the morphology, AFM can also be used to measure the interaction between the material and the surface atoms of the material, surface elasticity, plasticity, hardness, adhesion, friction, and other properties. Moreover, different from electron microscopy, which only provides two-dimensional images, AFM provides a true three-dimensional surface map and calculates the roughness, analyze thickness, step width, block diagram or granularity of 3D topographic images.

In my experiment, the surface was analyzed by NP-AFM-4012 (*fig.* 2.6).

Figure 2.6 Digital image of the AFM system.

BET specific surface area measurement: BET is the initials of the three people (Brunauer、Emmet and Teller) who developed the mathematics required for the measurement to work. The BET specific surface area measurement can be used to test the specific surface area, porosity, pore-volume, pore size distribution, and nitrogen adsorption-desorption curve of the particles. It plays an important role in studying the surface properties of the materials.

The specific surface of the BET method is using nitrogen as the adsorbate, and helium or hydrogen is used as the carrier gas. The two gases are mixed in a certain ratio to reach the specified relative pressure and then flow through the solid matter. When the sample tube is placed in liquid nitrogen, the sample is physically adsorbed to the nitrogen in the mixed gas, and the carrier gas is not adsorbed. When the liquid nitrogen is removed, the sample tube is again at room temperature, and the adsorbed nitrogen is desorbed. Finally, a known volume of pure nitrogen is injected into the mixture to obtain a corrected peak. Based on the peak areas of the corrected peak and the desorbed peak, the amount of adsorption of the sample at the relative pressure can be calculated. By changing the mixing ratio of nitrogen and carrier gas, the adsorption amount of several nitrogens under relative pressure can be measured, so that the specific surface can be calculated according to the BET formula. [129] The BET formula is:

$$\frac{P}{V(P_0-P)} = \frac{1}{V_m \times C} + \frac{C-1}{V_m \times C} \times \frac{p}{P_0} \qquad (5)$$

where p and p_0 are the equilibrium and the saturation pressure of adsorbates at the temperature of adsorption, v is the actual adsorbed gas quantity, and v_m is the monolayer saturated adsorbed gas quantity. C is the BET constant.

In the actual test process, 3-5 samples are measured in different pressures. P/P_0 is taken as the X-axis, and $P/V(P_0-P)$ is the Y-axis. To calculate these values the BET equation is plotted as an adsorption isotherm typically at a relative pressure (P/P_0) between 0.05-0.35. In this range, the BET theory suggests it should form a straight line. The slope and intercept are calculated to obtain the V_m value to calculate the specific surface area of the sample.

Figure 2.7 Digital image of Micromeritics TriStar 3000 BET system.

In my experiment, the surface area was measured by Micromeritics TriStar 3000 BET system (*fig.* 2.7) with 5 points method. The samples were cleaned/heated at 200°C for 4h.

Gas chromatography (GC). Gas chromatography (GC) is a common type of chromatography used in analytical chemistry for separating and analyzing compounds that can be vaporized without decomposition. In the gas chromatography system, carrier gas (e.g helium or nitrogen) is a mobile phase, solid (e.g activated carbon, silica gel) in the column is a stationary phase. Carrier gas takes the sample that vaporized in the vaporization chamber into the column. Due to the differences in boiling point, polarity or adsorption performance of each component in the sample, each component tends to form distribution or adsorption equilibrium between the mobile phase and the stationary phase. As a result, the highest concentration of a component in the carrier gas flow out of the column first and the highest concentration of component absorbed on the stationary phase flow out of the column the last. [130] The separated components are taken to the detector by the carrier gas. The detector is capable of converting a sample component into an electrical signal, and the magnitude of the

electrical signal is proportional to the amount or concentration of the component. The detector usually consists of two parts: the sensor and the detection circuit. The sensor uses the various physical properties, chemical properties, and physicochemical properties of the measured substance to distinguish the carrier gas from the presence of the measured substance. For example, the thermal conductivity detector (TCD) uses the difference between the thermal conductivity of the measured substance and the thermal conductivity of the carrier gas; the flame ionization detector (FID) and the nitrogen-phosphorus detector (NPD) are all based on the measured components. Under certain conditions, it can be ionized, and the carrier gas is not ionized; the flame photometric detector (FPD) uses the measured substance to emit light of different wavelengths under certain conditions, while the carrier gas N_2 does not emit light. Therefore, the sensor is a device that converts the substance to be measured into a corresponding signal. It is the heart of the detector. The signals sent from the sensor are various, including resistance, current, voltage, ion current, frequency, lightwave, etc. The function of the detection circuit is to determine these parameterizations and turn them into measurable electrical signals. For example, the change of the heat wire resistance in the TCD is converted into an electrical signal by using the Wheatstone bridge; the ion current generated by various gas-phase ionization is collected by the electric field and amplified by the microcurrent amplifier to show its change;

The gas chromatograph consists of five systems: pneumatic system, injection system, separation system, temperature control system, and detection system, [131] in which the separation system and detection system are the most important. There are two methods to inject samples into inlets: automatic injection and manual injection. Automatic injection provides better reproducibility and time-optimization. There are many types of detectors currently available, among which the commonly used detectors are: hydrogen flame ionization detector (FID), thermal conductivity detector (TCD), nitrogen phosphorus detector (NPD) flame photometric detector (FPD), electron capture detector (ECD), etc.

In my experiment, the evolved hydrogen was quantified by gas chromatography (GC) coupled with a thermal conductivity detector (Agilent 7820A, 6 ft, 1/8", packed 80/100 HayeSep Q column, helium 5.0 carrier gas) (*fig.* 2.8).

Figure 2.8 Digital image of Agilent 7820A gas chromatography.

X-ray absorption near edge structure (XANES). In the X-ray absorption spectrum, a spectrum in a low-energy region within 60 eV and above the threshold exhibits a strong absorption characteristic, which is called a near-edge absorption structure (XANES). It is caused by the excitation of photoelectrons undergoing multiple scattering of surrounding atoms. When the X-ray energy is equal to the ionization energy of an inner electron of the irradiated sample, resonance absorption occurs, the electron is ionized into photoelectrons, and the X-ray absorption coefficient is abrupt. This jump is called an edge. A typical XANES spectrum contains pre-edge, edge, post-edge. The absorption edges of electrons of different principal quantum numbers in atoms are quite far apart, and are named K, L, ... absorption edges, etc. according to the main quantum number. Each element has its characteristic absorption edge, therefore, XANES can be used for qualitative analysis of elements. In addition, the position of the absorption edge is related to the valence state of the element, and the absorption edge moves to the high energy side when the oxidation price increases, therefore, XANES can identify the element or the same element with different valence.

XANES is a useful tool for studying condensed matter. The application of XANES in the field of catalysis has the following aspects:

1. Identification of the catalyst phase.
2. Study on catalyst geometry and electronic structure.
3. Study on catalyst adsorption behavior.
4. Research on the structure of metal complexes.

In my experiment, XANES is employed to investigate the silicon surface electronic structure and distribution of element Si valence. XANES was measured by staff in HZB BESSY-II RGBL in Berlin.

Ultrasoft X-ray Emission Spectroscopy (USXES). USXES is a type of X-ray spectroscopy where the sample is bombarded with ultra-low energy (<1 keV) X-rays and the energies and intensities of the X-rays emitted due to valence-to-core transitions. USXES shows information about inner electron excitations in light atoms. USXES also can identify the element and the same element with different valence. Moreover, USXES can measure the composition of deep surface (reach to 120 nm). Therefore, USXES is an important technique to investigate the surface of the catalyst.

In my experiment, USXES is employed to investigate the silicon surface electronic structure and composition of the silicon surface. USXES is measured by staff at Voronezh State University.

2.4 Photocatalytic hydrogen evolution experiments

In photocatalytic hydrogen evolution experiments, two measurement methods were employed：manual injection and automatic injection. For manual injection, hydrogen evolution happened in a completely closed system. The total amount of hydrogen can be measured precisely. However, the individual difference of SiNWs (for example, etching time and etching temperature) can't be controlled identically among SiNWs wafers and the errors from manual injection were inevitable. The automatic injection could avoid these problems because the volume of injection was controlled by gas chromatography (GC). However, it is not a completely closed system with automatic injection due to the connection between the GC and the reactor. Considering the advantages and disadvantages of manual injection and automatic injection, the manual injection was employed to measure the total amount of hydrogen and the automatic injection was employed to investigate hydrogen generation kinetics. The temperature was controlled by mini fans.

To determine the amount or concentration of the hydrogen, a calibration curve should be done first. Pure hydrogen is injected with precise different volumes, the peak areas and volumes of hydrogen will be recorded. Each volume corresponds to a peak area. A calibration curve of hydrogen can be obtained by plotting volume or concentration to the peak area. The area of hydrogen to be tested will be recorded by the GC. Then the amount or concentration of the tested hydrogen can be estimated by the calibration curve.

An ethanol-water (v/v, 1:4) mixture was used for the hydrogen evolution experiments, (i) in order to reduce the surface tension of the solvent in particular as the SiNWs are very hydrophobic after etching and hydrogen termination processes. The presence of ethanol reduces the surface tension and increases the water molecule penetration into the porous silicon nanowires matrix. (ii) Ethanol as a "hole-scavager" can promote the separation of photogenerated electrons and holes and enhance the hydrogen generation rate in the hydrogen evolution was pointed in ref [26].

Manual injection part: 1x1cm^2 SiNW chips covered with AgNPs were cut into two pieces and fixed into a 5 mL vial. The water/ethanol (4:1; v/v) solution was degassed with a freeze-pump-thaw triple cycle under argon and the vial was degassed using standard Schlenk technique for three times under argon atmosphere. 3 mL water-ethanol solution was injected into the vial under argon atmosphere. The vial was irradiated with a neutral white LED lamp (33 mW/cm^2, ChiliTec GmbH, 4200 K) for maximum 180 minutes at ambient room conditions. The detached hydrogen amount was sampled manually by syringe (100 µL) from the 2 ml headspace of each vial after 5, 15, 30, 60, 120, 180 min. The evolved hydrogen was quantified by gas chromatography (GC) coupled with a thermal conductivity detector (Agilent 7820A, 6 ft, 1/8", packed 80/100 HayeSep Q column, helium 5.0 carrier gas). The hydrogen calibration curve was obtained by linear regression after the injection of known volumes of pure hydrogen. Each measured point was repeated at least two times. The total amount of generated hydrogen is 20 times (2 mL/ 100 µL) as the results of GC measurement.

Automatic injection part: Water/ethanol (4:1; v/v) solution was degassed with a freeze-pump-thaw triple cycle under argon and the vial was degassed using standard Schlenk technique for three times under argon atmosphere. Three pieces of n-type highly SiNWs were fixed into the top part of the 75 mL reactor. Then 50 mL water/ethanol (4:1; v/v) solution was injected into the reactor (the solution does not contact SiNWs). The reactor was degassed with a freeze-pump-thaw triple cycle under argon using standard Schlenk technique three times under argon. After that, the reactor was connected with gas chromatography. The n-type highly doped SiNWs with native AgNPs were moved carefully into the solution and started the timer immediately. Mini-electric fans were employed to cool down the temperature of the reactor. Then the reactor was cover with aluminum foil to keep it in the darkness. The neutral white LED lamp was switched on and off every 10 minutes. The hydrogen measurement was automatically controlled by the periodical injection of 250 µL of

analyzed gases mixture from the reactor volume. The total amount of generated hydrogen is 100 times (25 mL/ 250 μL) as the results of GC measurement.

2.5 Photocatalytic oxygen evolution experiments

Gas chromatography method. 1x1cm^2 SiNW chips were cut into two pieces and fixed into a 5 mL vial. The pure water solution was degassed with a freeze-pump-thaw triple cycle under nitrogen and the vial was degassed using glove box under the nitrogen atmosphere. 3 mL pure water solution was injected into the vial in the glove box. The vial was irradiated with a neutral white LED lamp (33 mW/cm^2, ChiliTec GmbH, 4200 K), green LED (505 nm, THORLABS, M505L3, 33.75 mW/cm^2) and blue light LED (365 nm, THORLABS, M365LP1, 42.5 mW/cm^2) for 180 minutes, maintaining room temperature with four fans. The evolved hydrogen was sampled manually by syringe (100 μL) from the 2 ml headspace of each vial after 180 min. The evolved oxygen was quantified by gas chromatography (GC) coupled with a thermal conductivity detector (Agilent 7820A, 6 ft, 1/8", packed 80/100 HayeSep Q column, helium 5.0 carrier gas).

Oxygen sensor method. 1x1cm^2 SiNW chips were cut into two pieces and fixed into a 5 mL vial. The pure water solution was degassed with a freeze-pump-thaw triple cycle under nitrogen and the vial was degassed using glove box under the nitrogen atmosphere. 3 mL pure water solution was injected into the vial in the glove box. The vial was irradiated with a neutral white LED lamp (33 mW/cm^2, ChiliTec GmbH, 4200 K), the green LED (505 nm, THORLABS, M505L3, 33.75 mW/cm^2) and blue light LED (365 nm, THORLABS, M365LP1, 42.5 mW/cm^2) for 180 minutes. The oxygen sensor (PyroScience GmbH, OXF50) was immersed in the water and the signal is recorded by the computer.

3. Results and discussion

In this part, the electron microscopy and optical properties of different types (n- and p-type) and different doping levels (lowly doped and highly doped) SiNWs will be discussed. The hydrogen generation of different types (n- and p-type) and different doping levels (lowly doped and highly doped) SiNWs also will be investigated. Based on the hydrogen generation result, SiNWs that have the best performance of hydrogen generation will be chosen to be decorated with AgNPs. AgNPs decorate SiNWs at the top, in the middle and at the bottom (native AgNPs) by three methods (ELD, MR and native AgNPs), respectively. The influence of AgNPs on the hydrogen generation of SiNWs will be investigated, subsequently. The effect of hole-scavager, surface area and excitation wavelength on hydrogen generation of SiNWs also will be investigated. Finally, and most importantly, the surface investigation of SiNWs before and after hydrogen will be performed by USXES, XANES, UV-vis spectroscopy, Infrared spectroscopy, AFM, BET, etc.

3.1 Electron microscopy and optical properties of SiNWs

Figure.3.1 shows SEM images of silicon nanowires prepared at different Ag^+concentrations, i.e.0.02 M, 0.05M $AgNO_3$ and 0.1M using n-type lowly doped silicon wafers. The concentration of silver ions in step (I) of MAWCE strongly influences the density and/or distance between neighboring SiNWs that finally influence the location of AgNPs on the SiNWs during the decoration. It is clear to observe that the size of Ag nanoparticles is bigger when the concentration of $AgNO_3$ is higher (*fig.3.1* a, c, e). A higher density of nanowires was observed due to the formation of smaller AgNPs when the samples were prepared using lower Ag^+ concentration (*fig.3.1* b). In contrast, higher Ag^+ concentrations, e.g. 0.05 M, yield samples with a higher distance between neighboring nanowires (*fig.3.1* d). However, when the concentration of $AgNO_3$ solution was increased to 0.1M, a dendritic silver layer was formed on top of the silicon surface which prohibits further HF diffusion toward the interface between AgNPs and Si surface to dissolve SiO_2 after holes injection from the AgNPs, which results in a slow etching rate and random lengths (*Fig.3.1* f). To decorated SiNWs with AgNPs, lower density denotes that AgNPs are easier to reach deeper part of SiNWs. Therefore, 0.05M $AgNO_3$ is a favorable concentration.

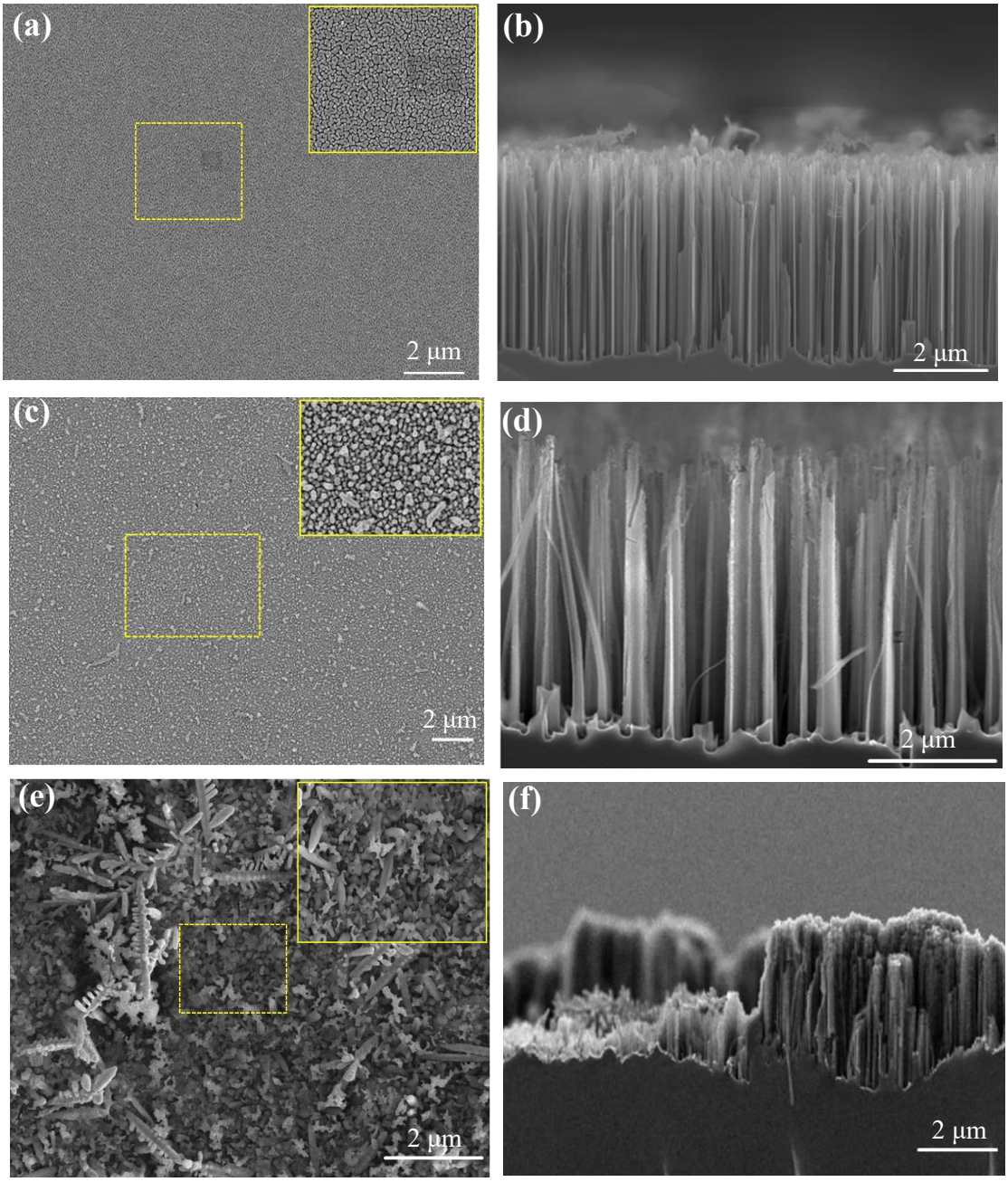

Figure 3.1 Scanning electon microscopy (SEM) images of silicon surfaces: Planar view of silver nanoparticles deposit for 15s on the surface of silicon matrix using (a) 0.02M $AgNO_3$; (c) 0.05M $AgNO_3$ and (e) 0.1M $AgNO_3$ in I step of MAWCE process; Cross-sectional view of n-type lowly doped SiNWs after II step MAWCE process using three different silver concentrations and 10 min etching time: (b) 0.02M $AgNO_3$, (d) 0.05M $AgNO_3$ and (f) 0.1M $AgNO_3$.

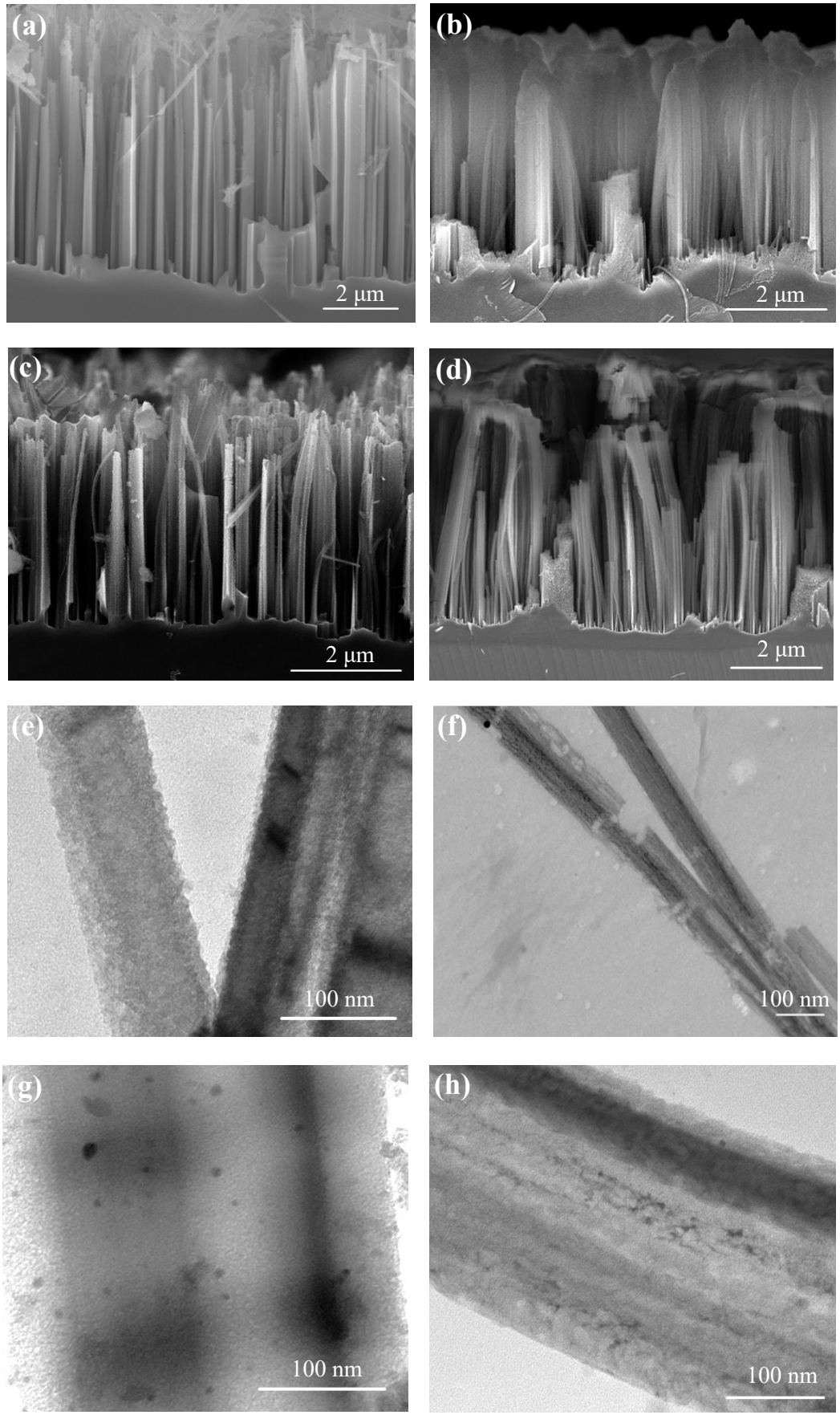
(a)
2 µm
(b)
2 µm
(c)
2 µm
(d)
2 µm
(e)
100 nm
(f)
100 nm
(g)
100 nm
(h)
100 nm

Figure 3.2 SEM cross-sectional images of (a) n-type lowly doped SiNWs; (b) n-type highly doped SiNWs; (c) p-type lowly doped SiNWs; (d) p-type highly doped SiNWs prepared in identical conditions (0.05M $AgNO_3$, deposition time: 15 sec, etching time: 10 min); TEM micrographs of (e) n-type lowly doped SiNWs; (f) n-type highly doped SiNWs; (g) p-type lowly doped SiNWs; (h) p-type highy doped SiNWs prepared in identical conditions (0.05M $AgNO_3$, deposition time: 15 sec, etching time: 10 min).

The doping level and doping type of silicon are important factors to affect the etching rate and morphology of SiNWs. It is reported that lowly (10 Ω*cm) and highly doped (0.01 Ω*cm) silicon showed different etching rates in identical conditions. [132] It is not the only doping level but also the dopant chemical nature that affects the silicon etching rate. Canevali et al. reported that etching rates increase with dopant concentration increasing and phosphorus-doped silicon has higher etching rate in comparison to arsenic (As) doped wafers. [133] Lai et al. reported that n-type silicon consistently etches faster than the p-type silicon regardless of doping level due to the Schottky barrier interface electric field between Au and Si confines holes to the surface.[134]

The scanning electron microscopy studies of SiNWs produced by MAWCE are presented in Figure 3.2. The length of n-type SiNWs is about 4 μm, in comparison, p-type SiNWs is about 3 μm. Moreover, the density of n-type SiNWs is higher than p-type SiNWs.

Besides influencing the etching rate, the doping level of the silicon also affects the morphology of SiNWs. Figure 3.2 (a)-(d) show the totally different morphologies of SiNWs with different doping level fabricated in identical conditions. Vertically aligned and ordered crystalline SiNW arrays are obtained from lowly doped silicon (1-10 Ω*cm) regardless of the special silicon type (*fig. 3.2 a* and *c*). In contrast, highly doped SiNWs surface looks rougher (*fig 3.2 b* and *d*). From the TEM micrographs, it is clear to see that the surface of n-lowly doped SiNWs is rough (*fig.3.2 e*) and n-highly doped SiNWs is rougher and more porous (*fig.3.2 f*). It can be explained as follow: [135] During the etching process, AgNPs are oxidized to Ag^+ ions by H_2O_2 and the Ag^+ ions diffuse out of the pit and are absorbed by defect sites (doping element) of the sidewall of SiNWs and form new nucleus for particle growth. These newly formed AgNPs leading to lateral etching pathways, which results in the porous nanostructure. Since highly doped silicon has many more dopants than lowly doped silicon substrate, therefore, the surface is porous. Figure 3.2 (g) and (h) show that the surface of p-type lowly doped SiNWs is smooth but p-type highly doped SiNWs is rougher and more

porous. Comparing Figure 3.1 (e) and (h), the surface of n-type lowly doped SiNWs is rougher than p-type highly doped SiNWs. It denotes that the type of silicon also can strongly influence the surface of SiNWs. The less rough surface of p-type SiNWs indicates that the lateral etching in such type of materials is not preferable. The most probable explanation could be the reason that excess electrons in n-type silicon can easily trap Ag^{+} ions and form new nucleus that is not a case for p-type silicon due to the excess holes.

The observed surface reflectivity measurement properties have been investigated by UV-vis spectroscopy in the spectral range between 200 and 1500 nm. Reflectivity measurements of the SiNWs are given in Figure 3.3a. It is clear to see that in the spectral region between 200 nm and 1050 nm SiNWs have much stronger absorption and lower reflectance than in comparison to nonstructured silicon wafer (*green line, in Fig. 3.3*). Furthermore, p-type and n-type highly doped SiNWs absorb more light in the spectral range of 200-1500 nm than p-type and n-type lowly doped SiNWs, respectively as shown in Fig. 3.3b. Also, n-type SiNWs exhibit higher light absorption than p-type SiNWs regardless of the doping level. N-type highly doped SiNWs have the best ability of light absorption in the range of 200-1500 nm (*red line in Fig. 3.3*). The reflectance of n-type highly doped SiNWs (*red line*) is less than 2% at wavelengths from 200 to 1500 nm as shown in Figure 3.3a. These results indicate that n-type highly doped SiNWs strongly suppress optical reflection. N-type highly doped SiNWs have higher optical absorption than n-type lowly doped SiNWs could be explained as follows: firstly, the n-type highly doped SiNWs array has much higher surface area as was found from

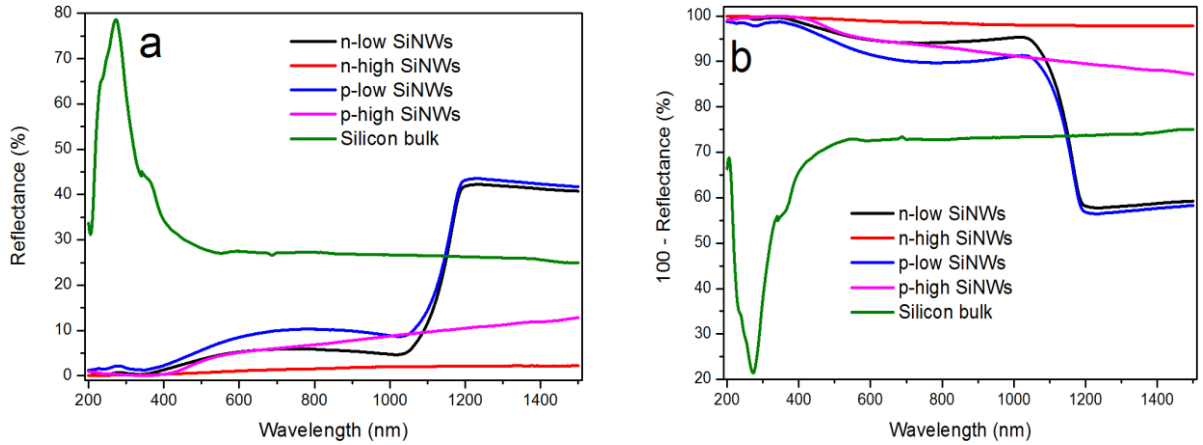

Figure 3.3 a: Reflectance spectra of n- and p-type lowly and highly doped SiNWs and single-crystalline n-type highly silicon wafer (bulk). b: 100-Reflectance spectra of n- and p-type lowly and highly doped SiNWs and single-crystalline n-type highly silicon wafer (bulk).

SEM and TEM studies in Figure 3.2; Secondly, surface sub-wavelength structures (SWSs) of the SiNW arrays could suppress the reflection over a wide spectral bandwidth; [136] and the last but not the least, the collective light scattering interactions among highly doped SiNWs, which trap the light and make it travels more turns over distances than the lowly doped SiNWs. [137] The length of SiNWs is another important factor to influence the light absorption. The light absorption increases with the length of the SiNWs. [138] This factor we also indicate in our system where the longer is n-type SiNWs (*fig 3.1* a-d), they have higher light absorption than p-type SiNWs. It is worth to note that a characteristic hillside of lowly doped SiNWs in the NIR region at about 1050-1200 nm and the light absorption is stable (about 40%) in the longer wavelength from 1200 nm. The reason could be related to the bandgap of bulk silicon around 1100 nm. The bandgap values of n-type lowly, n-type highly, p-type lowly and p-type highly doped SiNWs were roughly estimated as about 3.0 eV based on the reflectivity and Kubelka-Munk function (Supplement II).

3.2 SiNWs decorated with AgNPs by ELD, MR and native AgNPs

Since the last decade, porous silicon-based nanostructures have been widely reported in photoelectrochemistry (PEC) as a photoanode for hydrogen generation. However, the oxidation of silicon in aqueous electrolytes and formation of SiO_2 layer leads to the termination of hydrogen production. [139] The main issues for the hydrogen generation increase in the PEC system are efficient and stable silicon nanostructures based photoelectrodes. To resolve these limitations, the surface can be modified with various materials, for example, noble metal nanoparticles. The decoration of SiNWs by silver nanoparticles is one possible strategy to improve the efficiency of hydrogen generation. For example, Dadwal et al. decorated SiNWs with silver dendrites to enhance the photoinduced charge carrier separation and increase stability against photooxidation in the photoelectrochemical splitting of natural water. [140] AgNPs@SiNWs nanostructure was also applied as a photocatalyst to reduce 4-nitrophenol and decompose fluorescein sodium. [141, 142] Noble metals such as silver and gold are known as materials for the charge separation in case coupled to semiconductors and noble metal increases the light absorption in the visible spectral region because of surface plasmon resonance (SPR). [143-145] Furthermore, such metal-semiconductor hybrids allow the transfer of “hot electrons” to the semiconductor, a process known as “hot electron injection”. [146] Dai et al. modified SiNWs with platinum nanoparticles by atomic layer deposition (ALD) in a photoelectrochemical cell (PEC) to enhance the generation rate of hydrogen. [147] Zhu et al. modified SiNWs with ruthenium as

electrocatalysts exhibited higher hydrogen evolution performance in comparison to the pure Ru particles. [148] Hence, the decoration of SiNWs with AgNPs is a possible way to enhance the light absorption in visible spectral range and hydrogen generation rate.

In this thesis, three methods were employed to decorate SiNWs with AgNPs: electroless silver deposition (ELD), silver mirror reaction (MR) and native silver.

3.2.1 Electroless silver deposition (ELD) decoration of SiNWs

Electroless silver deposition (ELD) has been widely reported to decorate SiNWs with AgNPs. [149-151] Electroless deposition of noble metals by galvanic displacement is a comparably simple and cheap method. The method requires the treatment of a SiNWs matrix in an $AgNO_3$/HF water-based solution at ambient atmospheric conditions. Silver ions are reduced to metallic AgNPs by capturing electrons from SiNWs and deposit on the surface of SiNWs in the $AgNO_3$/HF solution.

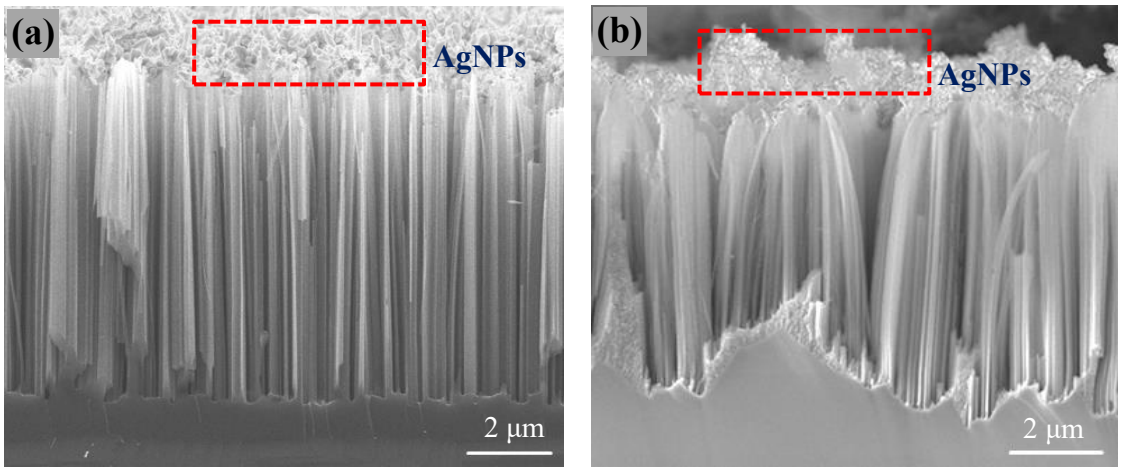

Figure 3.4 SEM cross-sectional views of n-type (a) lowly and (b) highly doped SiNWs decorated with AgNPs by ELD. (The experimental details are presented in Chapter **2.2**).

Figure 3.4 shows the morphologies of n-type lowly and highly SiNWs decorated with AgNPs by ELD. It is clear to see that AgNPs only deposit on the top of SiNWs (the red frame). It indicates that Ag^+ ions cannot penetrate deeper into the channels between the neighboring SiNWs. The reason could be Si-H terminated SiNWs surface with superhydrophobic nature after surface passivation with 2% hydrofluoric acid.

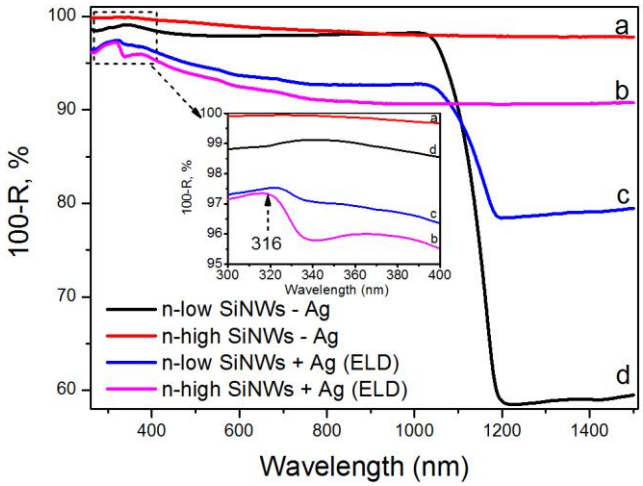

Figure 3.5 Absorption (100-R) spectra of n-type highly doped SiNWs (a) without AgNPs and (b) decorated with by ELD; n-type lowly doped SiNWs (c) decorated with AgNPs by ELD and (d) without AgNPs.

Absorption measurements of n-type lowly and highly doped SiNWs decorated with AgNPs are given in Figure 3.5. The absorption of n-type highly doped SiNWs decorated with AgNPs (ELD) is lower than n-type highly doped SiNWs without AgNPs in the whole range. The absorption of n-type lowly doped SiNWs with (ELD) is also lower than SiNWs without AgNPs in the range of about 200-1100 nm. It is because of the reflection of AgNPs on the top of SiNWs. It is noted to mention that a remarkable absorption peak at 316 nm attributes to silver clusters.[152]

3.2.2 Silver mirror reaction (MR) decoration of SiNWs

The well-known silver mirror (MR) approach enables the production of the silver-semiconductor hybrid system without employing any surfactants and additives, thus resulting in the formation of nanoparticles with “clean” and hence highly reactive metal surfaces. To the best of our knowledge, the silver mirror reaction has not been reported as a method to modify the surfaces of SiNWs by silver nanostructures. The silver mirror reaction can be divided into two steps: first, ammonia is dropped into $AgNO_3$ solution to form $Ag[NH_3]_2OH$, the reaction can be presented as follow:

$$AgNO_3 + 3NH_3H_2O = Ag[NH_3]_2OH + NH_4NO_3 + 2H_2O \quad (1)$$

In this step, the concentration of $Ag[NH_3]_2OH$ is determined by the concentration of $AgNO_3$. In the second stage, $Ag[NH_3]_2OH$ can be reduced by aldehydes (e.g. Acetaldehyde) and produce metallic silver, the reaction can be presented as follow:

$$CH_3CHO + 2Ag[NH_3]_2OH = CH_3COONH_4 + 2Ag\downarrow + 3NH_3 + H_2O \qquad (2)$$

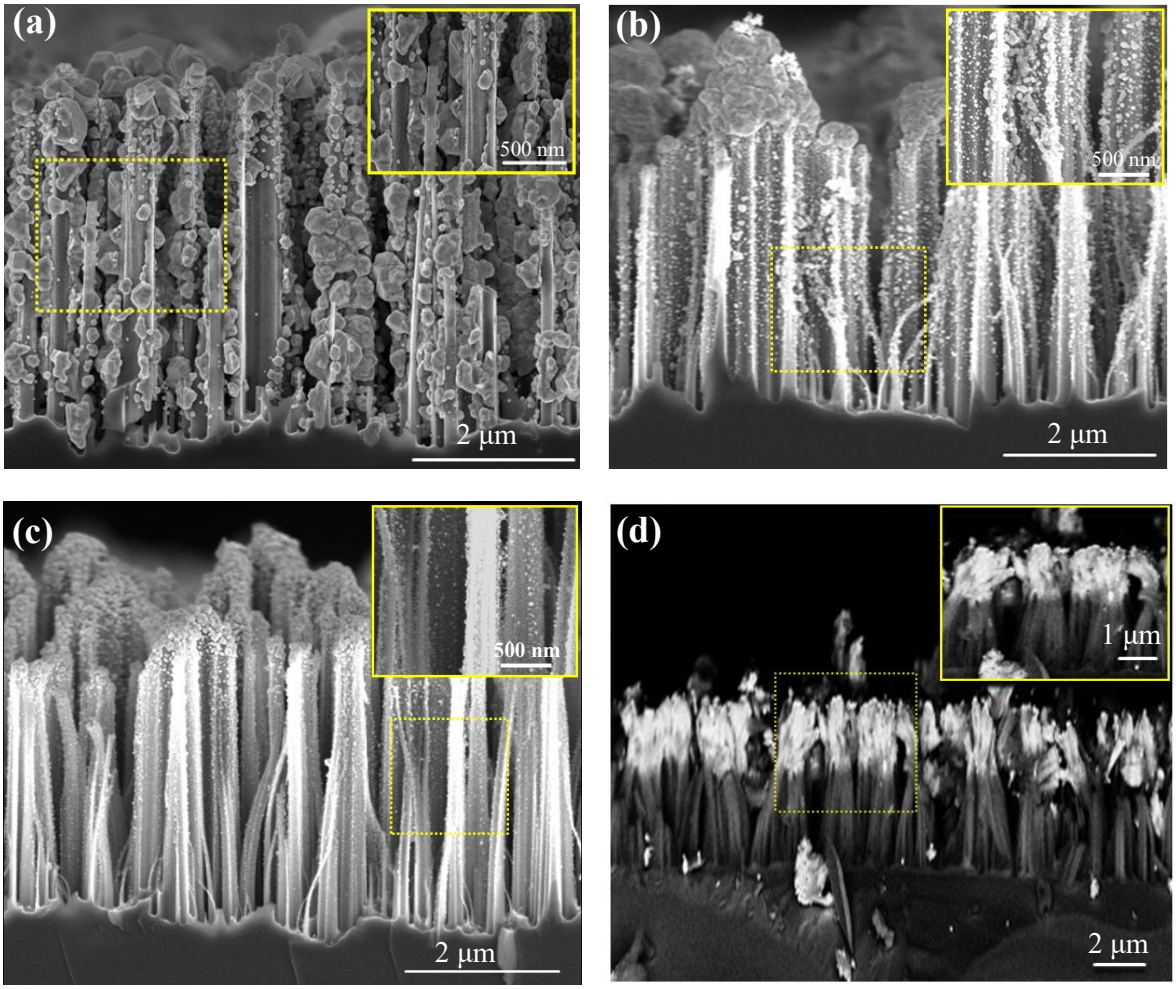

Figure 3.6 SEM cross-sectional images of n-type lowly doped SiNWs decorated with AgNPs by mirror reaction using: (a) 0.1 M $AgNO_3$, reaction time 2 min; (b) 0.1 M $AgNO_3$, reaction time 30 s; (c) 0.05 M $AgNO_3$, reaction time 30 s; (d) n-type highly doped SiNWs decorated with AgNPs by mirror reaction using 0.05 M $AgNO_3$, reaction time 30 s. All experiments were performed at room temperature (295K). (inset: zoom of)

Figure 3.6 shows SEM images of SiNWs decorated with AgNPs by the approach laid out above by using different conditions for silver nanoparticle formation. From Figure 3.6 a-c, it is apparent that AgNPs are deposited on the entire surface of the SiNWs matrix, i.e. a continuous AgNPs shell is formed around the SiNWs. The different morphologies in Figure

3.6 indicate that shape, uniformity, and geometry of the AgNPs strongly depend on the deposition kinetics and hence the concentrations of $AgNO_3$ and growth time.

To investigate the effect of growth time, coating reactions were performed for different reaction times while keeping the other experimental conditions unchanged (Figure 3.6 a and b). AgNPs are bulky-like and fully filling the spaces between SiNWs when the reaction time was 2 min as shown in Figure 3.6 (a). The size of AgNPs on the sidewall of SiNWs is about 90 nm (Figure 3.6 an inset) and dramatically decreased (down to 45 nm in Figure 3.6 b inset) when the reaction time was shortened to 30 s. However, the AgNPs stack at the top of SiNWs in Figure 3.6 b and form about 2 μm AgNPs agglomerates. Our observation thus indicates that the size of AgNPs on the surface of SiNWs can be controlled by reaction time.

The concentration of $AgNO_3$ also affects the morphology of AgNPs@SiNWs. 0.1M and 0.05M silver nitrate concentrations were used to investigate the influence of $AgNO_3$ concentration on the formation of the silver nanoparticles as shown in Figure 3.6 b and c: AgNPs are apparently localized on a top and sidewalls of SiNWs and become smaller and without additional silver nanoparticles agglomerates formation on a top of SiNWs at 0.05 M $AgNO_3$ concentration as presented in Figure 3.6 c. AgNPs@SiNWs coverage in Figure 3.6 c is more homogeneous in comparison to the silver nanoparticles formed at higher silver nitrate concentration. In general, the size of AgNPs and the morphology of AgNPs@SiNWs nanostructure can be controlled by tuning the concentrations of $AgNO_3$ and the reaction time. The mean sizes of AgNPs are calculated from XRD measurements using Scherrer's formula presented in Figure 3.7 and were found to be 33 nm, 21 nm and 19 nm for the silver nanostructures in Figure 3.6 a-c, respectively. The average size deviation of nanoparticles, by applying manual data processing (50 samples) and using Scherrer's formula, is 5%.

In general, a uniform and homogenous AgNPs@SiNWs coverage is achieved at 0.05M $AgNO_3$ and 30 s reaction time. The same conditions are employed to decorate n-type highly doped SiNWs (Figure 3.6 d). Comparing the morphologies of Figure 3.4 and Figure 3.6, the AgNPs can reach the deeper part of SiNWs by MR method. It could be the gravity settlement of AgNPs formed by MR.

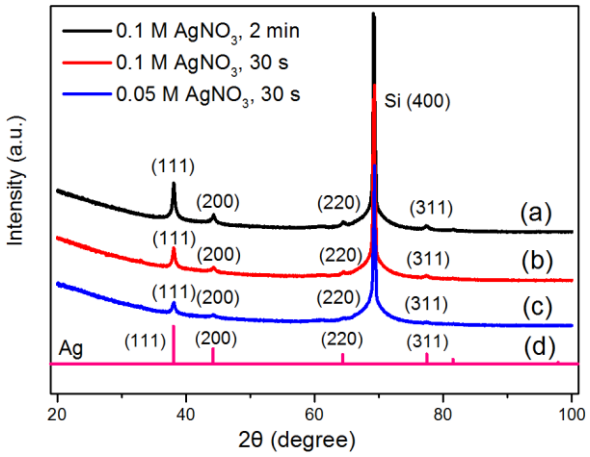

Figure 3.7 XRD diffraction patterns of AgNPs@SiNWs (n-type lowly doped) prepared at: (a) 0.1 M $AgNO_3$, reaction time 2 min; (b) 0.1M $AgNO_3$, reaction time 30 s; (c) 0.05M $AgNO_3$, reaction time 30 s; (d) reference pattern of Ag [JCPDS Card No. 00-004-0783].

The crystallinity studies of the AgNPs@SiNWs nanostructures were determined by XRD measurements as presented in Figure 3.7. The reflexes at 2θ values of 38.1°, 44.3°, 64.4°, 77.5° belong to Ag (111), (200,) (220), (311) and in a good agreement with the reference pattern of polycrystalline Ag [JCPDS Card No. 00-004-0783]. A strong reflex at 2θ 69.1° is attributed to the characteristic reflex of Si(400).[153] These results are strongly indicating the polycrystalline character of the silver precipitate. The second aspect which is clearly visible in XRD patterns is that the crystallinity of deposited silver into the SiNWs matrix increases with the increasing of initial silver nitrate concentration and growth time.

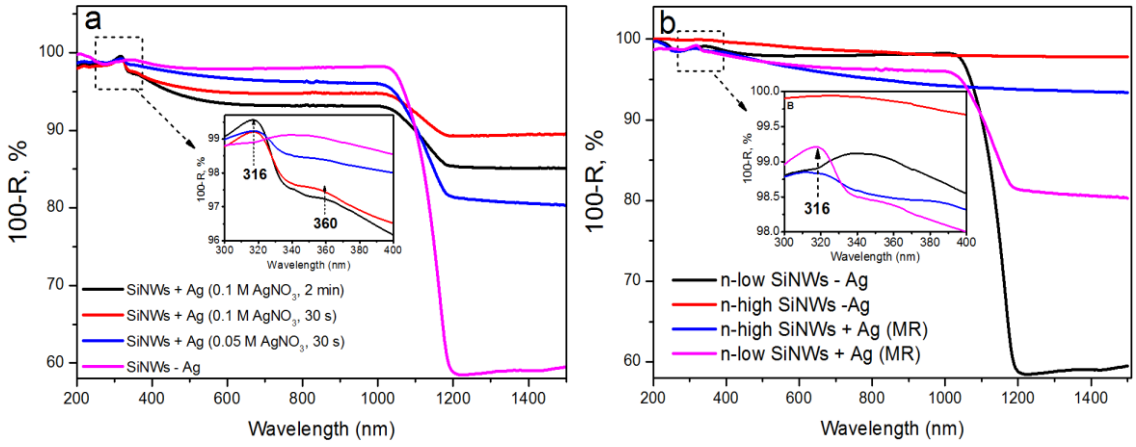

Figure 3.8 a: Absorption (100-R) spectra of n-type lowly doped SiNWs decorated with AgNPs prepared at different conditions. Inset: zoomed absorption spectra in the range of 300-400 nm. b: Absorption (100-R) spectra of n-type lowly and highly doped SiNWs without and with AgNPs by MR, the conditions of decoration are 0.05M $AgNO_3$, reaction time 30 s.

Absorption spectra of the AgNPs@SiNWs (Figure 3.6 a-c) are given in Figure 3.8 (a). The absorption of observed silver nanoparticles decorated nanostructures is about 40% higher in the near IR region (1000-1500 nm) in comparison to the non-decorated SiNWs matrix and similar in the whole visible region. In the silver nanoparticles decorated SiNWs two prominent absorption peaks at 316 nm and 360 nm (cf. Figure 3.8 inset) are present. The peak at 316 nm can be assigned to silver clusters, while the peak at 360 nm is due to the absorption of single silver atoms. [154] The typical absorption peak of AgNPs associated with the surface plasmon resonance at about 400 nm is not observed. The formation of AgNPs agglomerates on the top of SiNWs and the formation of the 2D silver thin film might explain this effect. [155] Figure 3.8 (b) is the absorption of the n-type lowly and highly doped SiNWs without and with AgNPs by MR. The absorption is similar to Figure 3.5.

In general, homogenous decoration of SiNWs by silver nanoparticles can be achieved by a cheap and facile approach based on the silver mirror reaction. The size of AgNPs and morphology of AgNPs@SiNWs is controlled by the variation of $AgNO_3$ concentration and reaction time. A uniform and homogenous AgNPs@SiNWs coverage is achieved at 0.05M $AgNO_3$ and 30 s reaction time. The AgNPs@SiNWs synthesized in this study exhibit two absorption bands at about 316 and 360 nm, which are related to absorption by silver clusters and/or single Ag atoms, respectively. Moreover, AgNPs@SiNWs show stronger light absorption in the near IR spectral region (1000-1500) nm in comparison to the non-decorated SiNWs matrix.

3.2.3 Native silver decoration of SiNWs

The general preparation aspects of SiNWs matrices used in the presented work have been presented in detail in chapter **1.5**. AgNPs have been used to etch silicon as catalysts. AgNPs stay at the bottom of SiNWs after etching (*fig. 3.9 a*). Usually, the AgNPs are removed by 65% nitric acid to prepare "clean" SiNWs (*fig. 3.9 b*) matrices/surfaces. In this part of experiment, natively produced AgNPs are saved as "native silver" to decorate SiNWs. SEM images of SiNWs with and without native AgNPs before hydrogen evolution are presented in Figure 3.9 (a) and (b), respectively. It is clear to see the native AgNPs stay at the bottom of SiNWs and can be removed by applying 65% HNO_3 treatment. XRD diffraction in Figure 3.10 (a) also demonstrates the presence of AgNPs. In Figure 3.10 (a), the reflexes at 2θ 38.1°, 44.3°, 64.4°, 77.5° belong to crystalline Ag (111), (200,) (220), (311), respectively, in a good agreement with the reference pattern of polycrystalline silver. A strong reflex at 2θ 69.1° is attributed to

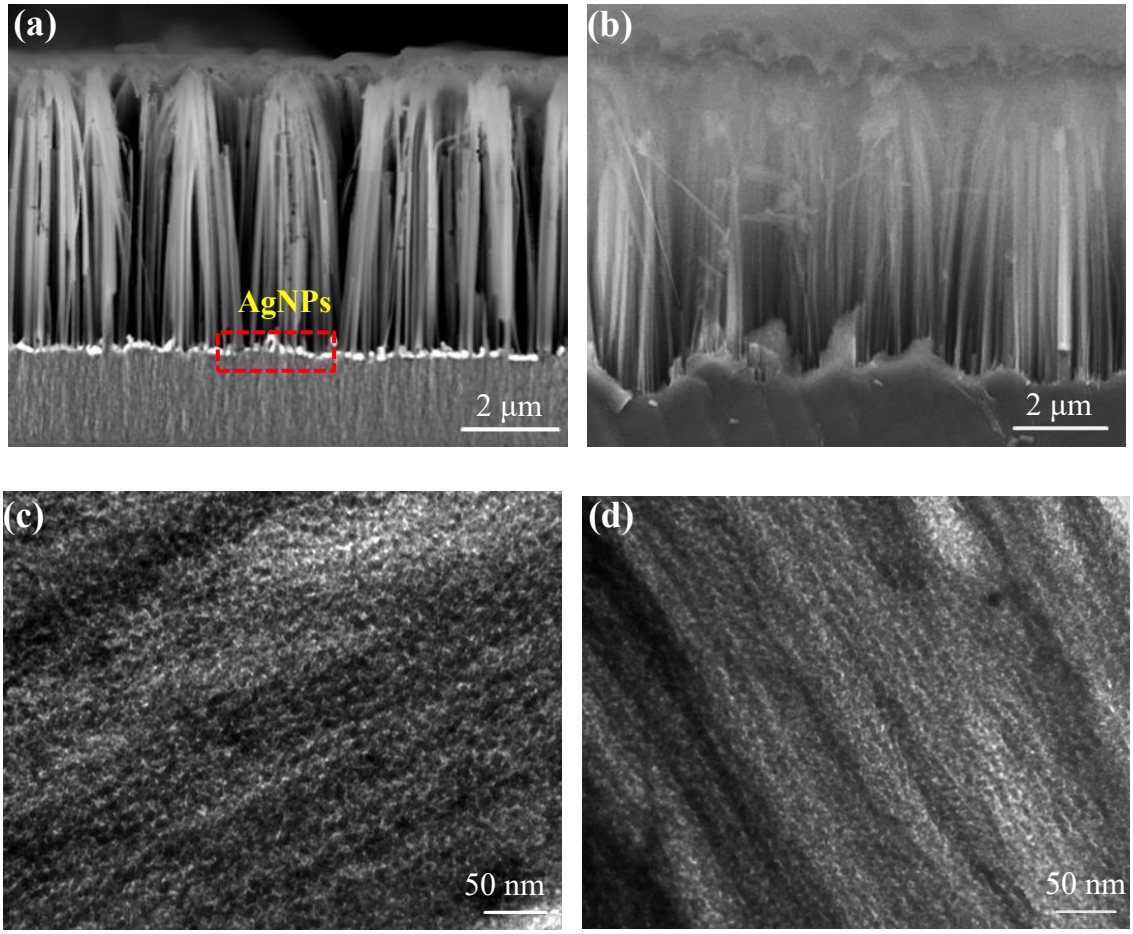

Figure 3.9 SEM cross-sectional images of highly n-type doped SiNWs (a) with and (b) without native AgNPs before hydrogen evolution; TEM micrographs of sidewall of SiNWs (c) with and (d) without native AgNPs before hydrogen evolution.

the characteristic reflex of the Si (400). The mean size of AgNPs is estimated by the Scherrer equation as 40 nm. The Ag reflex peaks cannot be observed after 65% HNO_3 treatment (*fig. 3.10 b*). It indicates that AgNPs are effectively removed by 65% HNO_3. TEM images in figure 3.9 (c) and (d) show that the surface of SiNWs with native AgNPs is rougher and more porous in comparison to the SiNWs without AgNPs.

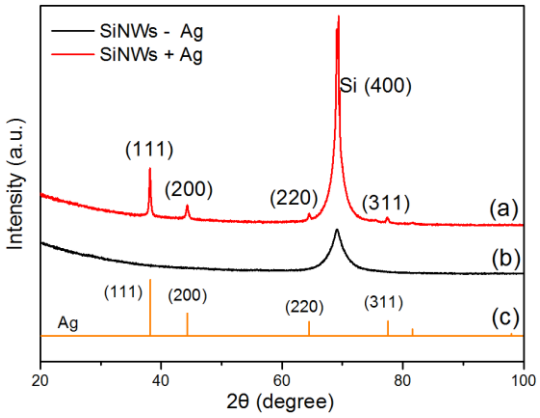

Figure 3.10 XRD diffraction patterns of SiNWs (a) with and (b) without native AgNPs. (c): Reference pattern of Ag [JCPDS Card No. 00-004-0783].

Absorption measurements of the n-highly doped SiNWs (a) without and (b) with native AgNPs are shown in Figure 3.11. The absorption of SiNWs with native AgNPs is lower than SiNWs without native AgNPs in the range of about 400-1500 nm. It could attribute to the different color of the surface. Due to the 65% HNO_3 treatment, the surface color of SiNWs without native AgNPs becomes deeper. As shown in Figure 3.11 inset, the surface color of SiNWs with and without native AgNPs is brown and gray, respectively. The deeper color can absorb more light. However, SiNWs with native AgNPs exhibits weakly higher absorption than SiNWs without native AgNPs from 200-400 nm. It is maybe attributed to isolated Ag^+ ions. [156]

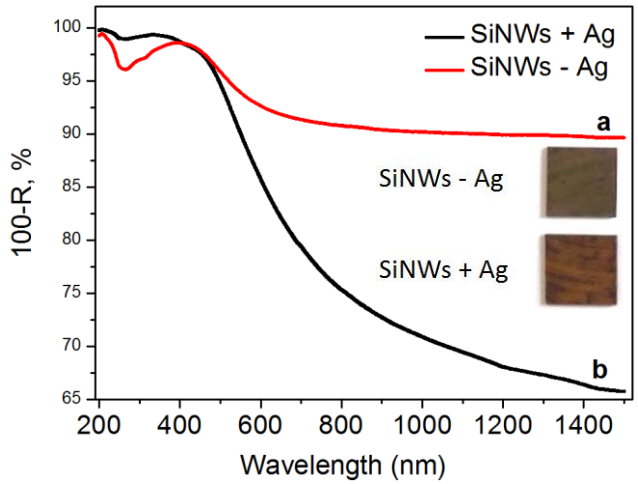

Figure 3.11 Absorption (100-R) spectra of n-highly doped SiNWs (a) without and (b) with native AgNPs.

3.3 Selection of appropriate hole scavager and ratio

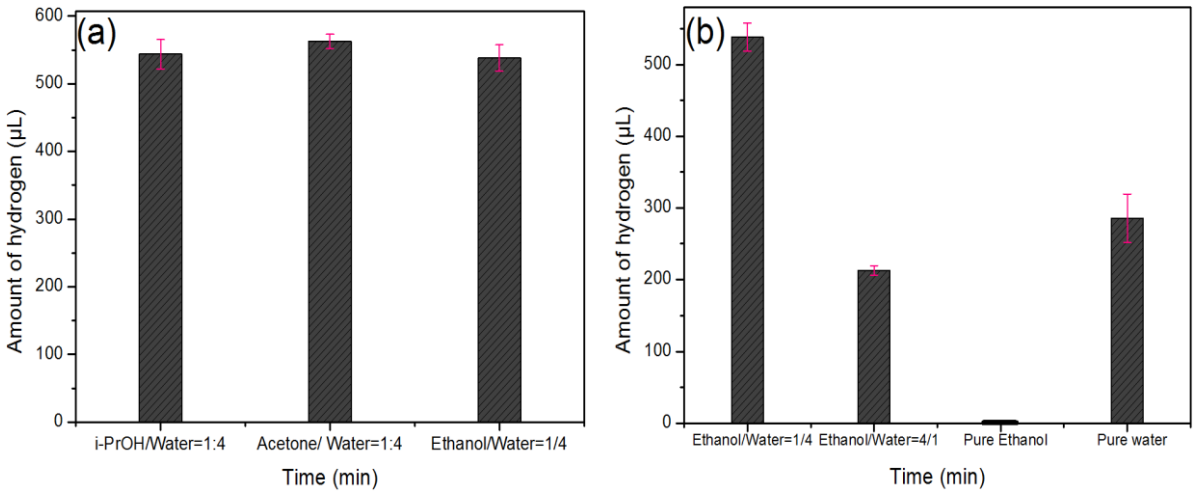

Figure 3.12 (a): Hydrogen amount of n-type highly doped SiNWs with native AgNPs in i-PrOH/water (1:4; v/v), acetone/water (1:4; v/v), and ethanol/water (1:4; v/v) solution; (b): Hydrogen amount of n-type highly doped SiNWs with native AgNPs in ethanol/water (1:4; v/v), ethanol/water (4:1; v/v), pure ethanol, and pure water. All hydrogen generation experiments were performed under white light irradiation for 3h.

As discussed in chapter **2.4**, ethanol is important for hydrogen generation of SiNWs in water. Ethanol was added to water to produce hydrogen for two main reasons: one is to decrease the surface tension as the SiNWs surface is very hydrophobic after etching. The other reason is ethanol, as a "hole-scavager", is easily oxidized by photo-generated holes and promotes the separation of photo-generated photos and holes. Ethanol is widely reported to enhance hydrogen generation as a hole scavager in water-based solutions. [157-159] Besides ethanol, other organic solvents (e.g. methanol, ethylene glycol) are also reported to promote hydrogen generation. [160-161] To select the appropriate hole scavager, isopropanol (i-PrOH) solution, acetone solution, and ethanol solution were employed to produce hydrogen as hole scavagers. The results are presented in Figure 3.12.

Figure 3.12 (a) shows that the amounts of hydrogen are not significantly different (about 550 μL) when the hole scavagers are isopropanol, acetone, or ethanol. It is because both hydroxyl and aldehyde are easily oxidized by the photo-generated holes. Considering that ethanol is inexpensive, ethanol is appropriate to be used as a hole scavager. Figure 3.12 (b) shows the amounts of hydrogen generated in different ratios of ethanol/ water solution. It is clear that when the ratio of ethanol/ water = 1:4, SiNWs can produce the most hydrogen. However,

when the ratio of ethanol to water = 4:1, one piece of 1×1 cm^2 SiNWs wafer can produce about 200 µL of hydrogen. It could be that ethanol molecules occupy the most surface of SiNWs and the water molecules are isolated from the SiNWs surface. Figure 3.12 (b) also shows that SiNWs cannot produce hydrogen in pure ethanol. There are two main reasons: firstly, pure ethanol cannot oxidize the surface of SiNWs because of the weak oxidation of hydroxyl. Secondly, the decomposition product of ethanol for photocatalysis is not hydrogen. The degradation of ethanol as complete photooxidation of ethanol was reported to form acetic acid and CO_2. [162] In pure water, one piece of 1×1 cm^2 SiNWs wafer can produce about 300 µL hydrogen. SiNWs produce about two times the amount of hydrogen in ethanol/water (1/4; v/v) solution than in pure water because ethanol as a "hole scavager" can promote the separation of photo-generated electrons and holes.

In general, ethanol is an appropriate "hole scavager". Ethanol (e.g. 25% ethanol) can enhance hydrogen generation, however, excess ethanol (e.g. 75% ethanol) suppresses hydrogen generation.

3.4 Influence of dopant type and doping level on the hydrogen generation

Figure 3.13 shows the hydrogen generation amount dependent on the exposition time under the white light irradiation by varying type and doping of SiNW matrixes. Figure 3.13 (a) and (b) show that both n-type lowly and highly doped SiNWs can produce hydrogen in darkness and under white light. Furthermore, more hydrogen was observed under white light than in darkness. The maximum growth rates of hydrogen amounts in white light than in darkness are about 33% (5 min) and 25% (30 min) for n-type lowly and highly doped SiNWs, respectively. Due to the higher surface area, n-type highly doped SiNWs can produce 2.5 times amount of hydrogen as n-type lowly doped SiNWs after 3 hours. Figure 3.13 (a) and (b) also show that hydrogen was not detected from silicon bulk regardless of the type and doping level. In theory, silicon bulk can produce hydrogen in water, however, due to the low surface area, the reaction is very slow. In addition, an oxide layer is quickly formed and inhibits further oxidation. As a result, the amount of hydrogen is too small to be detected (in our GC system, the limit of oxygen detection is about 40 µL). Furthermore, there is more hydrogen generation in white light than in darkness because of photocatalysis (see chapter **3.6.1**).

Hydrogen is not detected from p-type lowly doped SiNWs (*fig. 3.13* c). The reason is because of the smooth surface of p-type lowly doped SiNWs, as shown in Figure 3.2 (g). It indicates

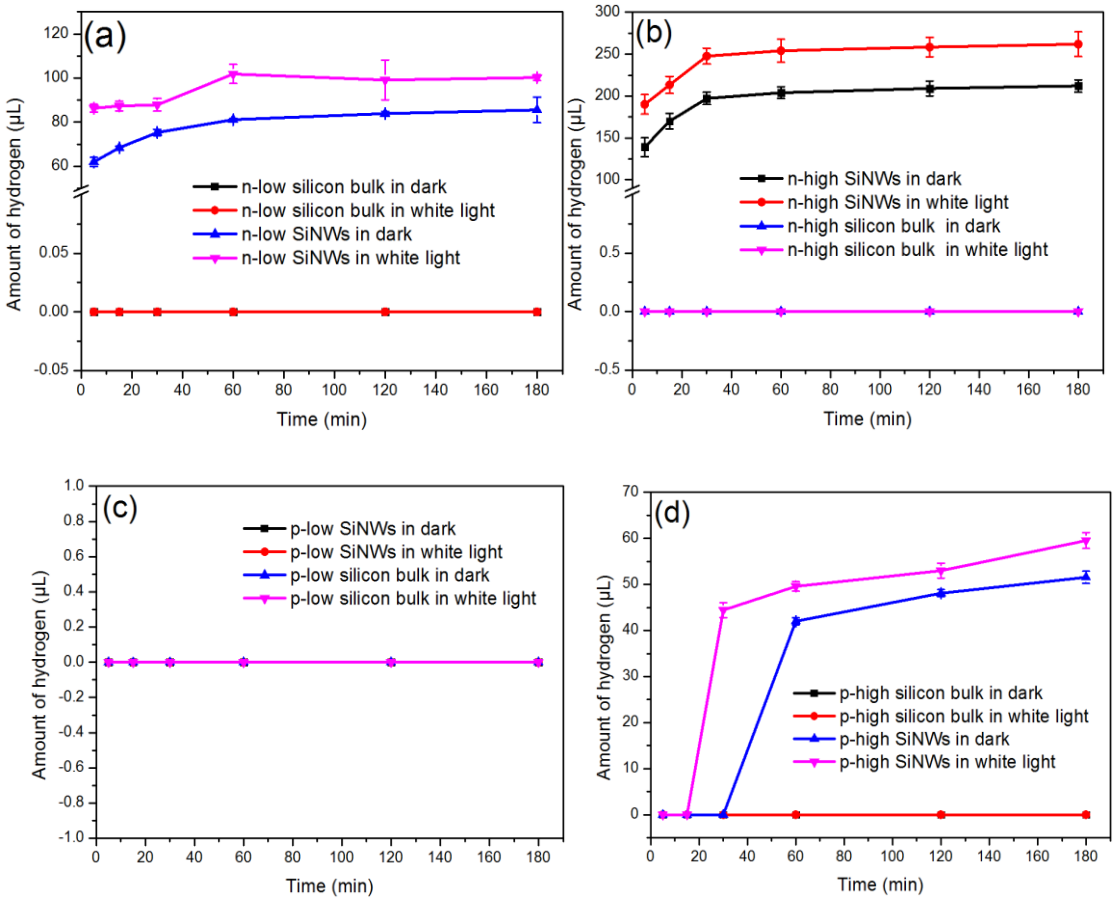

Figure 3.13 Hydrogen generation amount dependence on reaction time (5, 15, 30, 60, 120, 180 min) using: (a) n-type lowly doped SiNWs without AgNPs and silicon bulk; (b) n-type highly doped SiNWs without AgNPs and silicon bulk; (c) p-type lowly doped SiNWs without AgNPs and silicon bulk; (d) p-type highly doped SiNWs without AgNPs and silicon bulk in a water/ethanol solution (4:1; v/v) in the darkness and under white light irradiation. Each point was measured 2-5 times.

that the roughness of the surface of SiNWs strongly affects hydrogen generation. For p-type highly doped SiNWs, hydrogen is also not detected before 15 min and 30 min in white light and darknesses, respectively (*fig. 3.13* d). Due to the less rough surface (*fig. 3.2* h), p-type highly doped SiNWs produce about 60% and 11% hydrogen amount as n-type lowly and highly doped SiNWs in white light after 3 hours, respectively.

In general, n-type highly doped SiNWs produce the most hydrogen both in darknesses and in white light because of the rough surface. One piece of 1×1 cm^2 SiNWs wafer can produce about 250 µL and 160 µL hydrogen in white light and darknesses after 3 hours, respectively. Therefore, comparing the different types and doping levels, selecting n-type highly doped SiNWs is the best choice to produce hydrogen.

3. 5 Optical excitation wavelength influence to the hydrogen generation

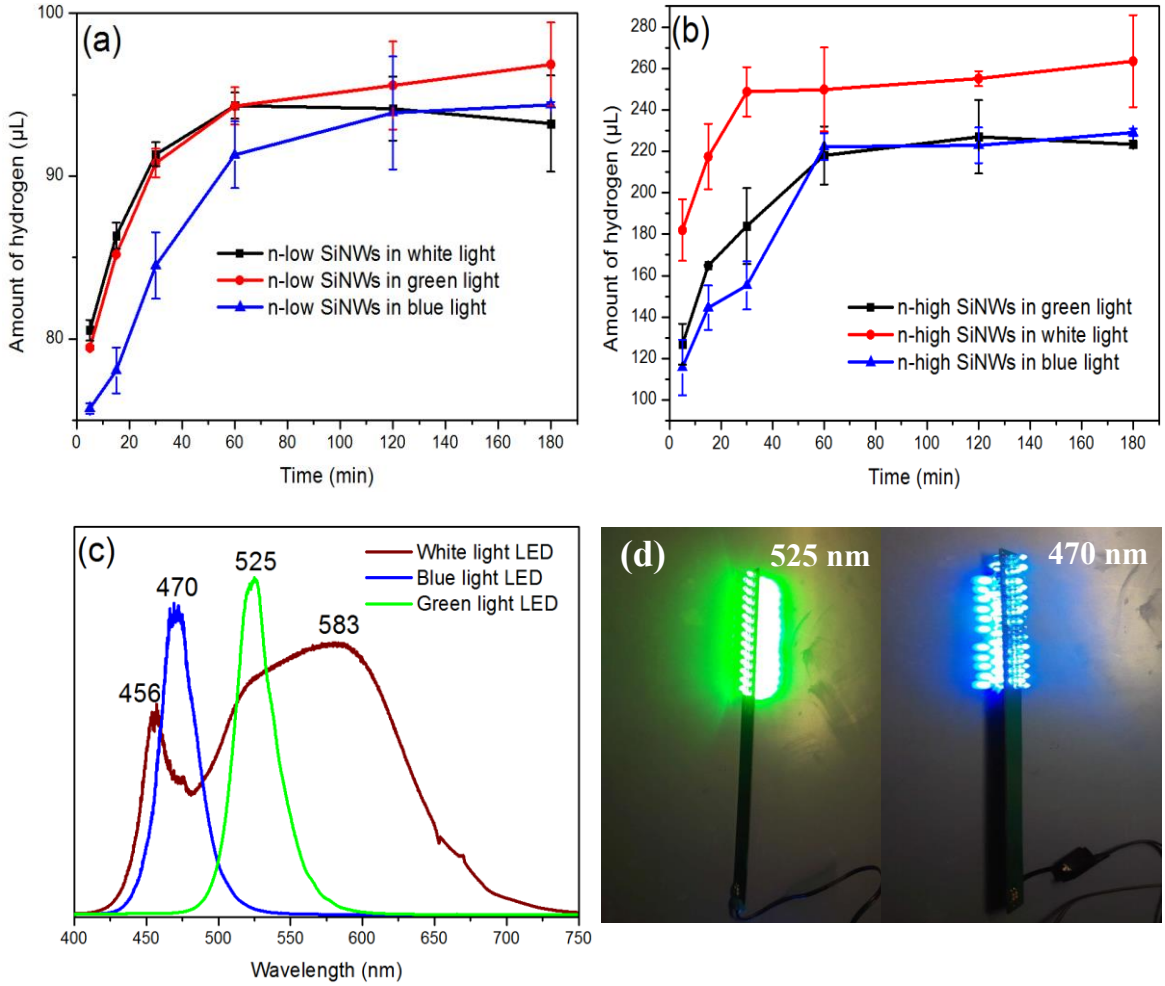

Figure 3.14 Dependence of amount of generated hydrogen on the exposition time (5, 15, 30, 60, 120, 180 min) using (a) n-type lowly doped SiNWs without AgNPs; (b) n-type highly doped SiNWs without AgNPs under white, green and blue light irradiation. The liquid media was a water/ethanol solution (4:1; v/v); (c) the spectrum of white(400-750 nm, 33 mW/cm^2, green (525 nm, 8 mW/cm^2) and blue light (470 nm, 3 mW/cm^2); (d) the digital images of green and blue LED. Each point was measured 2-5 times.

Due to the very weak hydrogen generation of p-type SiNWs, n-type SiNWs are employed to investigated system excitation wavelength influence on the hydrogen generation. N-type lowly and highly doped SiNWs are irradiated in three kinds of light: white light (400-750 nm), green light (525 nm) and blue light (470 nm). The power of these three kinds of light is 33 mW/cm^2, 8 mW/cm^2 and 3 mW/cm^2, respectively.

Figure 3.14 shows that there is no clear distinction of hydrogen amounts when the SiNWs matrix is irradiated under white, green and blue light. The most visible distinction of the hydrogen amount depending on the excitation light source is presented in the first hour of exposition. For the n-type lowly doped SiNWs, a similar hydrogen amount after 60 min of exposition was observed for the white and green light, and in the system irradiated with the blue light source the generated amount of hydrogen was significantly lower. For the n-type highly doped SiNWs, SiNWs produce about 15% more hydrogen under white light than in green and blue light. The results may be explained as follow: white light has the highest power (33 mW/cm^2) in all applied light sources, it denotes more white light photons reach the surface of SiNWs and are utilized in the photocatalysis. Although Ultrasoft X-ray Emission Spectroscopy and X-ray Absorption Near-Edge Structure indicate the presence of SiO_x on the surface of SiNWs (Chapter **3.6.4**), based on our observation, the nanostructure of SiNWs quickly became SiO_2 powder. Moreover, therefore, SiO_x hardly influences the hydrogen generation under green and blue light.

3.6 Influence of SiNWs decorated with AgNPs on the hydrogen generation

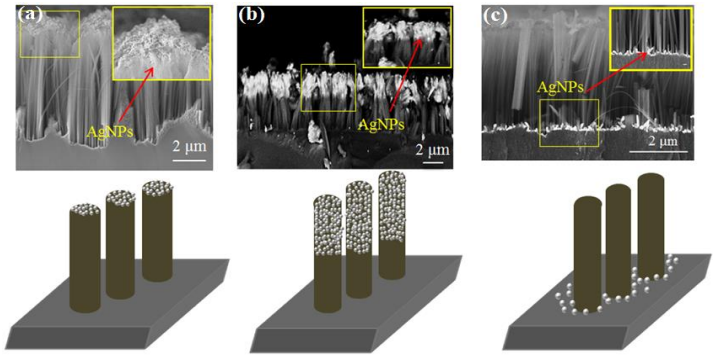

Figure 3.15 SEM cross-sectional view and schematic diagram of n-type highly doped SiNWs array decorated with AgNPs by (a) ELD; (b) MR and (c) native AgNPs. All experimental details are presented in Chapter **2.2**.

As Chapter 2.2 introduced, SiNWs are decorated with AgNPs by three methods: ELD, MR and native AgNPs. These three methods decorate SiNWs with AgNPs at the top, middle, and bottom, respectively (*fig.* 3.15). Based on the results observed in chapters **3.13**, we found that n-type highly doped SiNWs are more favorable for efficient hydrogen generation. For that reason, n-type highly doped SiNW matrixes with different silver functionalization have been employed to investigate the hydrogen generation.

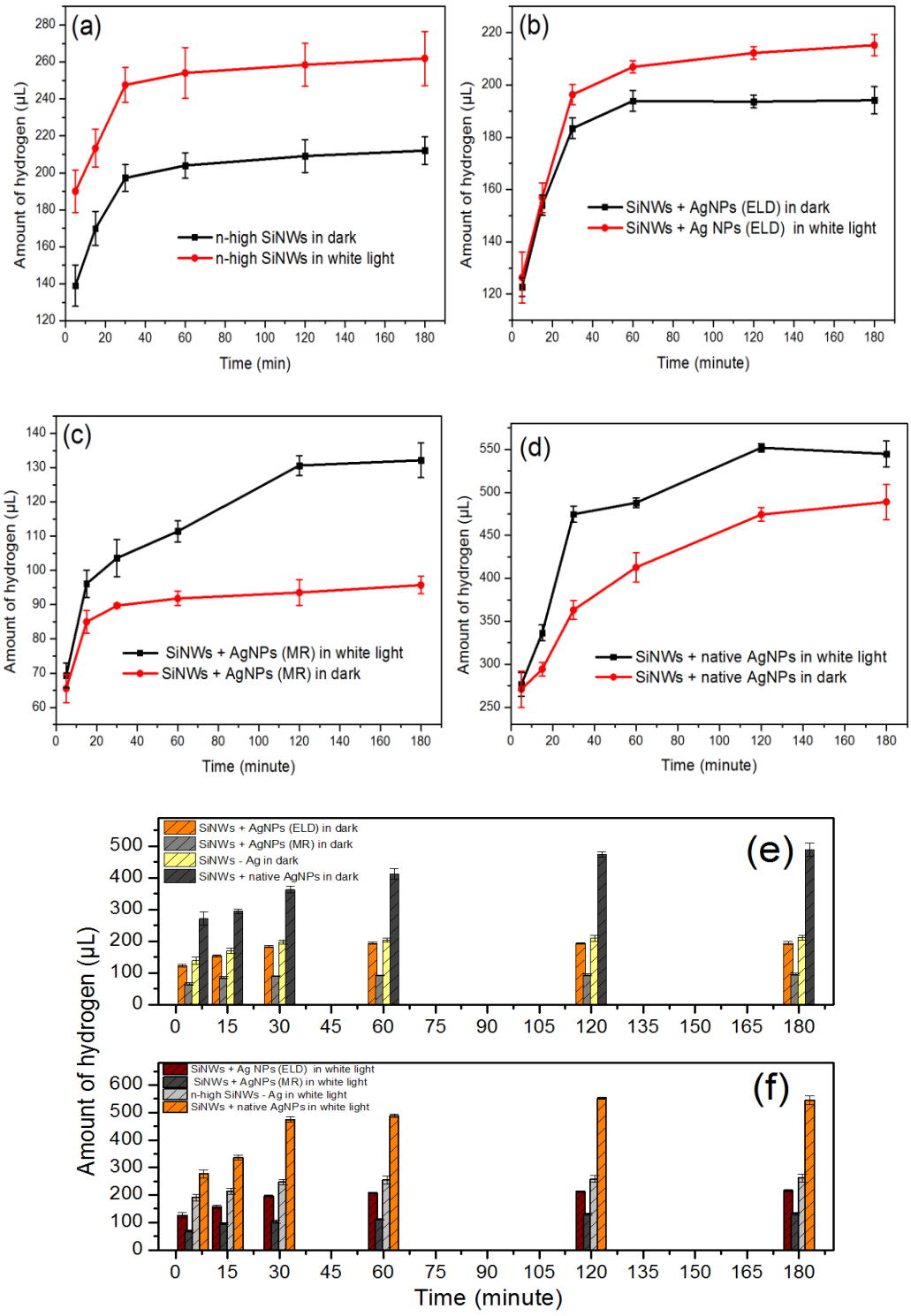

Figure 3.16 Generated hydrogen amount dependence on the system exposition time (5, 15, 30, 60, 120, 180 min) in a water/ethanol solution (4:1; v/v) in the darkness and under white light irradiation (a) SiNWs without AgNPs; (b) SiNWs with AgNPs (ELD); (c) SiNWs with AgNPs (MR) and (d) SiNWs with native AgNPs, respectively; (e) Comparaison of SiNWs with and without AgNPs in darkness and (f) under white light irradiation, respectively. Each point was measured 2-5 times.

The dependence of generated hydrogen amount on the system is exposure time to white light irradiation with and without AgNPs decorated n-type highly doped SiNWs matrices is shown in Figure 3.16. We observe that both nanostructured SiNWs with and without AgNPs can effectively produce hydrogen in darkness and under white light irradiation. SiNWs without AgNPs produce 9.3% and 22% more hydrogen amount than SiNWs decorated with AgNPs (ELD) in darkness and under white light after 3 hours, respectively. The weakest hydrogen generation was observed from the SiNWs matrix decorated with AgNPs by applying silver mirror reaction. SiNWs decorated with AgNPs (MR) only produce 45% and 50% hydrogen amount as SiNWs without AgNPs in darkness and under white light after 3 hours, respectively. The highest and more efficient hydrogen generation was observed for the SiNWs matrix decorated with native AgNPs which are densely distributed in the interface between SiNWs array and bulk part of silicon wafer as shown in Figure 3.15 (c). The fast three times higher hydrogen amount was observed for the “native” AgNPs decorated SiNWs in comparison to the ELD AgNPs or silver free SiNWs matrices both in darkness and under white light, respectively.

SEM images of SiNWs without and with AgNPs are performed after hydrogen evolution in Figure 3.17. Figure 3.17 a (SiNWs without AgNPs) shows that SiNWs become “silica powder” after hydrogen evolution. Figure 3.17 b (SiNWs with AgNPs by ELD) exhibits the analogous status, AgNPs are mixed with the silica powder. Very short SiNWs are observed from Figure 3.17 c (SiNWs with AgNPs by MR), AgNPs cover the SiNWs surface and form AgNPs@ SiNWs shell-core nanostructure. Interesting, for SiNWs with native AgNPs, the nanostructure of SiNWs is almost the same as initial SiNWs array that before hydrogen evolution, even after 24 hours in water/ethanol (4:1; v/v) solution. The length of SiNWs with native AgNPs before and after hydrogen evolution was about 7 μm. SiNWs stick together and form a “SiNWs film”. The material object of SiNWs with and without native AgNPs wafer also shows a totally different surface after hydrogen generation (Figure 3.17 a and d insets): For SiNWs without AgNPs, the surface becomes bright after hydrogen generation, however, for SiNWs without native AgNPs, a gray SiNWs layer still can be seen after hydrogen generation.

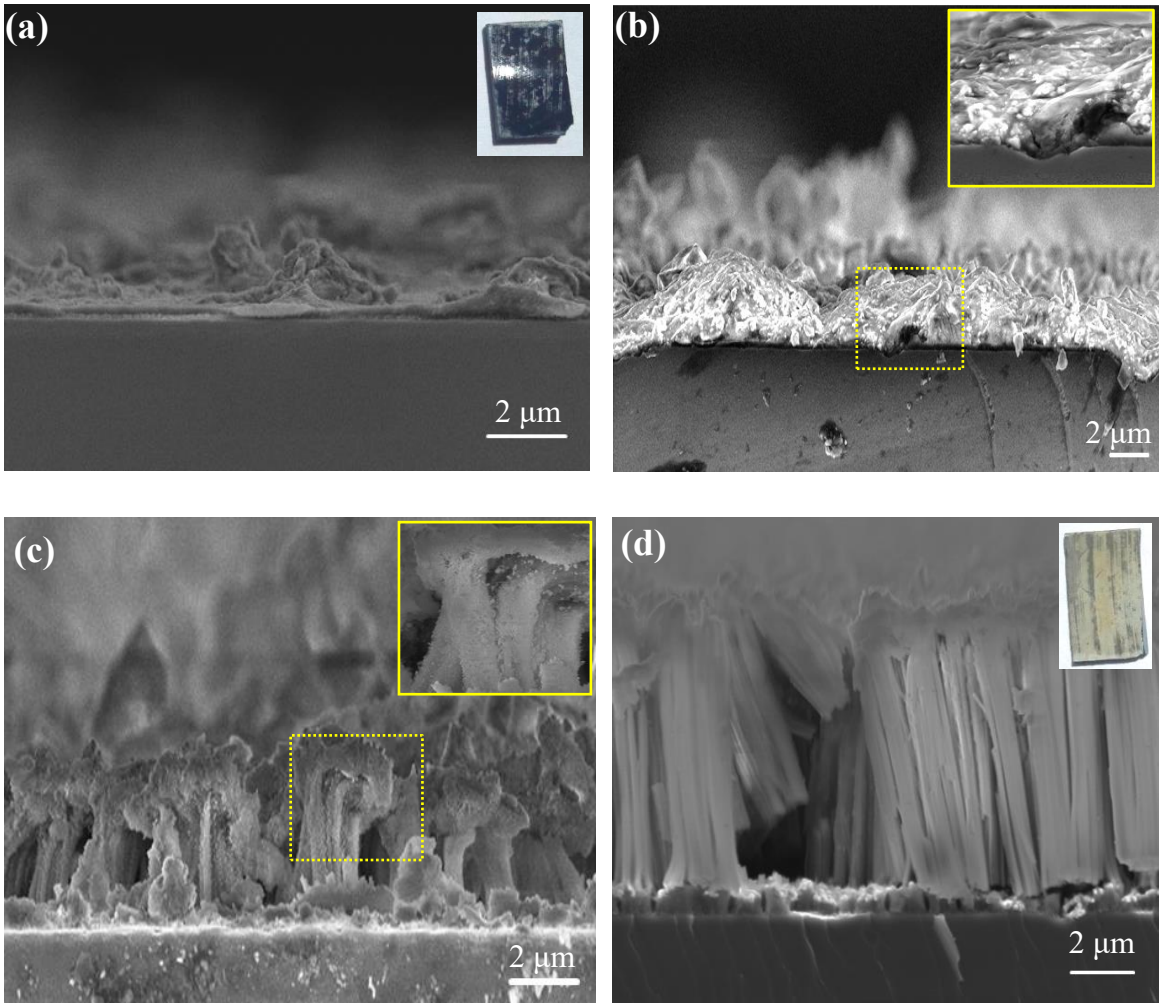

Figure 3.17 SEM cross-sectional view of SiNWs (a) without AgNPs and with AgNPs by (b) ELD ,(c) MR, (d) native ANPs after 3h hydrogen evolution. Insets: (a) is the image of SiNWs without AgNPs wafer surface after hydrogen generation. (b) and (c) are the zooms of SiNWs surface area after hydrogen generation. (d) is the image of SiNWs with native AgNPs wafer surface after hydrogen generation.

For SiNWs with AgNPs (ELD), because the AgNPs only stay at top of SiNWs, SiNWs still can be fully oxidized. During the oxidation, the nanostructure collapse and AgNPs transform into "silica powder" (Fig. 3.17 b). Due to the MR method can form AgNPs@SiNWs shell-core nanostructure, AgNPs protect SiNWs to suffer oxidation in water. Therefore, a part of SiNWs is saved (Fig. 3.17 c). It could be one reason that SiNWs with AgNPs by MR produce much less hydrogen but for a longer time than SiNWs without AgNPs.

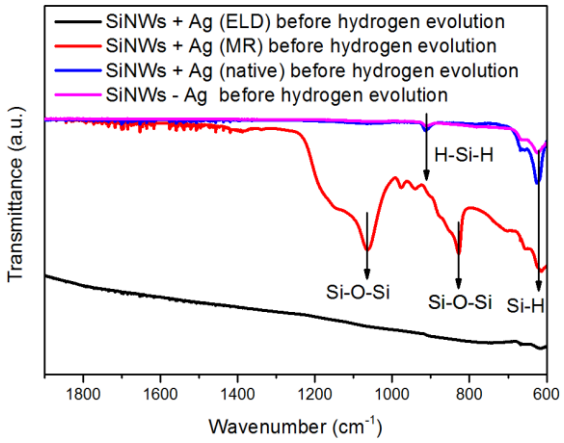

Figure 3.18 IR spectra of the SiNWs without and with AgNPs by ELD, MR and native AgNPs before hydrogen evolution.

Probably, the main reason for such effect is related to the surface structure and composition of SiNWs after different surface treatments. To investigate the surface of SiNWs chemical composition changes/stability during the hydrogen evolution and presence of AgNPs the vibrational IR spectroscopy was applied.

From the IR spectra of the SiNWs with AgNPs by MR before hydrogen evolution, two strong Si-O-Si peaks can be seen at 1065 cm^{-1} and 825 cm^{-1}. [163] It indicates SiNWs were consumed during the AgNPs decoration by MR method. Also, SiNWs were consumed by ELD method due to SiNWs reacted with $AgNO_3$. From IR spectra in Figure 3.18, it is clear that more SiNWs are consumed during MR decoration, therefore, SiNWs with AgNPs by MR produce the least hydrogen amount. Interesting, SiNWs with native AgNPs can produce about 81%-132% more hydrogen than SiNWs without AgNPs in darkness. As Figure 3.9 shows, SiNWs with native AgNPs have rougher surface than SiNWs without AgNPs. Therefore, SiNWs with native AgNPs could produce much more hydrogen. From the comparison of hydrogen generation of SiNWs without and with AgNPs by different methods, it demonstrates the surface of SiNWs strongly influences the hydrogen amount. The rougher surface and no-oxidation surface before hydrogen evolution can produce more hydrogen. Moreover, due to the rougher surface, SiNWs with native AgNPs can produce hydrogen longer time. SiNWs without AgNPs and with AgNPs by ELD almost cannot produce hydrogen in darkness after 30 min, however, SiNWs can continuously produce hydrogen in 3 hours.

Comparing the hydrogen generation in light, SiNWs without AgNPs produce 25% more hydrogen amount than in darkness, SiNWs with AgNPs by ELD produce 10% more

hydrogen amount than in darkness, SiNWs with AgNPs by MR produce 40% more amount hydrogen than in darkness and SiNWs with native AgNPs produce 29 % more hydrogen amount than in darkness at 120 min. In general, SiNWs with AgNPs by ELD have the least hydrogen increase and SiNWs with AgNPs by MR have the most hydrogen increase. It may be the reason that for SiNWs with AgNPs by ELD the AgNPs on the top of SiNWs suppresses the light absorption, and for SiNWs with AgNPs by MR, AgNPs on the sidewall of SiNWs plays as photogenerated electrons transport, which can promote the separation of photogenerated electron-hole. Still, Because of the roughest surface, SiNWs with native AgNPs can produce the most hydrogen in light. SiNWs with native AgNPs can produce 51%-115% more hydrogen than SiNWs without AgNPs in light.

In general, SiNWs with native AgNPs can produce the most hydrogen both in darkness and in light because of the roughest surface. SiNWs with AgNPs by MR produce the least hydrogen both in darkness and in light but the most increase in light than in darkness due to SiNWs are consumed during the decoration and the AgNPs protect the SiNWs to be oxidized in water, the AgNPs on the sidewall of SiNWs plays as photogenerated electrons transport to promote the separation of photogenerated electron-hole.

3.7 Hydrogen generation mechanism studies

3.7.1 System photosensitivity studies

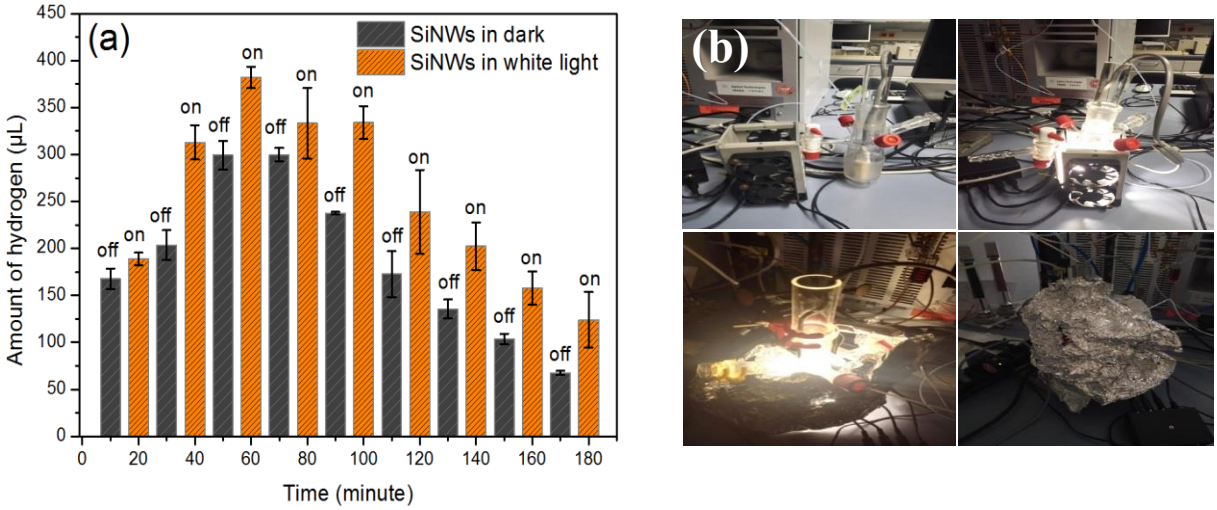

Figure 3.19 (a): Generated hydrogen amount dependence on reaction time in water/ethanol solution (4:1; v/v) by switching on and off the white light every 10 minutes using SiNWs with native AgNPs; (b) digital images of set-up system used in this experiment. The details of this experiment are presented in Chapter 2.4.

Although SiNWs can generate more hydrogen under white light than in darkness, photo-stimulated hydrogen evolution is not yet concluded unambiguously. As *fig.*3.13 shows, SiNWs can produce hydrogen by reaction with water in the darkness. Therefore, the subtle differences between different SiNWs (for example, etching time, etching temperature, etc.) will result in a different amount of hydrogen generation. To make sure there is photo-photocatalysis process, another experiment was designed to investigate it (Chapter **2.4**: automatic injection part). This experiment excludes influencing factors of preparation and hydrogen generation process because the SiNWs matrix only needs to compare itself. The results are shown in Figure 3.19 (a). In the first 10 minutes in the darkness, hydrogen is detected, then more hydrogen is generated in the next 10 minutes in the white light. Hydrogen amount is still increasing at 30 min in darkness due to the SiNWs surface oxidation. However, the amount of hydrogen decreases at 50 min in the darkness and increases at 60 min after under white light for 10 min. As the automatic injection part experiment introduces, it is not a completely closed system because of the connection from GC to the reactor. Hence, hydrogen can leak when more and more hydrogen is generated. The decrease of hydrogen amount at 50 min denotes that the loss rate of hydrogen is higher than the generation rate in darkness. The dramatically increase at 60 min indicates that the generation rate is higher than the loss rate in the darkness. The same tendency as from 40 min to 60min continues until the end of the experiment. This result strongly proves that SiNWs can produce more hydrogen in white light than in the darkness. This effect is related to the photoresponse of the SiNWs system to the external photon source. This is direct evidence of photosensitivity of the system under investigation with clear photoresponse.

Considering the surface passivation with hydrofluoric acid in the MAWCE process leads into the surface Si-H termination (or hydrogen storage in the porous matrix), [164] direct cleavage of Si-H bonds in the white light is one for a possible way to produce hydrogen in white light in the system of interest. For this reason, the following experiment was performed to prove the hydrogen amount produced due to surface passivation. SiNWs matrix was fixed in the empty vial following by the irradiation in white light and darkness for 3 hours. Figure 3.20 (a) shows that a small amount of hydrogen was generated in empty vial both in darkness and white light. The amount is almost the same. SiNWs produce hydrogen in empty in darkness could be the highly reductive activity of Si-H bonds. [165] Si-H bonds were oxidized by oxygen and form hydrogen. The almost same hydrogen in white light indicates that the direct cleavage of Si-H bonds is hard in white light. Therefore, the increasing amount of hydrogen

in white light in water (about 119 µL) is from the photocatalysis process. This direct experiment is clear evidence of the very minor influence of surface adsorbed hydrogen to the total generated hydrogen amount under white light irradiation for 3h. Figure 3.20 (b) shows that the pH value of water/ethanol solution was not changed both in darkness and white light, it denotes that Si-H bonds were not dissolved in the water during the hydrogen generation. In summary, the increased hydrogen generation in white light is not a direct cleavage of Si-H bonds, but additional evidence to the photocatalysis process in the applied system.

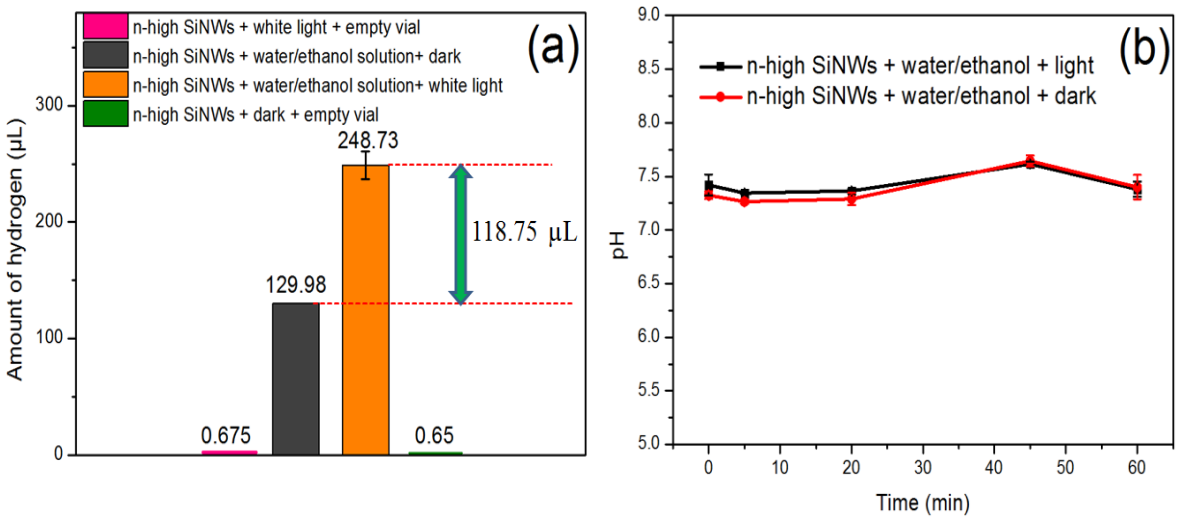

Figure 3.20 (a)**:** Hydrogen amount of n-type highly doped SiNWs without AgNps in empty vial and water/ethanol solution (4:1; v/v) in darkness and white light for 3h, respectively; (b): pH value of water/ethanol solution (4:1; v/v) containing n-type highly doped SiNWs in white light and darkness at different time. Each point was measured 2-5 times.

3.7.2 Surface passivation: with -H and oxidation of silicon

Erogbogbo et al. reported that 10-100 nm size silicon nanoparticles can produce hydrogen without light, heat, or electricity. [166] It demonstrated that the nanosized silicon can react with water and generate hydrogen due to the silicon oxidation processes. The following chemical reaction can take place:

$$Si + 4H_2O \rightarrow Si(OH)_4 + \mathbf{2H_2} \uparrow \qquad (1)$$

$$Si + 2H_2O \rightarrow SiO_2 + \mathbf{2H_2} \uparrow \qquad (2)$$

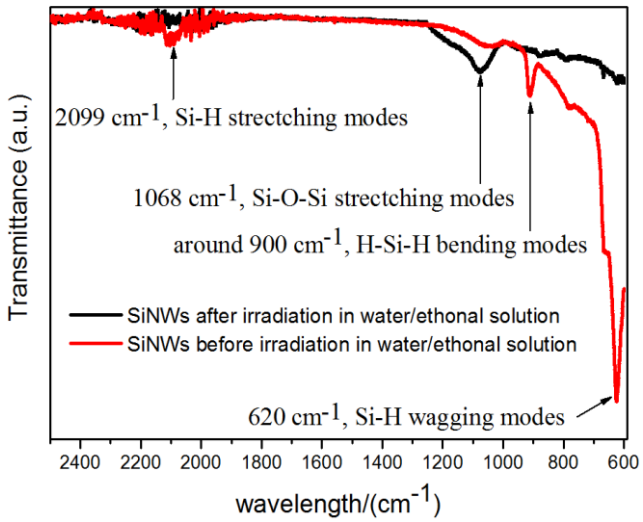

Figure 3.21 IR spectra of the SiNWs without native AgNPs before and after irradiation (3h) in water/ethanol (4:1; v/v) solution.

SiNWs (2D system) are different from silicon nanoparticles (1D system), however, from SEM studies presented before in *Fig. 3.2 e* and *f,* it shows that the diameter of n-type SiNWs is about 50 nm. It denotes that it is also possible to generate hydrogen via direct silicon oxidation of the silicon surface.

To investigate the SiNWs surface oxidation, IR spectra of SiNWs before and after irradiation in water/ethanol (4:1; v/v) solution was performed (*fig.* 3.21). Before irradiation in water/ethanol (4:1; v/v) solution, the surface of SiNWs is H-terminated with hydrogen bonds as reflected in the presence of characteristic Si-H vibrational modes at 620, 912 and 2099 cm^{-1} as shown in *Fig. 3.21*.[167] After 3 h irradiation in water/ethanol (4:1; v/v) solution, all Si-H bonds vanish and asymmetric Si-O stretching modes at above 1068 cm^{-1} (ref. 167) become clearly visible. These results are clear evidence of Si-H passivated SiNWs surface oxidation in water.

From SEM micrographs presented in Figure 3.22 (a) and (b) it is clearly visible that after hydrogen evolution experiment the primary SiNWs morphology has been changed. For n-type lowly doped SiNWs, the morphology after hydrogen evolution looks the same as before, but it is clear to observe the surface of SiNWs is charged. A lot of black spots can be seen on the surface. For n-type highly doped SiNWs, the morphology after hydrogen evolution is destroyed completely. Only silica powder can be seen on the silicon substrate. The color of the SiNWs wafer surface also demonstrates the SiNWs nanostructure is destroyed. Before hydrogen evolution, the surface of n-type highly doped SiNWs is brown (*fig.3.22* c inset), it

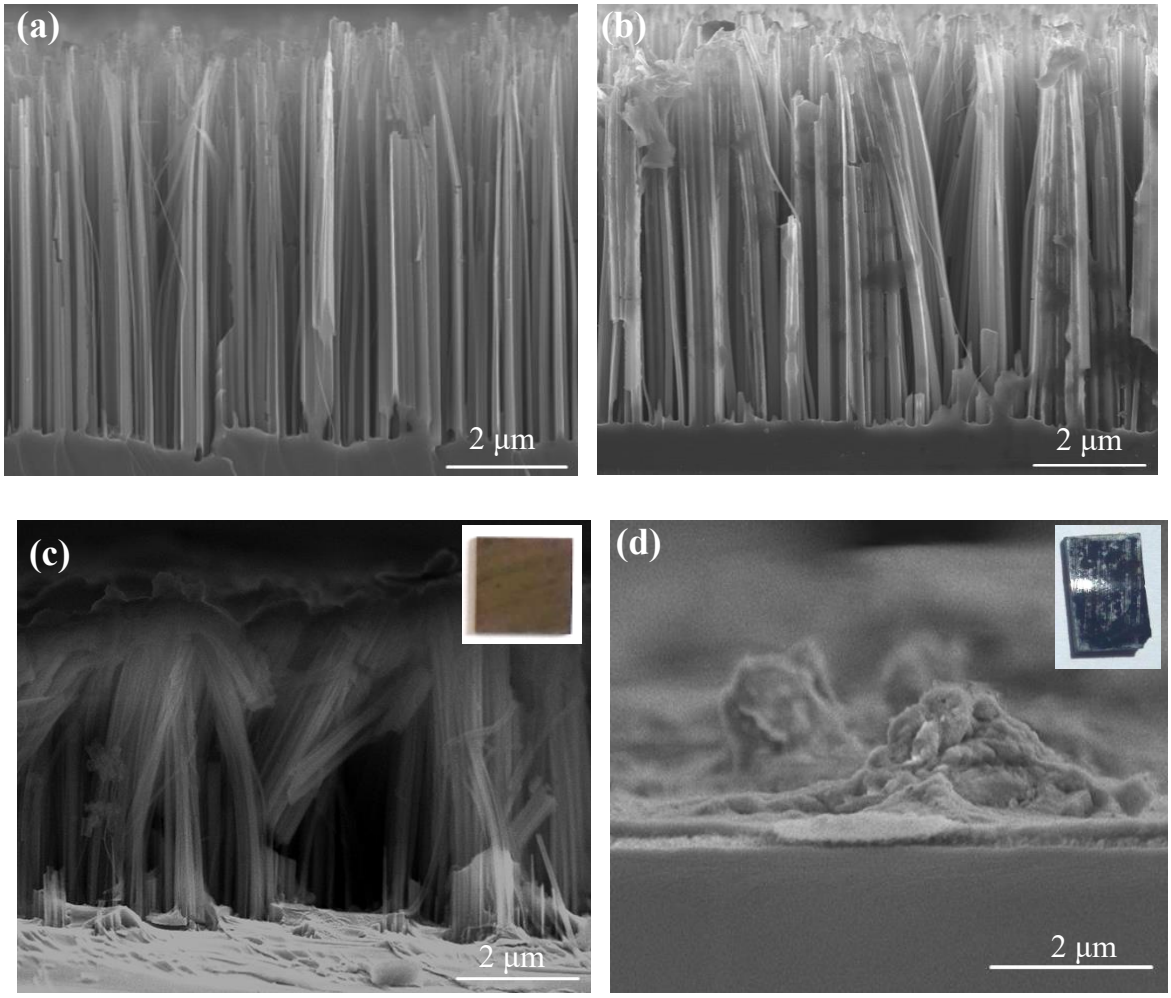

Figure 3.22 SEM cross-sectional view of n-type lowly and highly doped SiNWs without AgNPs before (a, c) and after (b, d) irradiation in water/ethanol solution (4:1; v/v), respectively. Insets: image of SiNWs without AgNPs surface (c) before and (d) after hydrogen evolution.

becomes bright after hydrogen generation (*fig.3.22* d inset). The different morphologies after hydrogen evolution indicate that the doping level of silicon can strongly affect the oxidation in water. Water molecules can only oxidize the shallow surface of the n-type lowly doped SiNWs but the deeper surface of n-type highly doped SiNWs. It could be the porous silicon surface is easier to be oxidized. Due to the less rough surface of n-type lowly doped SiNWs in water, much fewer hydrogen amounts were produced both in darkness and in white light than n-type highly doped SiNWs (*fig. 3.13*). It is well-known the oxidation of nanostructured silicon at ambient conditions (300K) has a self-limiting character that means the complete silicon oxidation is prohibited due to the natural properties of silicon. [168] Based on that the

part of hydrogen produced via silicon oxidation can be observed only for the limited time period that strongly correlates with our GC results presented in Figure 3.13.

3.7.3 H_2 evaluation dependence on the surface area

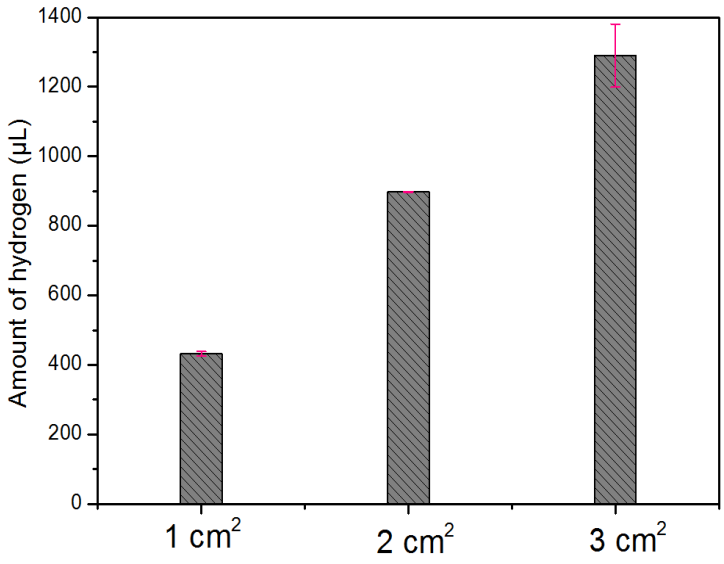

Figure 3.23 Hydrogen amount of highly doped SiNWs with native AgNPs in a water/ethanol solution (4:1; v/v) in white light for 3h using 1 cm^2, 2 cm^2, and 3 cm^2 of SiNWs. Each point was measured 2-5 times.

The hydrogen generation using the different surface area of SiNWs are given in Figure 3.23. 2 cm^2 and 3 cm^2 of SiNWs can produce 2.1 and 3.0 times hydrogen amount as 1 cm^2 of SiNWs. The results indicate that the hydrogen generation depends on the surface area of SiNWs wafers. As discuss above, there are three ways to produce hydrogen for SiNWs in water (*fig. 3.24*): The first way is SiNWs are oxidized by H_2O molecules and form SiO_X or SiO_2 layer. This way produces 52% and 80% amount of hydrogen for SiNWs without and with native AgNPs, respectively. The second way is photocatalysis. Si and SiO_x play as photocatalysts to produce hydrogen during the irradiation. The photocatalysis way produces less hydrogen than oxidation of SiNWs. The third way is the cleavage of dangling H bonds. As discussed in chapter **3.6.1**, H-terminated surface is hardly modified directly by light, however, they can be replaced by -OH of H_2O molecules. The -H passivated SiNWs surface during the oxidation give additionally one hydrogen atom due to the damage of Si-H bond. This way produces very small amount of hydrogen. These three ways of producing hydrogen are related to the surface area. Therefore, the amount of hydrogen generation strongly depends on the surface area of SiNWs.

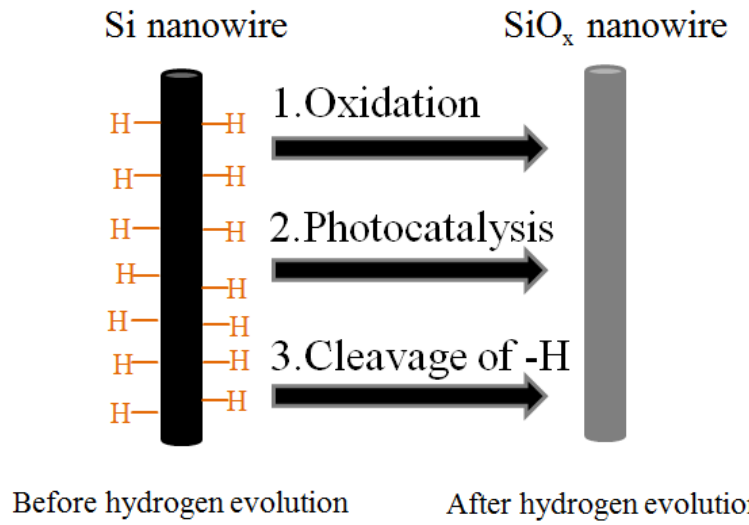

Figure 3.24 The schematic model of SiNWs produces hydrogen in water.

3.7.4 Atomic, electronic structure and composition of initial SiNWs

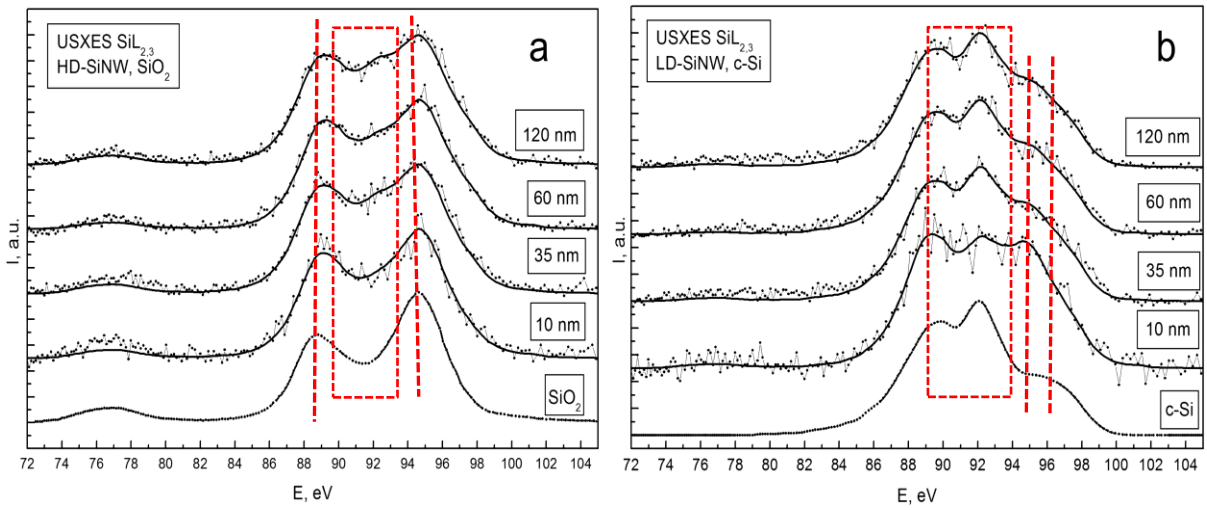

Figure 3.25 USXES Si $L_{2,3}$ spectra of (a) highly doped (HD) and SiO_2. (b) lowly doped (LD) and c-Si.

Investigation of the atomic and electronic structure of SiNWs is important to understand the hydrogen generation of SiNWs in water. However, such investigation of MAWCE SiNWs has not been widely reported. For this purpose, two non-destructive highly surface-states sensitive X-Ray spectroscopy methods using synchrotron irradiation are used to investigate the surface composition and electronic structure of SiNWs: Ultrasoft X-ray Emission Spectroscopy (USXES) and X-ray Absorption Near-Edge Structure (XANES). USXES is a type of X-ray spectroscopy where the sample is bombarded with ultra-low energy (<1 keV) X-rays and the energies and intensities of the X-rays emitted due to valence-to-core

transitions are detected. XANES provides means of probing the partially occupied density of electronic states of a material. [169-172] Both of them provide information about the Si or O atomic surroundings of the surface and the electronic structure of SiNWs.

Si $L_{2,3}$ USXES spectra of n-type lowly and highly doped SiNWs are presented in Figure 3.25. The analysis depth of the surface is from 10 nm to 120 nm. For highly doped SiNWs, the Si $L_{2,3}$ USXES spectra are similar to SiO_2. However, The shoulder becomes weaker and peaks around 89 eV and 95 eV right-shift with the deeper analysis (Figure 3.25 (a)). It denotes the surface is not only SiO_2 but also containing silicon suboxides (SiO_x). Figure 3.24 (b) shows that the Si $L_{2,3}$ USXES spectra of lowly doped SiNWs is similar to c-Si. However, a peak of 95 eV can be observed from SiNWs but is not seen from c-Si. In the range of 89-94 eV, the slope flattens, and at the position around 96 eV, the slope becomes steep. It indicates that the surface of lowly doped SiNWs is not only Si.

Table 1 Composition of highly doped and lowly doped SiNWs surface with different depth.

Sample	Depth (nm)	c-Si, %	SiO_2, %	SiO_x, %	Measurement error, %
HD SiNWs	10	0	35	65	8
	35	13	37	50	8
	60	19	34	47	6
	120	24	42	34	6
LD SiNWs	10	45	22	33	6
	35	67	13	20	10
	60	72	8	20	7
	120	74	11	15	10

The surface composition of highly doped and lowly doped SiNWs based on USXES spectra measurement is shown in Table 1. For highly doped SiNWs, the amount of c-Si is increased from 0% to 24% when the depth is increased from 10 nm to 120 nm. And the amount of SiO_x is decreased from 65% to 34% when the depth is increased from 10 nm to 120 nm. In contrast, for lowly doped SiNWs, the amount of c-Si is increased from 45% to 74% when the depth is increased from 10 nm to 120 nm. And the amount of SiO_x is decreased from 33% to 15% when the depth is increased from 10 nm to 120 nm.

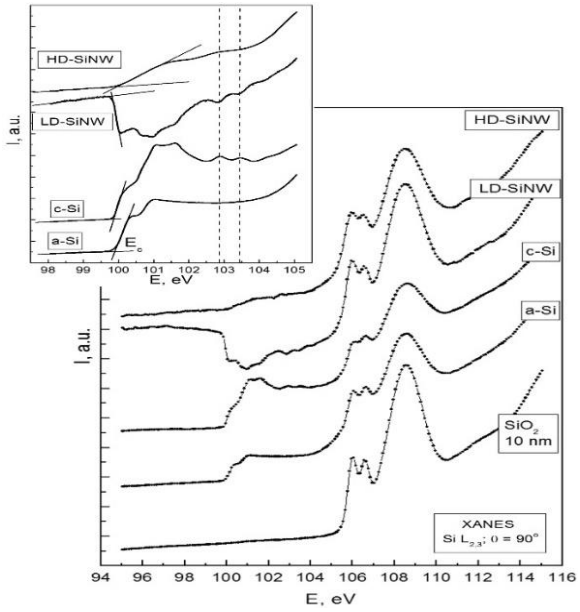

Figure 3.26 XANES Si $L_{2,3}$ spectra of n-type lowly and highly doped SiNWs.

Si $L_{2,3}$ XANES spectra of n-type lowly and highly doped SiNWs are presented in Figure 3.26. In the region till 105 eV (c-Si) for highly doped SiNWs a weak peak is visible that means the presence of elementary silicon in the surface layers up to 5 nm; the low intensity corresponds that the c-Si has weak influence on the surface composition that also correlates with USXES results; the high amorphization degree is evidence of highly disordered surface up to 5 nm in depth.

The presence of SiO_x and SiO_2 were also confirmed in our published work. [173] Local surroundings of the silicon and oxygen atoms character confirm the uniformity of the silicon oxides coverage of formed SiNW arrays at the surface atop layers, that did not exceed 10 nm, and their bulk part after in-situ mechanical removal (approx. 2μm) of the formed nanowires. The results obtained by us convincingly testify to the homogeneity of the phase composition of the sidewalls of SiNWs and the electronic structure in the entire length of the nanowire. Silicon atoms ordering and suboxides presence together with formed SiNWs density play an important role in the electronic structure and composition of silicon nanowires arrays. The engineering of the atomic and electronic structure of nanostructured silicon is a main factor for the exploiting SiNW arrays as universal matrices for different application fields and can be precisely determined by XANES spectroscopy.

In general, the presence of SiO_2 and SiO_x on the sidewalls of SiNWs prepared by the MAWCE approach are confirmed. The composition and electronic structure of n-type lowly

and highly doped SiNWs are different. For highly doped SiNWs, the surface is dominated by SiO_2 and SiO_x in-depth 120 nm. For lowly doped SiNWs, the surface is dominated by c-Si in-depth 120 nm. The results indicate that the silicon suboxides (SiO_x) can be formed on the surface of SiNWs in the etching process or exposed in the air.

3.7.5 Surface investigation of SiNWs with and without native AgNPs during hydrogen generation

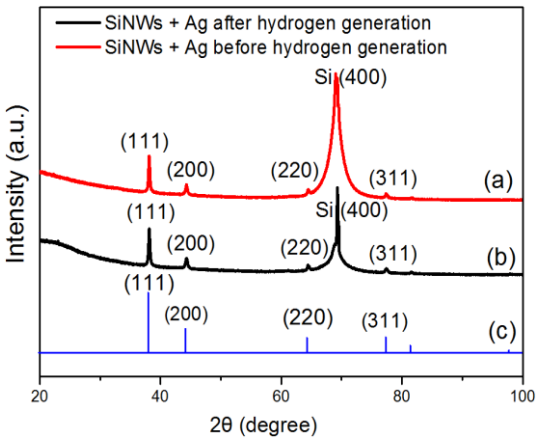

Figure 3.27 XRD of SiNWs with native AgNPs (a) after and (b) before hydrogen generation. (c): Reference pattern of Ag (JCPDS Card No. 00-004-0783).

As shown in Figure 3.16 and 3.17, SiNWs with native AgNPs (without 65% HNO_3 treatment) exhibit excellent hydrogen generation and totally different morphology in comparison to SiNWs without AgNPs after hydrogen evolution. Usually, the native AgNPs are removed by HNO_3 to get clean SiNWs. To the best of our knowledge, no literature has reported SiNWs with native AgNPs for hydrogen generation. For these reasons, it is necessary to clarify the mechanism of hydrogen generation on SiNWs with native AgNPs.

XRD is employed to investigate the influence of native AgNPs during the hydrogen evolution. Figure 3.27 shows the XRD results of two identical pieces of SiNWs with native AgNPs before and after hydrogen evolution. It is clear to see that the diffraction patterns of the AgNPs are identical. The mean size of AgNPs before and after hydrogen evolution is estimated by the Scherrer equation as 40 nm. The results indicate AgNPs are not changed during the hydrogen generation. Due to native AgNPs stay at the bottom of SiNWs and photocatalysis occurs on the sidewalls of SiNWs, therefore, AgNPs are not associated with the more hydrogen generation.

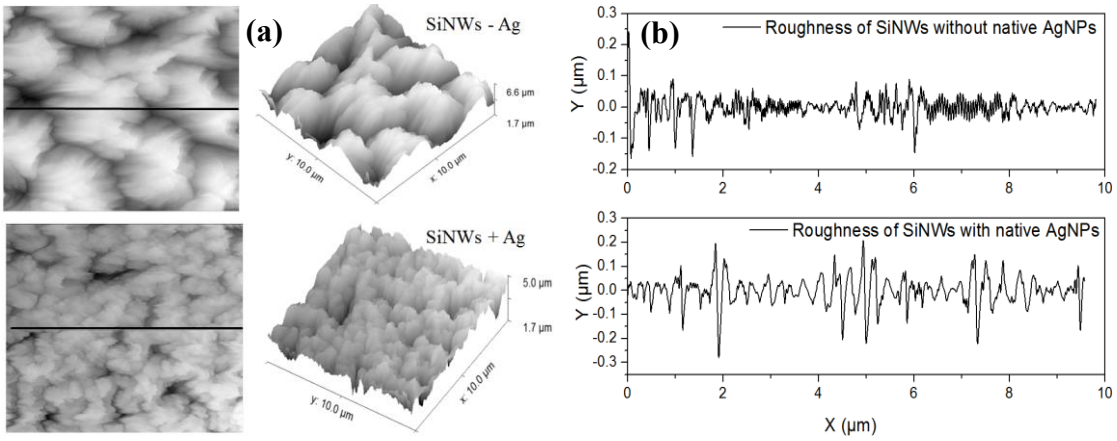

Figure 3.28 SiNWs with and without native AgNPs measured by AFM: (a) Top view and 3D images; (b) the roughness of SiNWs wafer surface.

As TEM images show (*fig. 3.9* c and d), SiNWs with native AgNPs have a rougher surface than without native AgNPs. To confirm the rougher surface, AFM and BET were employed to quantify the surface roughness. AFM results are shown in Figure 3.28. Figure 3.28 (a) shows that the density of SiNWs with native AgNPs clusters is higher than SiNWs without native AgNPs clusters. It should mention that AFM can only quantify the roughness of the SiNWs wafer surface (top of SiNWs) because the scanning tip cannot scan the sidewall of SiNWs. The average roughness of SiNWs with and without native wafer surface is calculated by AFM as 41.45 nm and 23.85 nm (*fig. 3.28* b), respectively. To quantify the sidewall, BET was employed to measure the surface area of SiNWs powder. The surface area of SiNWs with and without native AgNPs powder is calculated by BET as 54.1 m^2/g and 43.1 m^2/g, respectively. Both AFM and BET results indicate the basic distinction of the surface between SiNWs with and without native AgNPs. SiNWs with native AgNPs have about 74% higher average roughness on the wafer surface and about 26% higher surface area than the SiNWs without native AgNPs. As discussed in chapter **3.63**, oxidation of SiNWs contributes the most hydrogen generation, therefore, the rougher surface (or higher surface area) is the main reason that SiNWs with native AgNPs produce more hydrogen than without AgNPs. It also can explain the results in Figure 3.16 (a) and (d). Because of the rougher surface (or higher surface area) of SiNWs with native AgNPs, the surface is quickly oxidized in water. Therefore, the amount of hydrogen produced in 5 min in darkness is almost the same as in white light. Due to the less rough surface of SiNWs without native AgNPs, the effect of photocatalysis is obvious in 5 min.

However, comparing the SEM images of SiNWs with and without native AgNPs after hydrogen evolution in Figure 3.17 (a) and (d), SiNWs without native AgNPs become silica powder but SiNWs with native AgNPs form "SiNWs film". The nanostructure of SiNWs with native AgNPs after hydrogen evolution is almost the same as before hydrogen evolution. To clarify the different morphologies after hydrogen generation, infrared spectroscopy and UV-vis spectroscopy are performed to investigate the surface chemical composition and optical properties of SiNWs with and without native AgNPs during hydrogen evolution.

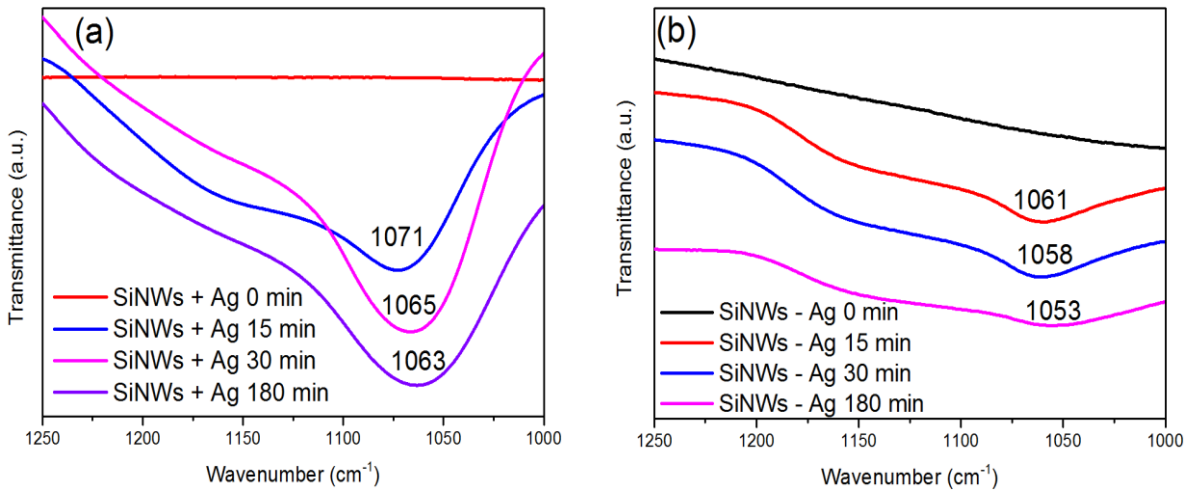

Figure 3.29 FTIR transmission spectra of SiNWs (a) with and (b) without native AgNPs at different times (0 min, 15 min, 30 min, 180 min) in the range of 1000-1250 cm^{-1}.

Infrared absorption (IR) spectroscopy is a powerful tool for providing information on the chemical structure and the densities of Si-O bonds. 1000-1100 cm^{-1} is a typical Si-O stretching mode. [174] This peak is neither observed from SiNWs with native AgNPs nor without native AgNPs before placed in water (0 min). However, it is clearly visible after SiNWs are put in water for 15 min. For SiNWs with native AgNPs, the Si-O bond shows up at 1071 cm^{-1} within 15 min, then shifts to 1063 cm^{-1} at 180 min (*fig. 3.29* a). For SiNWs without AgNPs, Si-O bond is observed at 1061 cm^{-1} at 15 min, then shifts to 1053 cm^{-1} at 180 min (*fig. 3.29* b). In general, the position of Si-O bond shifts to lower wavenumbers during hydrogen generation (dependence in time). However, the wavenumber of the Si-O bond of SiNWs with native AgNPs is greater than without native AgNPs at the same time. Lisovskii et. al reported that the dominant structural component is $SiO_{1.3\text{-}1.5}$ complex in the position 1061-1071 cm^{-1} and $SiO_{1.7\text{-}2}$ is in the position 1050-1058 cm^{-1}. [175] Therefore, SiNWs with native AgNWs form a dominant $SiO_{1.5}$ layer, while SiNWs without native SiNWs become SiO_2 from $SiO_{1.5}$. The reason could be the different roughness of the surface of SiNWs.

SiNWs with native AgNPs are oxidized by water and quickly form a thicker $SiO_{1.5}$ layer. Due to $SiO_{1.5}$ has strong stability in water, [176] it covers the SiNWs and prohibits H_2O molecules from percolating and further oxidizing SiNWs. [177] However, for the SiNWs without native AgNPs, H_2O molecules could percolate the thin $SiO_{1.5}$ layer and fully oxidized the SiNWs. When the $SiO_{1.5}$ layer is not thick enough to protect SiNWs from being oxidized, SiNWs will be continuously oxidized. Finally, the nanostructure of SiNWs without native SiNWs is completely destroyed and SiNWs with native AgNWs keeps the initial nanostructure. Due to SiNWs without native Ag that are completely oxidized and formed SiO_2, hydrogen can not be generated after 30 min (Figure 3.16 a). However, SiNWs with native AgNPs still can produce hydrogen until 120 min due to slow oxidation (Figure 3.16 d). Figure 3.29 also shows the peak intensity of SiNWs with native AgNPs (*fig. 3.29* a) is stronger than SiNWs without native AgNPs (*fig. 3.29* b). S. Miyazaki et al.reported the infrared peak of Si-O bond decreased with decreasing oxide thickness, [178] which is in agreement with our results. Due to the rougher surface of SiNWs with native AgNPs, the oxide layer is thicker. Therefore, the peak intensity in Figure 3.29 (a) is stronger than in Figure 3.29 (b). Also, the intensity in Figure 3.29 (a) increases with time denotes that the thickness of the oxide layer grows with time. However, the intensity of the peak at 180 min in Figure 3.29 (b) is weaker than at 15 min and 30 min, it could be the nanostructure of SiNWs is destroyed at 180 min, and only a little of the silica powder is on the silicon substrate.

UV-vis spectroscopy was used to investigate the absorption changes of SiNWs with and without native AgNPs during the hydrogen evolution. For SiNWs with native AgNPs, two remarkable peaks were observed at around 400 nm and 310 nm (*fig.*3.30 a). The peak around 400 nm could be attributed to the surface plasmon resonance (SPR) of AgNPs. [179] The most interesting peak is around 310 nm which as was observed has a blue shift during the hydrogen generation (dependence in time). This peak shows up at 15 min at 324 nm, then it shifts to 304 nm after 180 min of hydrogen generation (*fig.* 3.30 c). These peaks can be correlated with the presence of silicon suboxides SiO_x ($0<X<2$), where the x value is depending on the hydrogen generation detachment time.[180] The observed peak blue shift indicates that the SiO_x is unstable in water. Shabalov et. al reported the bandgap of SiO_x is increasing with x value increasing. [181] According to the literature, silicon suboxide with x values about 1.3 has a bandgap about 3.8eV and has similar properties as a wide-bandgap semiconductor, for example like titanium dioxide. At x values about 1.7 the bandgap shifts to the higher energies, over 4.1eV. The presence of silicon suboxides (with x values about 1.3

and wide-bandgap semiconductor character of the surface) can be a possible explanation of the observed high hydrogen generation rates and also decrease of hydrogen generation rate after 2 hours. However, silicon suboxides related absorption bands were not found for the SiNWs without AgNPs (*fig.* 3.30 b). An absorption peak at about 360 nm is seen from SiNWs without native AgNPs. This peak could be the characteristic peaks of SiNWs in water. [182]

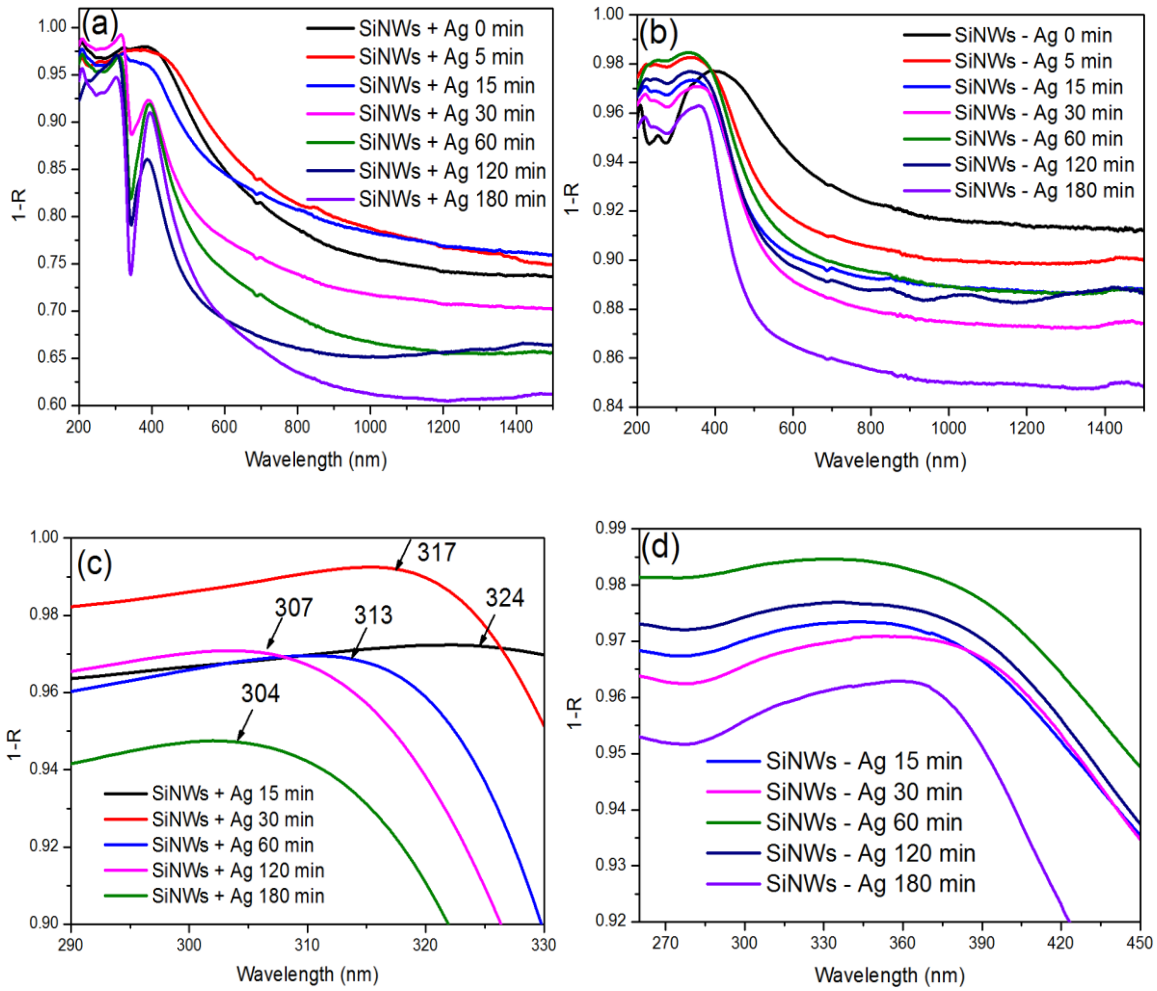

Figure 3.30 1-R spectra of SiNWs (a) with and (b) without native AgNPs at different times (5 min, 15 min, 30 min, 60 min, 120 min, 180 min) in the range of 200-1500 nm; (c) is 1-R spectra of SiNWs with native AgNPs at different times (15 min, 30 min, 60 min, 120 min, 180 min) in the range of 290-330 nm; (d) 1-R spectra of SiNWs without native AgNPs at different times (15 min, 30 min, 60 min, 120 min, 180 min) in the range of 260-450 nm;

In general, SiNWs with native AgNPs have the rougher surface than SiNWs without native AgNPs. The rougher surface is oxidized by water and forms a dominant $SiO_{1.5}$ oxide layer. The thick oxide layer permits H_2O molecules to percolate and further oxidize SiNWs. In

contact, SiNWs without AgNPs form thin $SiO_{1.5}$ oxide layer, H_2O molecules can percolate this thin oxide layer and fully oxidize SiNWs. Finally, the nanostructure of SiNWs with native AgNWs is saved and form SiO_X/SiNWs film while the nanostructure is destroyed and becomes SiO_2 powder in the water.

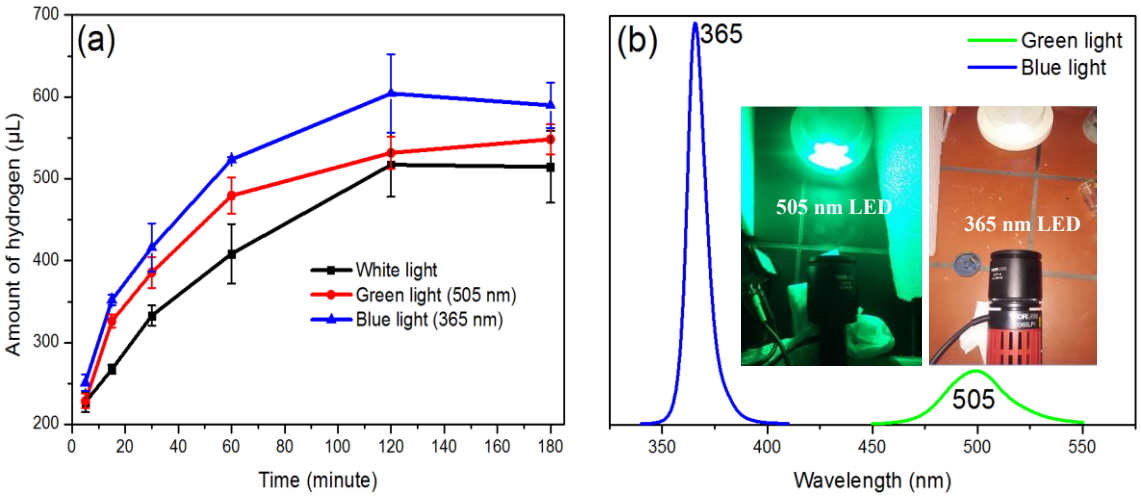

Figure 3.31 (a): Generated hydrogen amount of SiNWs dependence on the reaction time (5, 15, 30, 60, 120, 180 min) in a water/ethanol solution (4:1; v/v) under white light, green light (505 nm) and blue light (365 nm) irradiation; (b): Spectrum of green and blue light. inset: images of the green and blue LED. Each point was measured 4-5 times.

Due to SiNWs with native AgNPs have strong absorption at ultraviolet zone, green light LED (505 nm, THORLABS, M505L3, 42.5 mW/cm^2), blue light LED (365 nm, THORLABS, M365LP1, 33.75 mW/cm^2) and neutral white light LED (33 mW/cm^2, ChiliTec GmbH, 4200K) are employed to investigate system influence of excitation wavelength on the hydrogen generation. Figure 3.31 shows the hydrogen generation under three different kinds of light. SiNWs with native AgNPs produce the most amount of hydrogen in blue light and the least amount of hydrogen in white light, in 180 min. Comparing the hydrogen amount in white LED, it increases by about 10 % in green LED and 20 % in blue LED. The more hydrogen generation could be attributed to the SiO_x. Although SiNWs with native AgNPs have strong absorption at around 400 nm, however, the spectrum shows that 400 nm is not in the region of the white (*fig. 3.14* c), green and blue LED spectrum (*fig. 3.31* b). Therefore, the most probable reason is SiO_x is formed during hydrogen generation. SiO_x film participates in hydrogen generation as photocatalyst. However, due to the bandgap of SiO_x, which increases with time, SiO_x cannot absorb ultraviolet when the energy of ultraviolet is smaller than the bandgap energy. Finally, the hydrogen generation is terminated.

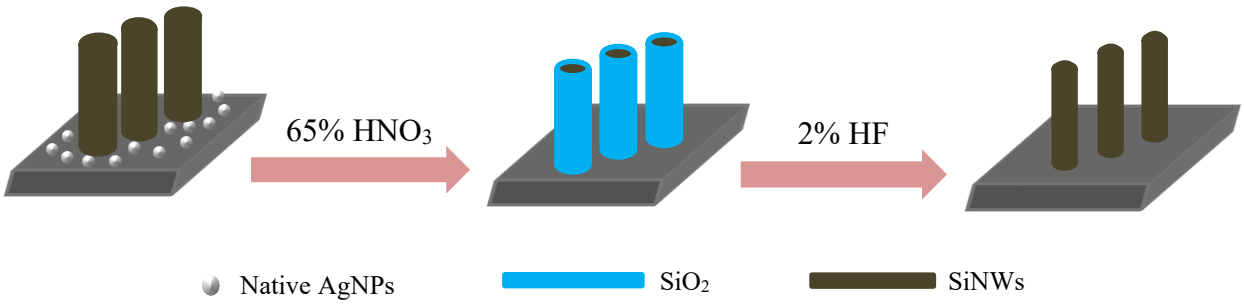

Figure 3.32 Schematic model from SiNWs with native AgNPs to SiNWs without native AgNPs.

The essential difference of SiNWs with and without AgNPs is HNO_3 treatment. Figure 3.32 shows the process from SiNWs with native AgNPs to SiNWs without native AgNPs. When native AgNPs are removed by 65% HNO_3, the rougher surface of SiNWs is oxidized to be SiO_2 by 65% HNO_3, simultaneously. The TEM images (*fig. 3.9* c and d), AFM and BET results have confirmed the rougher surface of SiNWs with native AgNPs. To investigate the effect of HNO_3 treatment time on hydrogen generation, SiNWs with native Ag are immersed in HNO_3 for different amounts of time (1 min, 5 min, 10 min, 20 min). As Figure 3.33 shows, the hydrogen amount is almost the same. It indicates that the thickness of the SiO_2 layer is independent of oxidation time in HNO_3. It may be the SiO_2 layer prohibits the HNO_3 from oxidizing deeper once it is formed. Therefore, the HNO_3 treatment time hardly affects hydrogen generation.

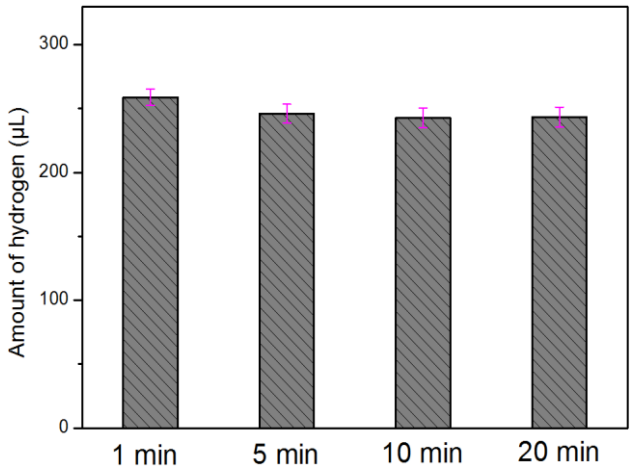

Figure 3.33 Hydrogen amount of SiNWs with native AgNPs immersed in 65% HNO_3 for different time (1 min, 5 min, 10 min, 20 min) in a water/ethanol solution (4:1; v/v) in white light for 3h.

4. Conclusions

Hydrogen generation of SiNWs in water-based solution was systematically investigated in the frame of presented Ph.D. thesis. It contains the evaluation of hydrogen generation depending on the pre-nature of silicon wafer: (I) different silicon conductivity types (n- and p-type) and doping level (highly and lowly doped) of SiNWs; (II) SiNWs decoration with AgNPs at the top, in middle and at the bottom, realized by applying three silver deposition methods: electroless silver deposition (ELD), silver mirror reaction (MR) and native AgNPs. The atomic, electronic structure and composition of SiNWs and the surface change during the hydrogen generation have been studied in detail. The influencing factors of hydrogen generation such as SiNWs surface and hole scavagers have also been investigated. Moreover, this thesis aimed at revealing the mechanism of hydrogen generation based on SiNWs. The following results have been achieved:

1. Comparing the hydrogen generation using different types (n and p-type) and doping level (lowly and highly doped) of SiNWs, the results show that n-type SiNWs produce about three times hydrogen amount than p-type SiNWs in the identical conditions (*fig. 3.13*). It could be the reason that n-type silicon contains lots of negative electrons that are in favor of catching the Ag^+ and results in lateral etching during the etching process. In contrast, excess holes are in the p-type silicon wafer and the lateral etching is weak. Therefore, n-type SiNWs is more porous and rougher than p-type SiNWs. Also, n-type silicon as an electron donor can enhance the hydrogen generation in comparison to the electron acceptor p-type silicon. Furthermore, n-type highly doped SiNWs produce about 2.5 times hydrogen amount as n-type lowly doped SiNWs (*fig. 3.13*), it is because of n-type highly doped silicon has much more dopants than the lowly doped silicon substrate. The dopants catch Ag^+ and form new nucleus. Therefore, n-type highly doped SiNWs are more porous and rougher than n-type lowly doped SiNWs.

2. SiNWs decorated with native AgNPs generate significantly higher hydrogen amount in comparison to other silver decorated systems realized by electroless silver deposition (ELD), silver mirror reaction (MR) methods (*fig. 3.15*). SiNWs with native AgNPs produce the most amount of hydrogen and the SiNWs decorate with AgNPs by MR produce the least amount of hydrogen. Moreover, the hydrogen generation rate

of SiNWs decorated with AgNPs realized by the MR method is highest in comparison to the ELD formed AgNPs, in which the hydrogen generation rate was observed as lowest (*fig. 3.16*). The main explanation for this effect is that SiNWs surface decorated with native AgNPs (without HNO_3 treatment) is rougher than SiNWs (with HNO_3 treatment), the rougher surface can produce significantly higher hydrogen amount. Because more SiNWs are consumed during the decoration by MR method, SiNWs decorated AgNPs (MR) produce the least hydrogen (*fig. 3.18*). AgNPs staying in the middle (by MR) promotes the separation of photo-generated electrons and holes in the photocatalysis process and inhibits SiNWs to be oxidized. Therefore, the hydrogen generation rate is highest. The AgNPs decorated SiNWs at the top by LED method suppress the light absorption, hence, the hydrogen generation increases the least. These results indicate the hydrogen generation amount strongly depends on the rough surface of SiNWs. Rougher surfaces can produce more hydrogen. The decoration of the AgNPs also affects the hydrogen generation amount. Avoiding the losing of SiNWs during the decoration and AgNPs on the sidewalls of SiNWs is important to enhance the hydrogen generation amount and rate. Also, the surface of native AgNPs decorated surface is covered by silicon suboxide (SiO_x) which has a wide-bandgap semiconductor character similar to the widely used titanium oxide (TiO_2).

3. Hydrogen generation strongly depends on the surface area of SiNWs (active surface) (*fig. 3.23*). Because the individual possible pathways to generate hydrogen (the oxidation, photocatalysis, and cleavage of Si-H bonds) are strongly affected by SiNWs area.

4. Ethanol, i-PrOH, acetone can be applied as effective hole scavager molecules to enhance the hydrogen generation compared to pure water. The generated hydrogen amounts produced during the implementation of different hole scavager molecules show that no obvious difference among ethanol, i-PrOH, acetone-water solution was observed (*fig. 3.12*).

5. UV-vis spectroscopy and infrared spectroscopy have been employed to investigate the SiNWs surface with and without native AgNPs changes during the hydrogen generation. The observed results show that silicon suboxides (SiO_x) with wide-bandgap semiconductor characteristics are formed during the hydrogen generation in

the water-ethanol environment. The X values and the bandgap of SiO_x become larger with time. The Ultrasoft X-ray Emission Spectroscopy (USXES) and X-ray Absorption Near-Edge Structure (XANES) results also demonstrate the presence of SiO_x on the surface of SiNWs without AgNPs as a main phase in the initial highly doped n-type SiNWs (*table 1*). SiNWs with native AgNPs forms dominated SiO_x (x=1.3-1.5) phase in comparison SiNWs without AgNPs fast forms SiO_x (x=1.7-2.0) after hydrogen evolution (*fig. 3.29*). Moreover, SiNWs with native AgNPs become SiO_x film after hydrogen evolution, but the nanostructure of SiNWs without native AgNPs is destroyed completely. SiNWs with native AgNPs is the best system for efficient hydrogen generation (*fig. 3.17*).

6. Optical excitation wavelength hardly influences hydrogen generation of SiNWs without AgNPs (*fig. 3.14*), but strongly influences the SiNWs with native AgNPs to produce hydrogen (*fig. 3.31*). It is because SiNWs without AgNPs quickly form SiO_2 and the nanostructure is destroyed, however, SiNWs with native AgNPs slowly form a dominated $SiO_{1.5}$ phase, and the nanostructure is protected from oxidation. The $SiNWs/SiO_x$ film has a strong ultraviolet absorption at about 320 nm. The photocatalytic nature of hydrogen generation was also confirmed experimentally where the highest amount of hydrogen in the native AgNPs decorated SiNWs under the UV light irradiation was observed.

7. There are three main ways to produce hydrogen using SiNWs array in water-based solutions. The first one is related to the direct oxidation of SiNWs in water during which hydrogen as a byproduct can be generated. The second way is direct photocatalysis. The presence of the silicon suboxides as the main phase in highly doped n-type SiNWs was experimentally verified using UV-vis, IR and X-Ray spectroscopy methods. The observed SiO_x can play as an efficient photocatalyst to produce hydrogen. The third way for hydrogen generation in the applied system is desorption of hydrogen from the SiNWs surface or formation of hydrogen due to the damage of -H terminated silicon nanowires surface (*fig. 3.20*). The most realistic explanation of hydrogen generation using n-type highly doped silicon nanostructures with native AgNPs is a combination of surface oxidation and photocatalysis that is the main scientific goal of presented Ph.D. thesis and based on broad experimental data.

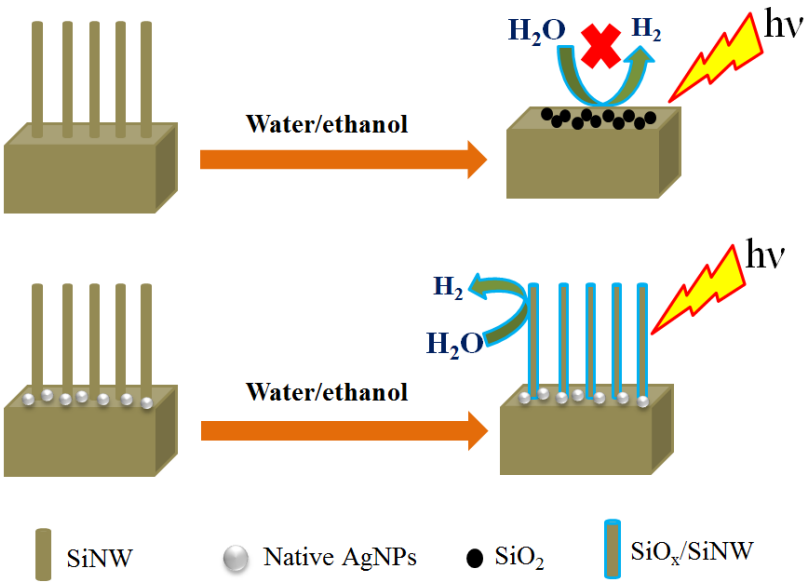

Figure 4.1 Schematic representation of SiNWs with and without native AgNPs in water.

It is the first time to observe excellent hydrogen generation and strong stability of n-type highly doped SiNWs with native AgNPs in water. The thick SiO_x (x=1.3-1.5) coverage not only protects SiNWs from oxidation but also plays as photocatalysts to generated hydrogen (*fig.* 4.1). Ultrasoft X-ray Emission Spectroscopy (USXES) and X-ray Absorption Near-Edge Structure (XANES) demonstrate the presence of SiO_x on the surface of SiNWs without AgNPs as the main phase in the initial n-type highly doped SiNWs (*Table* 1). However, due to the less rough surface, SiNWs without AgNPs quickly become SiO_2 powder in water and cannot produce hydrogen after 30 min (*fig.* 3.13) while SiNWs with native AgNPs can continuously produce hydrogen. This investigation provides the possible way to effectively and sustainably produce hydrogen by SiNWs in water.

5. Zusammenfassung

Die Wasserstofferzeugung von SiNWs in wässriger Lösung wurde im Rahmen der vorliegenden Doktorarbeit systematisch untersucht. Sie enthält die Bewertung der Wasserstofferzeugung in Abhängigkeit von der Vornatur des Siliziumwafers: (I) verschiedene Siliziumleitfähigkeitstypen (n-und p-Typ) und Dotierungsgrad (hoch-und niedrigdotiert) von SiNWs; (II) SiNWs-Dekoration mit AgNPs oben, in der Mitte und unten, realisiert durch die Anwendung von drei Silberabscheidungsmethoden: stromlose Silberabscheidung (ELD), Silberspiegelreaktion (MR) und native AgNPs. Die atomare, elektronische Struktur und Zusammensetzung von SiNWs und die Oberflächenveränderung während der Wasserstofferzeugung wurden im Detail untersucht. Auch die Einflussfaktoren der Wasserstofferzeugung wie SiNWs Oberflächen- und Lochfänger wurden untersucht. Darüber hinaus hat diese Arbeit versucht, den Mechanismus der Wasserstofferzeugung auf der Grundlage von SiNWs. Die folgenden Ergebnisse wurden erzielt:

1. Vergleicht man die Wasserstofferzeugung der SiNWs mit verschiedenen Dotiertypen (n- und p-Typ) und dem Dotierungsgrad (niedrig- und hochdotiert), so zeigen die Ergebnisse, dass n-SiNWs unter identischen Bedingungen etwa die drei-fache Wasserstoffmenge produzieren im Vergleich zu p-SiNWs (*abb. 3.13*). Ein Möglicher Grund dafür könnte sein, dass n-Typ Silizium viele negative Elektronen enthält, die für den Fang des Ag+ sprechen und zu seitlichem Ätzen während des Ätzprozesses führen. Im Gegensatz dazu befinden sich überschüssige Löcher im p-Typ Silizium-Wafer und das seitliche Ätzen ist schwächer ausgeprägt. Daher sind n-Typ SiNWs poröser und rauer als p-Typ SiNWs. Auch n-Typ Silizium als Elektronendonor kann die Wasserstofferzeugung im Vergleich zum p-Typ Silizium als Elektronenakzeptors verbessern. Darüber hinaus produzieren n- hochdotierte SiNWs etwa die 2,5-fache Wasserstoffmenge als n- niedrigdotierte SiNWs (*abb. 3.13*), da n- hochdotiertes Silizium viel mehr Dotierstoffe aufweist als das niedrigdotierte Siliziumsubstrat. Die Dotierstoffe fangen Ag+ und bilden einen neuen Keim. Daher ist n- hochdotiertes SiNWs poröser und rauer als n- niedrigdotiertes SiNWs.

2. SiNWs, die mit nativen AgNPs dekoriert sind, erzeugen deutlich höhere Wasserstoffmengen im Vergleich zu anderen silberbeschichteten Systemen, die durch stromlose Silberabscheidung (ELD) und Silberspiegelreaktion (MR) realisiertwurden

(*abb. 3.15*). SiNWs mit nativen AgNPs produzieren die größte Menge an Wasserstoff. SiNWs dekoriert mit AgNPs von MR produzieren die geringste Menge an Wasserstoff. Darüber hinaus ist die Wasserstofferzeugungsrate von SiNWs, die mit AgNPs dekoriert sind, die nach dem MR-Verfahren realisiert wurden, höher im Vergleich zu den ELD-geformten AgNPs, bei denen die Wasserstofferzeugungsrate die niedrigste ist (*abb. 3.16*). Die Ursache für diesen Effekt ist, dass die mit nativen AgNPs dekorierte SiNWs-Oberfläche (ohne HNO_3-Behandlung) rauer ist als die SiNWs (mit HNO_3-Behandlung), die rauere Oberfläche kann eine deutlich höhere Wasserstoffmenge erzeugen. Da bei der Dekoration nach dem MR-Verfahren mehr SiNWs verbraucht werden, produzieren SiNWs dekorierte AgNPs (MR) am wenigsten Wasserstoff (*abb. 3.18*). AgNPs, die in der Mitte bleiben (durch MR), fördern die Trennung von photogenerierten Elektronen und Löchern im Photokatalyseprozess und verhindern, dass SiNWs oxidiert werden. Daher ist die Wasserstofferzeugungsrate am höchsten. Die oben mit AgNPs dekorierten SiNWs im LED-Verfahren unterdrücken die Lichtabsorption, so dass die Wasserstofferzeugung am geringsten ist. Diese Ergebnisse deuten darauf hin, dass die Menge der Wasserstofferzeugung stark von der rauen Oberfläche der SiNWs abhängt. Eine rauere Oberfläche kann mehr Wasserstoff produzieren. Die Art der Dekoration mit AgNPs beeinflusst auch die Menge der Wasserstofferzeugung. Die Vermeidung des Verlusts von SiNWs während der Dekoration mit AgNPs an den Seitenwänden von SiNWs sind wichtig, um die Menge und Geschwindigkeit der Wasserstofferzeugung zu erhöhen. Außerdem ist die Oberfläche der mit nativen AgNPs dekorierten SiNWs mit unterstöchiometrischem Siliziumoxid (SiO_x) bedeckt, das einen breitbandigen Halbleitercharakter hat, der dem weit verbreiteten Titanoxid (TiO_2) ähnlich ist.

3. Die Wasserstofferzeugung hängt stark von der größe der Oberfläche der SiNWs (aktive Oberfläche) ab (*abb. 3.23*). Denn die einzelnen möglichen Wege zur Wasserstofferzeugung (Oxidation, Photokatalyse und Spaltung von Si-H-Bindungen) werden vom SiNWs-Bereich stark beeinflusst.

4. Ethanol, i-PrOH, Aceton können als effektive Elektronendonor eingesetzt werden, um die Wasserstofferzeugung im Vergleich zu reinem Wasser zu verbessern. Die erzeugten Wasserstoffmengen, die bei der Implementierung verschiedener

Lochfangmoleküle entstehen, zeigen, dass kein offensichtlicher Unterschied zwischen Ethanol, i-PrOH, Aceton-Wasser-Lösung beobachtet wurde (*abb. 3.12*).

5. UV-Vis-Spektroskopie und Infrarotspektroskopie wurden eingesetzt, um Veränderungen der SiNWs-Oberfläche mit und ohne native AgNPs während der Wasserstofferzeugung zu untersuchen. Die Ergebnisse zeigen, dass Siliziumsuboxide (SiOx) mit breitbandigen Halbleitereigenschaften bei der Wasserstofferzeugung in der Wasser-Ethanol-Umgebung entsteht. Die Suboxidkonzentration ? und die Bandlücke von SiO_x werden mit der Zeit größer. Die Ergebnisse der Ultrasoft-Röntgen-Emissionsspektroskopie (USXES) und der X-ray Absorption Near-Edge Structure (XANES) zeigen auch das Vorhandensein von SiO_x auf der Oberfläche von SiNWs als Hauptphase in den hochdotierten n-Typ-SiNWs (*tablle 1*). SiNWs mit nativen AgNPs- dominiert die SiO_x (x=1,3-1,5) Phase im Vergleich zu SiNWs ohne AgNPs bildet schnell SiO_x (x=1,7-2,0) nach der Wasserstoffentwicklung (*abb. 3.29*). Darüber hinaus werden SiNWs mit nativen AgNPs nach der Wasserstoffentwicklung zum SiOx-Film, aber die Nanostruktur von SiNWs ohne native AgNPs werden vollständig zerstört. SiNWs mit nativen AgNPs stellte sich als das effizienteste Syste zur Wasserstofferzeugung heraus (*abb. 3.17*).

6. Die optische Anregungswellenlänge beeinflusst die Wasserstofferzeugung von SiNWs ohne AgNPs kaum. (*abb. 3.14*), sondern beeinflusst die SiNWs mit nativen AgNPs zur Wasserstofferzeugung stark (*abb. 3.31*). Weil SiNWs ohne AgNPs schnell SiO_2 bilden und die Nanostruktur zerstört wird, SiNWs mit nativen AgNPs jedoch langsam eine dominierte $SiO_{1.5}$-Phase bilden und die Nanostruktur vor Oxidation geschützt ist. Der SiNWs/SiO_x-Film hat eine starke UV-Absorption bei etwa 320 nm. Die photokatalytische Natur der Wasserstofferzeugung wurde auch experimentell bestätigt, wobei die höchste Wasserstoffmenge in den nativen AgNPs, die unter der UV-Lichtbestrahlung mit SiNWs dekoriert wurden, beobachtet wurde.

7. Es gibt drei Mechanismen, Wasserstoff mit Hilfe von SiNWs- in wasserbasierten Lösungen herzustellen. The first one is related to the direct oxidation of SiNWs in water during which hydrogen as a byproduct can be generated. Der zweite Weg ist die direkte Photokatalyse. Das Vorhandensein der Siliziumsuboxide als Hauptphase in hochdotierten n-Typ-SiNWs wurde experimentell mit UV-Vis, IR und Röntgenspektroskopieverfahren nachgewiesen. Das beobachtete SiO_x kann als

effizienter Photokatalysator zur Wasserstofferzeugung eingesetzt werden. Der dritte Weg zur Wasserstofferzeugung im angewandten System ist die Desorption von Wasserstoff aus der SiNWs-Oberfläche oder die Bildung von Wasserstoff aufgrund der Beschädigung der Oberfläche von -H terminierten Silizium-Nanodrähten(*abb. 3.20*). Die realistischste Erklärung für die Wasserstofferzeugung mit n- hochdotierten Silizium-Nanostrukturen mit nativen AgNPs ist eine Kombination aus Oberflächenoxidation und Photokatalyse, welche ein Hauptziel der vorliegenden Doktorarbeit ist und auf breiten experimentellen Daten basiert.

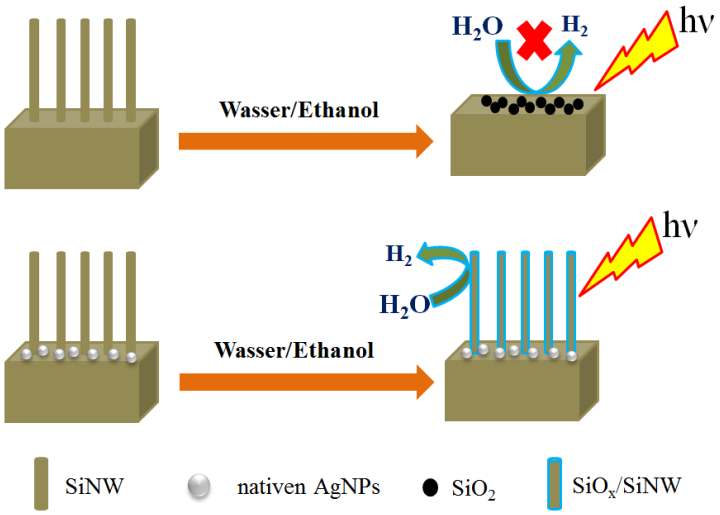

Abbildung 5.1 Schematische Darstellung von SiNWs mit und ohne nativen AgNPs in Wasser.

Zum ersten Mal wurde von n-hochdotierten SiNWs mit nativen AgNPs in Wasser, eine ausgezeichnete Wasserstofferzeugung bei gleichzeitig hoher Stabilität beobachtet. Die dicke SiOx (x=1,3-1,5) Schicht schützt die SiNWs nicht nur vor der Oxidation, sondern spielt auch als Photokatalysator für den erzeugten Wasserstoff (Abb. *5.1*) eine Rolle. Obwohl die Ultrasoft-Röntgen-Emissionsspektroskopie (USXES) und die X-ray Absorption Near-Edge Structure (XANES) das Vorhandensein von SiO_x auf der Oberfläche von SiNWs ohne AgNPs als Hauptphase in den anfänglich n- hochdotierten SiNWs zeigen (*Tabelle* 1). Aufgrund der weniger rauen Oberfläche werden SiNWs ohne AgNPs jedoch schnell zu SiO_2-Pulver in Wasser abgebaut und können nach 30 Minuten keinen Wasserstoff mehr produzieren (Abb. 3.13), während SiNWs mit nativen AgNPs kontinuierlich Wasserstoff produzieren können. Diese Untersuchung bietet den möglichen Weg, Wasserstoff durch SiNWs im Wasser effektiv und nachhaltig zu erzeugen.

6. Outlook

6.1 Oxygen detection

Most researchers are focusing on hydrogen generation based on SiNWs but fully ignore an oxygen generation. However, oxygen measurement is highly important as additional evidence of the photocatalytic water splitting process. A lot of literature defined to the hydrogen generation on SiNWs as “water splitting” is not rigorous because hydrogen can come from other ways (e.g. oxidation). In fact, the real “water splitting” must satisfy the condition that the ratio of photo-generated hydrogen to photo-generated oxygen is 2:1.

Once water splitting on SiNWs in water is proved, aside from application in hydrogen generation, SiNWs also can be used in seawater purification, wastewater purification, etc. For this reason, it is necessary to measure the oxygen generation on SiNWs in water. Furthermore, oxygen measurement is useful to reveal the mechanism of SiNWs produce hydrogen in water as photocatalyst. However, it is a huge challenge to measure oxygen due to the oxygen in the air is pervasive and the amount of photo-generated oxygen is very small. It may be the reason that very few literature report oxygen measurements about SiNWs. To the best of my knowledge, only one paper reported the oxygen measurement from SiNWs. [96] In this paper, oxygen was measured by gas chromatography. However, based on communication with the authors and our experience in oxygen measurement, the oxygen results in this paper are still open to question. Moreover, n-type lowly doped SiNWs wafer was employed to produce oxygen in this paper. As discussed above, n-type lowly doped SiNWs is not the best choice because of the much lower hydrogen generation amount in comparison to n-type highly doped SiNWs with native AgNPs.

Here, I introduce two methods for oxygen measurement: one method is gas chromatography, the other method is the oxygen sensor (chapter **2.5**). It is raw data because we have not found appropriate equipment that can detect oxygen precisely. However, these results provide basic guidance to measure oxygen. Based on these results, we propose a method that probably measures oxygen precisely.

It is worth to mention that due to the ethanol can catch the holes and suppress the oxygen generation, therefore, the solvent is pure water. To decrease the surface tension, SiNWs were

not dried after preparation. All samples in this experiment are n-type highly doped SiNWs with native AgNPs.

6.1.1 Oxygen detection by gas chromatography

To make sure the reproducibility of the result, ten empty vials were degassed in the glove box and the ratio of oxygen to nitrogen is measured by gas chromatography. The average ratio of O_2: N_2 in the glove box is 0.005645 (*fig.6.1* a). The standard deviation is about 0.00045. The results indicate the detection of oxygen cannot be controlled precisely. The error mainly occurs in the injection. Ten pieces of SiNWs in pure water in ten vials (each vial hold one piece of SiNWs) were irradiated under white light for 3h. The average ratio of O_2: N_2 is 0.01095 (*fig.6.1* b). The standard deviation is about 0.00096. The average ratio of O_2: N_2 is about two times as that in empty vials. Normally, the ratio of O_2: N_2 should be stable if there is no oxygen generation. The higher ratio of O_2: N_2 for SiNWs in water denotes it could be the oxygen generation.

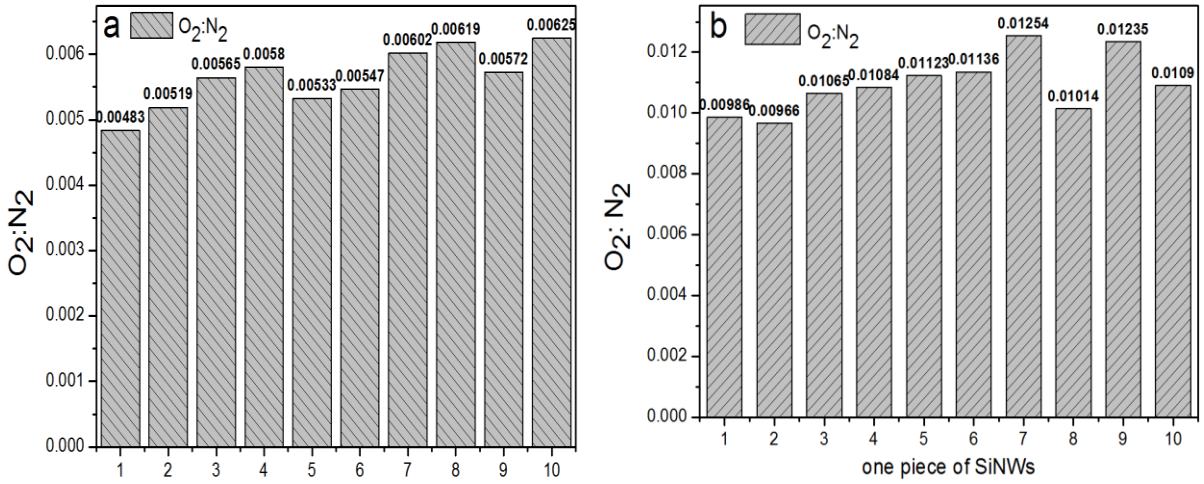

Figure 6.1 The ratios of O_2: N_2 of (a) ten empty vials; (b) ten pieces of SiNWs in ten vials (each vial holds one piece of SiNWs) with 3 mL pure water under white light irradiation for 3h. (The pure water solution was degassed with a freeze-pump-thaw triple cycle under nitrogen and all vials were degassed using glove box under nitrogen atmosphere. 3 mL pure water solution was injected into the vial in the glove box.)

To confirm oxygen generation, the ratios of O_2: N_2 for one piece (1×1 cm^2) of SiNWs were measured at different times (15 min, 30 min, 60 min, 90 min, 120 min). Still, the ratios of O_2: N_2 increased from 0.0066 to 0.01027 with time (*fig.6.2*). The results also indicate the oxygen is generated in the vial.

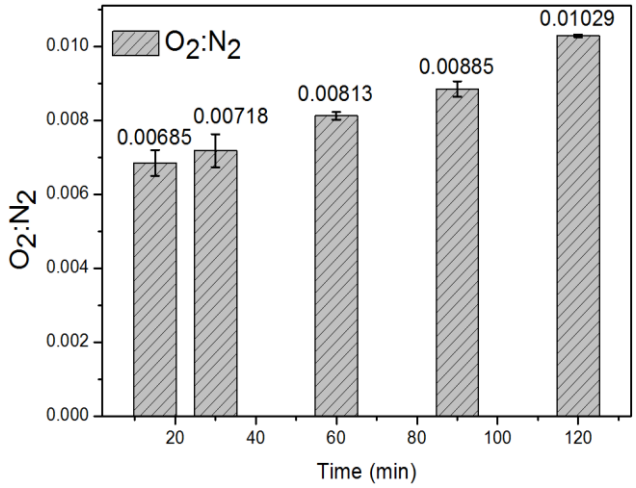

Figure 6.2 The ratios of O_2: N_2 of one piece (1×1 cm^2) of SiNWs in pure water at different times under white light irradiation for 3h. (The pure water solution was degassed with a freeze-pump-thaw triple cycle under nitrogen and all vials were degassed using glove box under nitrogen atmosphere. 3 mL pure water solution was injected into the vial in the glove box.)

Another experiment was also designed to prove oxygen generation. One (1 cm^2), two (2 cm^2) and three pieces (3 cm^2) of SiNWs were fixed in the vials with 3 mL pure water and irradiated under white light for 3h and the ratios of O_2: N_2 were measured by gas chromatography. Figure 6.3 shows that the ratios of O_2: N_2 increased from 0.00987 (1 cm^2) to 0.01372 (3 cm^2).

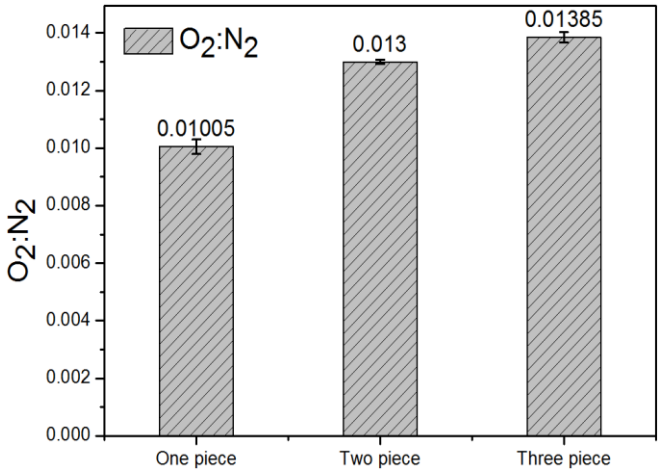

Figure 6.3 The ratio of O_2: N_2 of different pieces of SiNWs in pure water in ten vials under white light irradiation for 3h.

In general, the ratios of O_2: N_2 increases with time and more pieces of SiNWs. Due to the fact that oxygen cannot be generated from the oxidation of SiNWs, it must come from photocatalyst. However, gas chromatography, strictly speaking, cannot precisely measure oxygen because of the effect of oxygen in the air. Moreover, photo-generated oxygen can be dissolved in the water. For these reasons, the oxygen sensor is better to measure oxygen. Oxygen sensor can be immersed in the pure water to measure oxygen. Therefore, it is more precise to measure oxygen. The image of the oxygen sensor is shown in Figure 6.4. The oxygen concentration is recorded by the software on the computer.

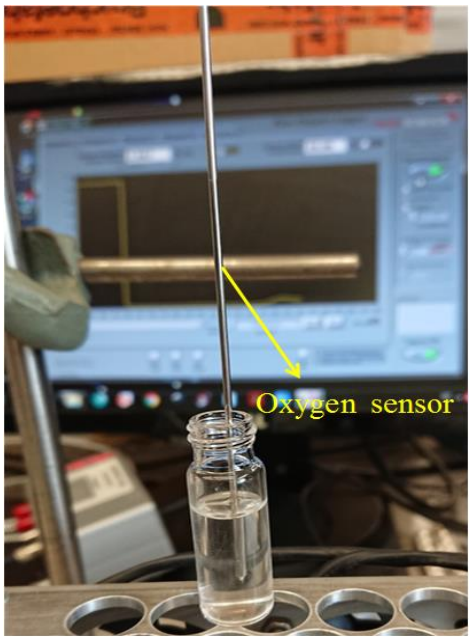

Figure 6.4 Image of oxygen sensor measuring oxygen.

6.1.2 Oxygen detection using dye-sensitive oxygen sensor

The measuring principle of the oxygen sensor is based on the quenching of the red flash indicator luminescence caused by a collision between oxygen molecules and the red flash indicator immobilized on the sensor tip or surface. The duration of the red flash for a single oxygen measurement could be as short as 10 ms. Therefore, the oxygen sensor is very sensitive to the change in oxygen concentration.

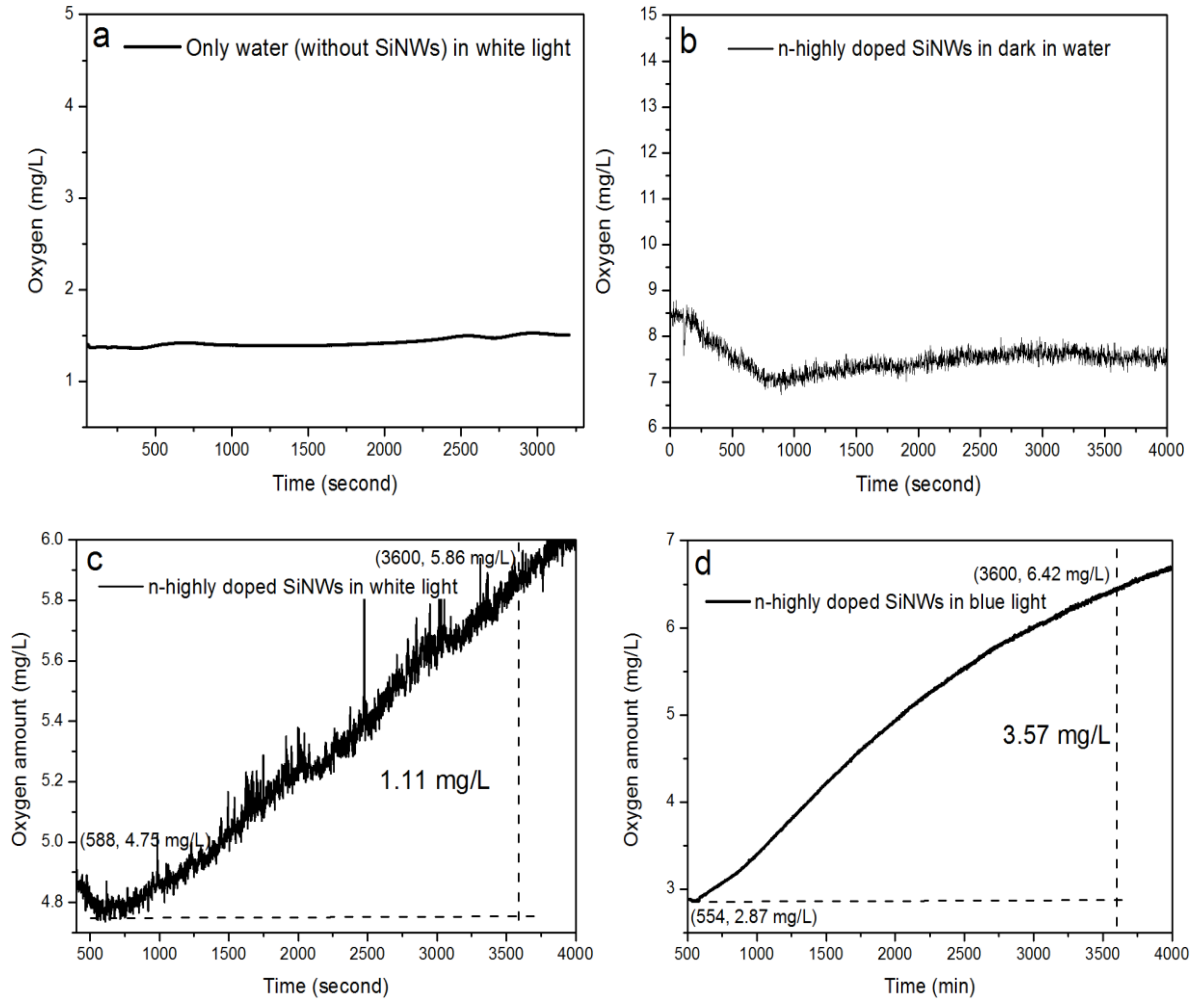

Figure 6.5 Oxygen detection of (a) pure water without SiNWs; (b) SiNWs in pure water in darkness; (c) SiNWs in pure water in white light. (d) SiNWs in water in blue light (365 nm).

The results of oxygen measured by the oxygen sensor are given in Figure 6.5. No oxygen was generated in pure water (*fig. 6.5 a*). SiNWs in darkness also cannot produce oxygen (*fig. 6.5 b*). However, the oxygen amounts were increased to 1.11 mg/L and 3.57 mg/L when SiNWs were in white light and blue light in one hour, respectively (*fig. 6.5 c* and *d*). These results indicate SiNWs can produce oxygen in the light in pure water. However, oxygen concentration at the beginning is very different in Figure 6.5, because the oxygen in the air affected the value of oxygen when the oxygen sensor was immersed in the water from the air. Therefore, the initial oxygen value that the oxygen sensor showed was higher than the real value of oxygen in the water.

6.2 Outlook of oxygen measurement and hydrogen generation

Both gas chromatography and oxygen sensor results indicate that SiNWs could generate oxygen. However, precise oxygen measurement is still a huge challenge due to the strong influence of oxygen in the air. Using pure heavy-oxygen water ($H_2{}^{18}O$) as a solvent is a possible way to exclude the effect of oxygen in the air. The splitting products of $H_2{}^{18}O$ are H_2 and $^{18}O_2$, $^{18}O_2$ can be precisely detected by Mass spectrometry.

However, it is a long story, I have no so much time to finish it during my Ph.D. study. I think it is a good idea to measure the photo-generated oxygen precisely. I wish the person who concentrates on this work can consider this idea and realize it. Once the water splitting is proved by $^{18}O_2$ detection again, SiNWs are not only used in hydrogen generation but also in seawater purification, wastewater purification, etc. These applications are prospective.

SiNWs is a promising material to produce “clean energy” hydrogen in water as photocatalyst. However, the oxidation of SiNWs greatly limits the application. Based on our investigation of hydrogen generation on SiNWs, I propose to prepare shell-core noble metal (e.g. Ag, Au. etc) @ SiNWs with native AgNPs by physical methods as photocatalyst. The shell-core nanostructure can protect SiNWs from suffering oxidation in water, physical methods can avoid the loss of SiNWs during the decoration and noble metal can enhance the hydrogen generating rate. Also, the light source is important. Dut to SiNWs with native AgNPs form stable wide bandgap semiconductor SiO_x in water, using high energy light source to irradiate the sample is necessary.

I hope this thesis can give some guidance and inspiration to people who are doing similar research. I also hope people could consider my suggestions and go further.

Supplement I

The permission of the publisher that I was allowed to use the figures (**Figure 1.7 a, b and c**) in my thesis.

RE: Copyright permission

View Sou
Save

Date: 02/10/19 (22:18:50 CEST)
From: AIPRights Permissions
To: Tingsen Ming

You replied to this message on 03/10/19 16:42:25.

Text (2 KB)

Dear Dr. Ming:

Thank you for requesting permission to reproduce material from AIP Publishing publications.

Material to be reproduced:

Figure 1a from:
Appl. Phys. Lett. 77, 2572 (2000); https://doi.org/10.1063/1.1319191

For use in the following manner:

Reproduced in your PhD thesis.

Permission is granted subject to these conditions:

1. AIP Publishing grants you non-exclusive world rights in all languages and media. This permission extends to all subsequent and future editions of the new work.

2. The following notice must appear with the material (please fill in the citation information):

"Reproduced from [FULL CITATION], with the permission of AIP Publishing."

The notice may appear in the figure caption or in a footnote. In cases where the new publication is licensed under a Creative Commons license, the full notice as stated above must be used.

3. If the material is published in electronic format, we ask that a link be created pointing back to the abstract of the article on the journal website using the article's DOI.

4. This permission does not apply to any materials credited to another source.

For future permission requests, we encourage you to use RightsLink, which is a tool that allows you to obtain permission quickly and easily online. To launch the RightsLink application, simply access the appropriate article on the journal site, click on the "Tools" link in the abstract, and select "Reprints & Permissions."

Please let us know if you have any questions.

Sincerely,
Susann LoFaso
Manager, Rights & Permissions

AIP Publishing
1305 Walt Whitman Road | Suite 300 | Melville NY 11747-4300 | USA

JOHN WILEY AND SONS LICENSE TERMS AND CONDITIONS

Sep 30, 2019

This Agreement between Mr. Tingsen Ming ("You") and John Wiley and Sons ("John Wiley and Sons") consists of your license details and the terms and conditions provided by John Wiley and Sons and Copyright Clearance Center.

License Number	4678750411013
License date	Sep 30, 2019
Licensed Content Publisher	John Wiley and Sons
Licensed Content Publication	Advanced Materials
Licensed Content Title	Boring Deep Cylindrical Nanoholes in Silicon Using Silver Nanoparticles as a Catalyst
Licensed Content Author	K. Tsujino, M. Matsumura
Licensed Content Date	Apr 7, 2005
Licensed Content Volume	17
Licensed Content Issue	8
Licensed Content Pages	3
Type of use	Dissertation/Thesis
Requestor type	University/Academic
Format	Print and electronic
Portion	Figure/table
Number of figures/tables	1
Original Wiley figure/table number(s)	Figure 3d
Will you be translating?	No
Title of your thesis / dissertation	Porous Silicon Nanowires for Hydrogen Generation: Mechanism and Photocatalytic Studies
Expected completion date	Dec 2019
Expected size (number of pages)	120
Requestor Location	Mr. Tingsen Ming Leibniz IPHT Albert Einstein AStr. 9 Jena, 07745 Germany Attn: Mr. Tingsen Ming
Publisher Tax ID	EU826007151
Total	0.00 EUR
Terms and Conditions	

TERMS AND CONDITIONS

This copyrighted material is owned by or exclusively licensed to John Wiley & Sons, Inc. or one of its group companies (each a"Wiley Company") or handled on behalf of a society with which a Wiley Company has exclusive publishing rights in relation to a particular work

Supplement II

The bandgap values of n-type lowly, n-type highly, p-type lowly and p-type highly doped SiNWs were empirically estimated based on the reflectivity measurements and Kubelka-Munk function.

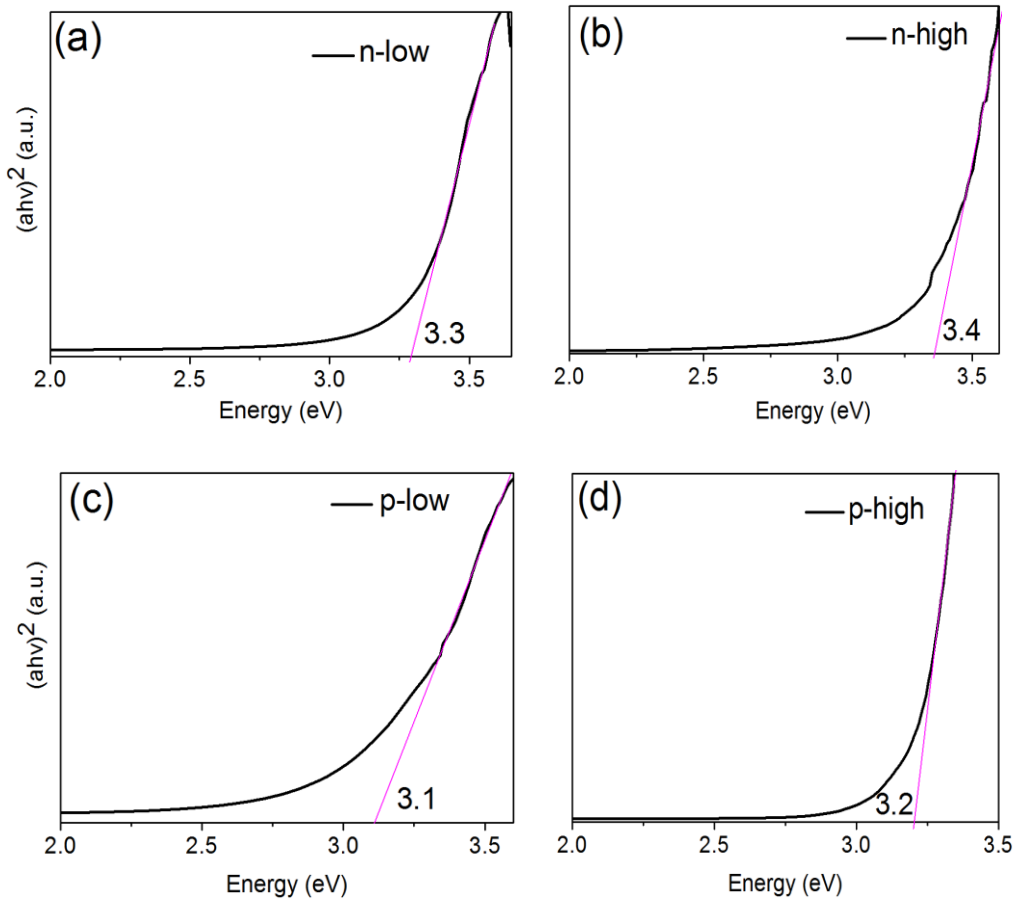

Figure 1 Estimation of band gap in (a): n-type lowly doped SiNWs; (b) n-type highly SiNWs; (c) p-type lowly doped SiNWs; (d) p-type highly doped SiNWs using reflectance spectra (cf. Chapter 3.1) obtained from UV-vis measurements and obtained spectra trasformation using Kubelka-Munk function.

Selbständigkeitserklärung

Ich erkläre, dass ich die vorliegende Arbeit selbständig und unter Verwendung der angegebenen Hilfsmittel, persönlichen Mitteilungen und Quellen angefertigt habe.

Declaration of originality

I certify that the work presented here is, to the best of my knowledge and belief, original and the result of my own investigations, except as acknowledged, and has not been submitted, either in part or whole, for a degree at this or any other university.

Acknowledgment

Here, I want to thank people who have helped me during my Ph.D. study. This thesis would not be possible without their help. I heartfeltly appreciated their patience, often due to my poor English, in their generous assistance in my living and working here in Jena.

Firstly, I would like to thank **Prof. Dr. Benjamin Dietzek** for giving me the opportunity to work in his group. I am grateful that he did not give up on me because of my lack of German skills. I thank him for spending time discussing my topic with me. He has set for me an excellent example of being an outstanding researcher and an inspiring group leader.

I also want to thank **Dr.Vladimir Sivakov**. To be honest, I couldn't get this achievement without his guidance and support. He discussed the experiment results with me and ordered the necessary experiment materials for me. He spent time polishing the paper and report. I thank him so very much. He is a kind and funny man, I am happy to have worked so closely with him. I will remember this time forever.

I would like to thank my colleague **Mr. Alexander Schleusener**. I am thankful for his help when I came to Germany, especially in the first year. He helped me to extend my visa and patiently showed me how to operate the machinery and how to work in the lab. He also helped me to solve some of the problems in life. I am grateful to him.

Thanks a lot to **Dr. Martin Schulz** in our group. He taught me how to measure hydrogen. He has helped me to solve problems during the measurements. He also discussed my topic with me and Vladimir.

I would like to thank **Dr. Erhan Tütüncü** at Ulm University. I'd like to thank him for ordering the oxygen sensor and helping us to measure oxygen.

Many thanks to **Dr. Guobin Jia** for translating the German letters for me and for introducing me to new friends.

I would like to thank all the other colleagues in our group. It is a nice group, people were kind and obliging. They helped me a lot when I had problems.

I thank my family, especially my parents, and friends for understanding me.

Finally, I thank the **China Scholarship Council (CSC)** for their generous financial support.

I thank all the people I mention above, I could not have achieved this without your help. I will remember all of you. My four years in Germany will always be memorable.

Curriculum Vitae

Personal Information

Name	Tingsen Ming
Date of birth	25.12.1982
Nationality	China

University Education and Work Experience

12/2015-present	Doctoral candidate, Group of Prof. Benjamin Dietzek, Leibniz Institute of Photonic Technology (IPHT) and Friedrich Schiller University, Jena, Germany.
07/2013-07/2015	Worked in SGS company in Wuhan city in China.
09/2010-06/2013	Master studies, Group of Prof. Dr. Huogen Yu, Wuhan University of Technology, Wuhan, China (supervised by Prof. Dr. Ping Wang). Topic: Preparation and performance enhancement of graphene-based nano photocatalysts.
08/2007-08/2010	Worked in pharmaceutical company in China.
09/2003-06/2007	Bachelor studies, Department of Chemistry, Inner Mongolia University of Technology, Hohhot, China Thesis: Crystallization Kinetics of Barium Sulfate.

Academic achievements

1. Turishchev, S. Y., Parinova, E. V., Pisliaruk, A. K., Koyuda, D. A., Yermukhamed, D., Ming, T., ... & Sivakov, V. (2019). Surface deep profile synchrotron studies of mechanically modified top-down silicon nanowires array using ultrasoft X-ray absorption near edge structure spectroscopy. *Scientific reports*, *9*(1), 8066.

2. Ming T, Schleusener A, Yermukhamed D, et al. Silver mirror reaction as a simple method for silicon nanowires functionalization. Materials Research Express, **2019**, 6(10): 105057.

References

[1] Kabir E, Kumar P, Kumar S, et al. Solar energy: Potential and future prospects. Renewable and Sustainable Energy Reviews, **2018**, 82: 894-900.

[2] Moniz S J A, Shevlin S A, Martin D J, et al. Visible-light driven heterojunction photocatalysts for water splitting–a critical review. Energy & Environmental Science, **2015**, 8(3): 731-759.

[3] Kibria M G, Chowdhury F A, Zhao S, et al. Visible light-driven efficient overall water splitting using p-type metal-nitride nanowire arrays. Nature communications, **2015**, 6: 6797.

[4] Lewis N S. Research opportunities to advance solar energy utilization. Science, **2016**, 351(6271): aad1920.

[5] Sakthivel S, Neppolian B, Shankar M V, et al. Solar photocatalytic degradation of azo dye: comparison of photocatalytic efficiency of ZnO and TiO_2. Solar energy materials and solar cells, **2003**, 77(1): 65-82.

[6] Shudo T, Suzuki H. Applicability of heat transfer equations to hydrogen combustion. Jsae Review, **2002**, 23(3): 303-308.

[7] Das V, Padmanaban S, Venkitusamy K, et al. Recent advances andchallenges of fuel cell based power system architectures and control–A review. Renewable and Sustainable Energy Reviews, **2017**, 73: 10-18.

[8] Wu D, Long M, Cai W, et al. Low temperature hydrothermal synthesis of N-doped TiO_2 photocatalyst with high visible-light activity. Journal of Alloys and Compounds, **2010**, 502(2): 289-294.

[9] Zou Z, Ye J, Sayama K, et al. Direct splitting of water under visible light irradiation with an oxide semiconductor photocatalyst. nature, **2001**, 414(6864): 625.

[10] Kudo A, Miseki Y. Heterogeneous photocatalyst materials for water splitting. Chemical Society Reviews, **2009**, 38(1): 253-278.

[11] Bolton J R. Solar photoproduction of hydrogen: a review. Solar energy, **1996**, 57(1): 37-50.

[12] Fujishima A, Honda K. Electrochemical photolysis of water at a semiconductor electrode. nature, **1972**, 238(5358): 37.

[13] Shaban Y A, Khan S U M. Visible light active carbon modified n-TiO_2 for efficient hydrogen production by photoelectrochemical splitting of water. International journal of hydrogen energy, **2008**, 33(4): 1118-1126.

[14] Navarro Yerga R M, Alvarez Galvan M C, Del Valle F, et al. Water splitting on semiconductor catalysts under visible-light irradiation. ChemSusChem: Chemistry & Sustainability Energy & Materials, **2009**, 2(6): 471-485.

[15] Mills A, Williams G. Photosensitised oxidation of water by CdS-based suspensions. Journal of the Chemical Society, Faraday Transactions 1: Physical Chemistry in Condensed Phases, **1989**, 85(3): 503-519.

[16] Garg N. A Brief Study on Characteristics, Properties, and Applications of CdSe/Innovation in Materials Science and Engineering. Springer, Singapore, **2019**: 43-60.

[17] Li Z, Xin Y, Wu W, et al. Phosphorus cation doping: A new strategy for boosting photoelectrochemical performance on TiO_2 nanotube photonic crystals. ACS applied materials & interfaces, **2016**, 8(45): 30972-30979.

[18] Neufeld O, Toroker M C. Platinum-doped α-Fe_2O_3 for enhanced water splitting efficiency: a DFT+ U study. The Journal of Physical Chemistry C, **2015**, 119(11): 5836-5847.

[19] Ge M Z, Cao C Y, Li S H, et al. In situ plasmonic Ag nanoparticle anchored TiO_2 nanotube arrays as visible-light-driven photocatalysts for enhanced water splitting. Nanoscale, **2016**, 8(9): 5226-5234.

[20] Salgado S Y A, Zamora R M R, Zanella R, et al. Photocatalytic hydrogen production in a solar pilot plant using a Au/TiO_2 photo catalyst. international journal of hydrogen energy, **2016**, 41(28): 11933-11940.

[21] Chai Z, Zeng T T, Li Q, et al. Efficient visible light-driven splitting of alcohols into hydrogen and corresponding carbonyl compounds over a Ni-modified CdS photocatalyst. Journal of the American Chemical Society, **2016**, 138(32): 10128-10131.

[22] Liu Z, Hou W, Pavaskar P, et al. Plasmon resonant enhancement of photocatalytic water splitting under visible illumination. Nano letters, **2011**, 11(3): 1111-1116.

[23] Klar T, Perner M, Grosse S, et al. Surface-plasmon resonances in single metallic nanoparticles. Physical Review Letters, **1998**, 80(19): 4249.

[24] Maruthamuthu P, Ashokkumar M. Hydrogen production with visible light using metal loaded-WO_3 and MV^{2+} in aqueous medium. International Journal of Hydrogen Energy, **1989**, 14(4): 275-277.

[25] Maruthamuthu P, Ashokkumar M. Hydrogen generation using Cu (II)/WO_3 and oxalic acid by visible light. International journal of hydrogen energy, **1988**, 13(11): 677-680.

[26] Nakibli Y, Mazal Y, Dubi Y, et al. Size Matters: Cocatalyst Size Effect on Charge Transfer and Photocatalytic Activity. Nano letters, **2017**, 18(1): 357-364.

[27] Chen X, Shen S, Guo L, et al. Semiconductor-based photocatalytic hydrogen generation. Chemical reviews, **2010**, 110(11): 6503-6570.

[28] Schneider J, Bahnemann D W. Undesired role of sacrificial reagents in photocatalysis. **2013**.

[29] Ishikawa A, Takata T, Kondo J N, et al. Oxysulfide $Sm_2Ti_2S_2O_5$ as a stable photocatalyst for water oxidation and reduction under visible light irradiation ($\lambda \leq$ 650 nm). Journal of the American Chemical Society, **2002**, 124(45): 13547-13553.

[30] Ohmori T, Takahashi H, Mametsuka H, et al. Photocatalytic oxygen evolution on α-Fe_2O_3 films using Fe^{3+} ion as a sacrificial oxidizing agent. Physical Chemistry Chemical Physics, **2000**, 2(15): 3519-3522.

[31] Cappel U B, Moia D, Bruno A, et al. Evidence for photo-induced charge separation between dye molecules adsorbed to aluminium oxide surfaces. Scientific reports, **2016**, 6: 21276.

[32] Jensen I J T, Ulyashin A G, Løvvik O M. Direct-to-indirect bandgap transitions in ⟨110⟩ SiNWs. Journal of Applied Physics, **2016**, 119(1): 015702.

[33] Barajas-Aguilar A H, Irwin J C, Garay-Tapia A M, et al. Crystalline structure, electronic and lattice-dynamics properties of $NbTe_2$. Scientific reports, **2018**, 8(1): 16984.

[34] Chen J, Wu G, Wang T, et al. Carrier step-by-step transport initiated by precise defect distribution engineering for efficient photocatalytic hydrogen generation. ACS applied materials & interfaces, **2017**, 9(5): 4634-4642.

[35] Droseros N, Longo G, Brauer J C, et al. Origin of the Enhanced Photoluminescence Quantum Yield in $MAPbBr_3$ Perovskite with Reduced Crystal Size. ACS energy letters, **2018**, 3(6): 1458-1466.

[36] Joyce H J, Baig S A, Parkinson P, et al. The influence of surfaces on the transient terahertz conductivity and electron mobility of GaAs nanowires. Journal of Physics D: Applied Physics, **2017**, 50(22): 224001.

[37] Shklovskii B I, Efros A L. Electronic properties of doped semiconductors . Springer Science & Business Media, **2013**.

[38] Venturi G, Castaldini A, Schleusener A, et al. Electronic levels in silicon MaWCE nanowires: evidence of a limited diffusion of Ag. Nanotechnology, **2015**, 26(42): 425702.

[39] Sivakov V, Andrä G, Gösele U, et al. Epitaxial vapor–liquid–solid growth of silicon nano-whiskers by electron beam evaporation. physica status solidi (a), **2006**, 203(15): 3692-3698.

[40] Eisenhawer B, Sivakov V, Christiansen S, et al. A time-resolved numerical study of the vapor-liquid-solid growth kinetics describing the initial nucleation phase as well as pulsed deposition processes. Nano letters, **2013**, 13(3): 873-883.

[41] Suzuki H, Araki H, Tosa M, et al. Formation of silicon nanowires by CVD using gold catalysts at low temperatures. Materials transactions, **2007**: 0707090083-0707090083.

[42] Yang Y H, Wu S J, Chiu H S, et al. Catalytic growth of SiNWs assisted by laser ablation. The Journal of Physical Chemistry B, **2004**, 108(3): 846-852.

[43] Al-Salman R, Mallet J, Molinari M, et al. Template assisted electrodeposition of germanium and silicon nanowires in an ionic liquid. Physical chemistry chemical physics, **2008**, 10(41): 6233-6237.

[44] Sivakov V, Andrä G, Himcinschi C, et al. Growth peculiarities during vapor–liquid–solid growth of silicon nanowhiskers by electron-beam evaporation. Applied Physics A, **2006**, 85(3): 311-315.

[45] Eisenhawer B, Sivakov V, Christiansen S, et al. A time-resolved numerical study of the vapor-liquid-solid growth kinetics describing the initial nucleation phase as well as pulsed deposition processes. Nano letters, **2013**, 13(3): 873-883.

[46] Allen J E, Hemesath E R, Perea D E, et al. High-resolution detection of Au catalyst atoms in Si nanowires. Nature nanotechnology, **2008**, 3(3): 168.

[47] Wagner C. Theorie der alterung von niederschlägen durch umlösen (Ostwald-reifung). Zeitschrift für Elektrochemie, Berichte der Bunsengesellschaft für physikalische Chemie, **1961**, 65(7-8): 581-591.

[48] Lifshitz I M, Slyozov V V. The kinetics of precipitation from supersaturated solid solutions. Journal of physics and chemistry of solids, **1961**, 19(1-2): 35-50.

[49] Hannon J B, Kodambaka S, Ross F M, et al. The influence of the surface migration of gold on the growth of silicon nanowires. nature, **2006**, 440(7080): 69.

[50] Wittemann J V, Münchgesang W, Senz S, et al. Silver catalyzed ultrathin silicon nanowires grown by low-temperature chemical-vapor-deposition. **2010**.

[51] Hochbaum A I, Fan R, He R, et al. Controlled growth of Si nanowire arrays for device integration. Nano letters, **2005**, 5(3): 457-460.

[52] Hoffmann S, Bauer J, Ronning C, et al. Axial pn junctions realized in silicon nanowires by ion implantation. Nano letters, **2009**, 9(4): 1341-1344.

[53] Grigoropoulos S, Gogolides E, Tserepi A D, et al. Highly anisotropic silicon reactive ion etching for nanofabrication using mixtures of SF_6/CHF_3 gases. Journal of Vacuum Science & Technology B: Microelectronics and Nanometer Structures Processing, Measurement, and Phenomena, **1997**, 15(3): 640-645.

[54] Gonchar K A, Osminkina L A, Sivakov V, et al. Optical properties of nanowire structures produced by the metal-assisted chemical etching of lightly doped silicon crystal wafers. Semiconductors, **2014**, 48(12): 1613-1618.

[55] To W K, Tsang C H, Li H H, et al. Fabrication of n-type mesoporous SiNWs by one-step etching. Nano letters, **2011**, 11(12): 5252-5258.

[56] Choi H J, Baek S, Jang H S, et al. Optimization of metal-assisted chemical etching process in fabrication of p-type silicon wire arrays. Current Applied Physics, **2011**, 11(1): S25-S29.

[57] To W K, Tsang C H, Li H H, et al. Fabrication of n-type mesoporous SiNWs by one-step etching. Nano letters, **2011**, 11(12): 5252

[58] Aouida S, Zaghouani R B, Bachtouli N, et al. Hydrogen passivation of silicon nanowire structures. Applied Surface Science, **2016**, 370: 49-52.

[59] Peng K Q, Hu J J, Yan Y J, et al. Fabrication of single-crystalline SiNWs by scratching a silicon surface with catalytic metal particles. Advanced Functional Materials, **2006**, 16(3): 387-394.

[60] Bahruji H, Bowker M, Davies P R. Photoactivated reaction of water with silicon nanoparticles. International Journal of Hydrogen Energy, **2009**, 34(20): 8504-8510.

[61] Litvinenko S, Alekseev S, Lysenko V, et al. Hydrogen production from nano-porous Si powder formed by stain etching. International journal of hydrogen energy, **2010**, 35(13): 6773-6778.

[62] Shen P, Uesawa N, Inasawa S, et al. Stable and color-tunable fluorescence from silicon nanoparticles formed by single-step plasma assisted decomposition of $SiBr_4$. Journal of Materials Chemistry, **2010**, 20(9): 1669-1675.

[63] English D S, Pell L E, Yu Z, et al. Size tunable visible luminescence from individual organic monolayer stabilized silicon nanocrystal quantum dots. Nano Letters, **2002**, 2(7): 681-685.

[64] Hessel C M, Henderson E J, Veinot J G C. Hydrogen silsesquioxane: a molecular precursor for nanocrystalline Si-SiO_2 composites and freestanding hydride-surface-terminated silicon nanoparticles. Chemistry of materials, **2006**, 18(26): 6139-6146.

[65] Tilley R D, Yamamoto K. The microemulsion synthesis of hydrophobic and hydrophilic silicon nanocrystals. Advanced Materials, **2006**, 18(15): 2053-2056.

[66] Hofmeister H, Huisken F, Kohn B. Lattice contraction in nanosized silicon particles produced by laser pyrolysis of silane. The European Physical Journal D-Atomic, Molecular, Optical and Plasma Physics, **1999**, 9(1): 137-140.

[67] Meier C, Gondorf A, Lüttjohann S, et al. Silicon nanoparticles: Absorption, emission, and the nature of the electronic bandgap. Journal of Applied Physics, **2007**, 101(10): 103112.

[68] Dimova-Malinovska D, Sendova-Vassileva M, Tzenov N, et al. Preparation of thin porous silicon layers by stain etching. Thin Solid Films, **1997**, 297(1-2): 9-12.

[69] Li X, Bohn P W. Metal-assisted chemical etching in HF/H_2O_2 produces porous silicon. Applied Physics Letters, **2000**, 77(16): 2572-2574.

[70] Tsujino K, Matsumura M. Boring deep cylindrical nanoholes in silicon using silver nanoparticles as a catalyst. Advanced Materials, **2005**, 17(8): 1045-1047.

[71] To W K, Tsang C H, Li H H, et al. Fabrication of n-type mesoporous SiNWs by one-step etching. Nano letters, **2011**, 11(12): 5252-5258.

[72] Qu Y, Liao L, Li Y, et al. Electrically conductive and optically active porous SiNWs. Nano letters, **2009**, 9(12): 4539-4543.

[73] Peng K Q, Yan Y J, Gao S P, et al. Synthesis of large-area silicon nanowire arrays via self-assembling nanoelectrochemistry. Advanced materials, **2002**, 14(16): 1164-1167.

[74] Li S, Ma W, Zhou Y, et al. Fabrication of porous SiNWs by MACE method in $HF/H_2O_2/AgNO_3$ system at room temperature. Nanoscale research letters, **2014**, 9(1): 196.

[75] Sivakov V A, Bronstrup G, Pecz B, et al. Realization of vertical and zigzag single crystalline silicon nanowire architectures. The Journal of Physical Chemistry C, **2010**, 114(9): 3798-3803.

[76] Hannon J B, Kodambaka S, Ross F M, et al. The influence of the surface migration of gold on the growth of silicon nanowires. nature, **2006**, 440(7080): 69.

[77] Park S Y, Di Giacomo S J, Anisha R, et al. Fabrication of nanowires with high aspect ratios utilized by dry etching with SF_6: C_4F_8 and self-limiting thermal oxidation on Si substrate. Journal of Vacuum Science & Technology B, Nanotechnology and Microelectronics: Materials, Processing, Measurement, and Phenomena, **2010**, 28(4): 763-768.

[78] Nanowires: Recent Advances. BoD–Books on Demand, **2012**.

[79] Lin L, Guo S, Sun X, et al. Synthesis and photoluminescence properties of porous silicon nanowire arrays. Nanoscale research letters, **2010**, 5(11): 1822.

[80] Fazio B, Artoni P, Iatì M A, et al. Strongly enhanced light trapping in a two-dimensional silicon nanowire random fractal array. Light: Science & Applications, **2016**, 5(4): e16062.

[81] Yao D, Zhang G, Li B. A universal expression of band gap for silicon nanowires of different cross-section geometries. Nano Letters, **2008**, 8(12): 4557-4561.

[82] Sun X H, Wang S D, Wong N B, et al. FTIR spectroscopic studies of the stabilities and reactivities of hydrogen-terminated surfaces of silicon nanowires. Inorganic chemistry, **2003**, 42(7): 2398-2404.

[83] Tian B, Zheng X, Kempa T J, et al. Coaxial silicon nanowires as solar cells and nanoelectronic power sources. nature, **2007**, 449(7164): 885.

[84] Garnett E C, Yang P. Silicon nanowire radial p-n junction solar cells. Journal of the American Chemical Society, **2008**, 130(29): 9224-9225.

[85] Priolo F, Gregorkiewicz T, Galli M, et al. Silicon nanostructures for photonics and photovoltaics. Nature nanotechnology, **2014**, 9(1): 19.

[86] Adachi M M, Anantram M P, Karim K S. Core-shell silicon nanowire solar cells. Scientific reports, **2013**, 3: 1546.

[87] Sivakov V, Andrä G, Gawlik A, et al. Silicon nanowire-based solar cells on glass: synthesis, optical properties, and cell parameters. Nano letters, **2009**, 9(4): 1549-1554.

[88] Shao M W, Shan Y Y, Wong N B, et al. Silicon nanowire sensors for bioanalytical applications: glucose and hydrogen peroxide detection. Advanced Functional Materials, **2005**, 15(9): 1478-1482.

[89] Ahn J H, Yun J, Moon D I, et al. Self-heated SiNWs for high performance hydrogen gas detection. Nanotechnology, **2015**, 26(9): 095501.

[90] Shehada N, Cancilla J C, Torrecilla J S, et al. Silicon nanowire sensors enable diagnosis of patients via exhaled breath. ACS nano, **2016**, 10(7): 7047-7057.

[91] Venturi G, Castaldini A, Schleusener A, et al. Electronic levels in silicon MaWCE nanowires: evidence of a limited diffusion of Ag. Nanotechnology, **2015**, 26(42): 425702.

[92] Venturi G, Castaldini A, Schleusener A, et al. Influence of surface pre-treatment on the electronic levels in silicon MaWCE nanowires. Nanotechnology, **2015**, 26(19): 195705.

[93] Garnett E, Yang P. Light trapping in silicon nanowire solar cells. Nano letters, **2010**, 10(3): 1082-1087.

[94] Nolan M, O'Callaghan S, Fagas G, et al. Silicon nanowire band gap modification. Nano letters, **2007**, 7(1): 34-38.

[95] Dai P, Xie J, Mayer M T, et al. Solar hydrogen generation by SiNWs modified with platinum nanoparticle catalysts by atomic layer deposition. Angewandte Chemie International Edition, **2013**, 52(42): 11119-11123.

[96] Liu D, Li L, Gao Y, et al. The nature of photocatalytic “water splitting” on SiNWs. Angewandte Chemie International Edition, **2015**, 54(10): 2980-2985.

[97] Oh I, Kye J, Hwang S. Enhanced photoelectrochemical hydrogen production from silicon nanowire array photocathode. Nano letters, **2011**, 12(1): 298-302.

[98] Liu C, Tang J, Chen H M, et al. A fully integrated nanosystem of semiconductor nanowires for direct solar water splitting. Nano letters, **2013**, 13(6): 2989-2992.

[99] Linsebigler A L, Lu G, Yates Jr J T. Photocatalysis on TiO_2 surfaces: principles, mechanisms, and selected results. Chemical reviews, **1995**, 95(3): 735-758.

[100] Wang F Y, Yang Q D, Xu G, et al. Highly active and enhanced photocatalytic silicon nanowire arrays. Nanoscale, **2011**, 3(8): 3269-3276.

[101] Yamada Y M A, Yuyama Y, Sato T, et al. A Palladium-Nanoparticle and Silicon-Nanowire-Array Hybrid: A Platform for Catalytic Heterogeneous Reactions. Angewandte Chemie International Edition, **2014**, 53(1): 127-131.

[102] Zhang R Q, Liu X M, Wen Z, et al. Prediction of silicon nanowires as photocatalysts for water splitting: band structures calculated using density functional theory. The Journal of Physical Chemistry C, **2011**, 115(8): 3425-3428.

[103] Dai F, Zai J, Yi R, et al. Bottom-up synthesis of high surface area mesoporous crystalline silicon and evaluation of its hydrogen evolution performance. Nature communications, **2014**, 5: 3605.

[104] Jang Y J, Ryu J, Hong D, et al. A multi-stacked hyperporous silicon flake for highly active solar hydrogen production. Chemical Communications, **2016**, 52(67): 10221-10224.

[105] Ryu J, Jang Y J, Choi S, et al. All-in-one synthesis of mesoporous silicon nanosheets from natural clay and their applicability to hydrogen evolution. NPG Asia Materials, **2016**, 8(3): e248.

[106] Liu D, Li L, Gao Y, et al. The nature of photocatalytic “water splitting” on silicon nanowires. Angewandte Chemie International Edition, **2015**, 54(10): 2980-2985.

[107] Song H, Liu D, Yang J, et al. Highly crystalline mesoporous silicon spheres for efficient visible photocatalytic hydrogen evolution. ChemNanoMat, **2017**, 3(1): 22-26.

[108] Tian Y, Tatsuma T. Mechanisms and applications of plasmon-induced charge separation at TiO2 films loaded with gold nanoparticles. Journal of the American Chemical Society, **2005**, 127(20): 7632-7637.

[109] Li J, Cushing S K, Zheng P, et al. Plasmon-induced photonic and energy-transfer enhancement of solar water splitting by a hematite nanorod array. Nature communications, **2013**, 4: 2651.

[110] Erogbogbo F, Lin T, Tucciarone P M, et al. On-demand hydrogen generation using nanosilicon: splitting water without light, heat, or electricity. Nano letters, **2013**, 13(2): 451-456.

[111] Oh I, Kye J, Hwang S. Enhanced photoelectrochemical hydrogen production from silicon nanowire array photocathode. Nano letters, **2011**, 12(1): 298-302.

[112] Meier C, Gondorf A, Lüttjohann S, et al. Silicon nanoparticles: Absorption, emission, and the nature of the electronic bandgap. Journal of Applied Physics, **2007**, 101(10): 103112.

[113] Boettcher S W, Warren E L, Putnam M C, et al. Photoelectrochemical hydrogen evolution using Si microwire arrays. Journal of the American Chemical Society, **2011**, 133(5): 1216-1219.

[114] Dai P, Xie J, Mayer M T, et al. Solar hydrogen generation by silicon nanowires modified with platinum nanoparticle catalysts by atomic layer deposition. Angewandte Chemie International Edition, **2013**, 52(42): 11119-11123.

[115] Seger B, Laursen A B, Vesborg P C K, et al. Hydrogen production using a molybdenum sulfide catalyst on a titanium-protected n^+ p-silicon photocathode. Angewandte Chemie International Edition, **2012**, 51(36): 9128-9131.

[116] Kenney M J, Gong M, Li Y, et al. High-performance silicon photoanodes passivated with ultrathin nickel films for water oxidationScience, **2013**, 342(6160): 836-840.

[117] Fan R, Mi Z, Shen M. Silicon based photoelectrodes for photoelectrochemical water splitting. Optics express, **2019**, 27(4): A51-A80.

[118] Chen Y W, Prange J D, Dühnen S, et al. Atomic layer-deposited tunnel oxide stabilizes silicon photoanodes for water oxidation. Nature Materials, **2011**, 10(7): 539.

[119] Sivakov V, Voigt F, Hoffmann B, et al. Wet-chemically etched silicon nanowire architectures: formation and properties. Nanowires-Fundamental Research. Dr. Abbass Hashim (Ed.), **2011**: 45-80.

[120] Ming T, Schleusener A, Yermukhamed D, et al. Silver mirror reaction as a simple method for silicon nanowires functionalization[J]. Materials Research Express, 2019, 6(10): 105057.

[121] López R, Gómez R. Band-gap energy estimation from diffuse reflectance measurements on sol-gel and commercial TiO_2: a comparative study. Journal of sol-gel science and technology, **2012**, 61(1): 1-7.

[122] Kubelka P. New contributions to the optics of intensely light-scattering materials. Part I. Josa, **1948**, 38(5): 448-457.

[123] Stuart B. Infrared spectroscopy. Kirk-Othmer Encyclopedia of Chemical Technology, **2000**: 1-18.

[124] Hsu C P S. Infrared spectroscopy. Handbook of instrumental techniques for analytical chemistry, **1997**, 247: 277.

[125] Goldstein J I, Newbury D E, Michael J R, et al. Scanning electron microscopy and X-ray microanalysis. Springer, **2017**.

[126] Reimer L. Scanning electron microscopy: physics of image formation and microanalysis. Springer, **2013**.

[127] Cheville N F, Stasko J. Techniques in electron microscopy of animal tissue. Veterinary pathology, **2014**, 51(1): 28-41.

[128] Patterson A L. The Scherrer formula for X-ray particle size determination. Physical Review, **1939**, 56(10): 978.

[129] Koh K, Wong-Foy A G, Matzger A J. A porous coordination copolymer with over 5000 m^2/g BET surface area. Journal of the American chemical society, **2009**, 131(12): 4184-4185.

[130] McNair H M, Miller J M. Basic gas chromatography. John Wiley & Sons, **2011**.

[131] Jennings W, Mittlefehldt E, Stremple P. Analytical gas chromatography. Academic Press, **1997**.

[132] Cruz S, Hönig-d'Orville A, Müller J. Fabrication and optimization of porous silicon substrates for diffusion membrane applications. Journal of the Electrochemical Society, **2005**, 152(6): C418-C424.

[133] Canevali C, Alia M, Fanciulli M, et al. Influence of doping elements on the formation rate of silicon nanowires by silver-assisted chemical etching. Surface and Coatings Technology, **2015**, 280: 37-42.

[134] Lai R A, Hymel T M, Narasimhan V K, et al. Schottky barrier catalysis mechanism in metal-assisted chemical etching of silicon. ACS applied materials & interfaces, **2016**, 8(14): 8875-8879.

[135] Lin L, Guo S, Sun X, et al. Synthesis and photoluminescence properties of porous silicon nanowire arrays. Nanoscale research letters, **2010**, 5(11): 1822.

[136] Kanamori Y, Hane K, Sai H, et al. 100 nm period silicon antireflection structures fabricated using a porous alumina membrane mask. Applied Physics Letters, **2001**, 78(2): 142-143.

[137] Peng K Q, Lee S T. Silicon nanowires for photovoltaic solar energy conversion. Advanced Materials, **2011**, 23(2): 198-215.

[138] Li H, Jia R, Chen C, et al. Influence of nanowires length on performance of crystalline silicon solar cell. Applied Physics Letters, **2011**, 98(15): 151116.

[139] Boettcher S W, Warren E L, Putnam M C, et al. Photoelectrochemical hydrogen evolution using Si microwire arrays. Journal of the American Chemical Society, **2011**, 133(5): 1216-1219.

[140] Dadwal U, Ali D, Singh R. Silicon-silver dendritic nanostructures for the enhanced photoelectrochemical splitting of natural water. International Journal of Hydrogen Energy, **2018**, 43(51): 22815-22826.

[141] Casiello M, Picca R, Fusco C, et al. Catalytic activity of silicon nanowires decorated with gold and copper nanoparticles deposited by pulsed laser ablation. Nanomaterials, **2018**, 8(2): 78.

[142] Hua J, Shao M, Cheng L, et al. The fabrication of silver-modified silicon nanowires and their excellent catalysis in the decomposition of fluorescein sodium. Journal of Physics and Chemistry of Solids, **2009**, 70(1): 192-196.

[143] Liqiang J, Dejun W, Baiqi W, et al. Effects of noble metal modification on surface oxygen composition, charge separation and photocatalytic activity of ZnO nanoparticles. Journal of Molecular Catalysis A: Chemical, **2006**, 244(1-2): 193-200.

[144] Tian Y, Tatsuma T. Mechanisms and applications of plasmon-induced charge separation at TiO_2 films loaded with gold nanoparticles. Journal of the American Chemical Society, **2005**, 127(20): 7632-7637.

[145] Yuan H, Ma W, Chen C, et al. Shape and SPR evolution of thorny gold nanoparticles promoted by silver ions. Chemistry of materials, **2007**, 19(7): 1592-1600.

[146] Li J, Cushing S K, Zheng P, et al. Plasmon-induced photonic and energy-transfer enhancement of solar water splitting by a hematite nanorod array. Nature communications, **2013**, 4: 2651.

[147] Dai P, Xie J, Mayer M T, et al. Solar hydrogen generation by silicon nanowires modified with platinum nanoparticle catalysts by atomic layer deposition. Angewandte Chemie International Edition, **2013**, 52(42): 11119-11123.

[148] Zhu L, Cai Q, Liao F, et al. Ru-modified silicon nanowires as electrocatalysts for hydrogen evolution reaction. Electrochemistry Communications, **2015**, 52: 29-33.

[149] Dadwal U, Ali D, Singh R. Silicon-silver dendritic nanostructures for the enhanced photoelectrochemical splitting of natural water. International Journal of Hydrogen Energy, **2018**, 43(51): 22815-22826.

[150] Yin J, Qi X, Yang L, et al. A hydrogen peroxide electrochemical sensor based on silver nanoparticles decorated silicon nanowire arrays. Electrochimica Acta, **2011**, 56(11): 3884-3889.

[151] Liu K, Qu S, Zhang X, et al. Improved photovoltaic performance of silicon nanowire/organic hybrid solar cells by incorporating silver nanoparticles. Nanoscale research letters, **2013**, 8(1): 88.

[152] Ershov B G, Janata E, Henglein A. Growth of silver particles in aqueous solution: long-lived "magic" clusters and ionic strength effects. The Journal of Physical Chemistry, **1993**, 97(2): 339-343.

[153] Chen Y, Guo L, Chen F, et al. Synthesis and characterization of crystalline films on silicon. Journal of Physics: Condensed Matter, **1996**, 8(45): L685.

[154] Janata E. Structure of the trimer silver cluster Ag_3^{2+}. The Journal of Physical Chemistry B, **2003**, 107(30): 7334-7336.

[155] Gong J, Dai R, Wang Z, et al. Thickness dispersion of surface plasmon of ag nano-thin films: determination by ellipsometry iterated with transmittance method. Scientific reports, **2015**, 5: 9279.

[156] Maurel C, Cardinal T, Bellec M, et al. Luminescence properties of silver zinc phosphate glasses following different irradiations. Journal of Luminescence, **2009**, 129(12): 1514-1518.

[157] Montini T, Gombac V, Sordelli L, et al. Nanostructured Cu/TiO_2 Photocatalysts for H2 Production from Ethanol and Glycerol Aqueous Solutions. ChemCatChem, **2011**, 3(3): 574-577.

[158] Gallo A, Marelli M, Psaro R, et al. Bimetallic Au–Pt/TiO_2 photocatalysts active under UV-A and simulated sunlight for H_2 production from ethanol. Green Chemistry, **2012**, 14(2): 330-333.

[159] Beltram A, Romero-Ocana I, Jaen J J D, et al. Photocatalytic valorization of ethanol and glycerol over TiO_2 polymorphs for sustainable hydrogen production. Applied Catalysis A: General, **2016**, 518: 167-175.

[160] Lalitha K, Reddy J K, Sharma M V P, et al. Continuous hydrogen production activity over finely dispersed Ag_2O/TiO_2 catalysts from methanol: water mixtures under solar irradiation: a structure-activity correlation. International Journal of hydrogen energy, **2010**, 35(9): 3991-4001.

[161] Melián E P, López C R, Santiago D E, et al. Study of the photocatalytic activity of Pt-modified commercial TiO_2 for hydrogen production in the presence of common organic sacrificial agents. Applied Catalysis A: General, **2016**, 518: 189-197.

[162] Pilkenton S, Hwang S J, Raftery D. Ethanol photocatalysis on TiO_2-coated optical microfiber, supported monolayer, and powdered catalysts: An in situ NMR study. The Journal of Physical Chemistry B, **1999**, 103(50): 11152-11160. Catalysis A: General, **2016**, 518: 167-175.

[163] Ali N K, Hashim M R, Aziz A A. Effects of surface passivation in porous silicon as H2 gas sensor. Solid-State Electronics, **2008**, 52(7): 1071-1074.

[164] Shiu S C, Lin S B, Hung S C, et al. Influence of pre-surface treatment on the morphology of silicon nanowires fabricated by metal-assisted etching. Applied surface science, **2011**, 257(6): 1829-1834.

[165] Wang F Y, Yang Q D, Xu G, et al. Highly active and enhanced photocatalytic silicon nanowire arrays. Nanoscale, **2011**, 3(8): 3269-3276.

[166] Erogbogbo F, Lin T, Tucciarone P M, et al. On-demand hydrogen generation using nanosilicon: splitting water without light, heat, or electricity. Nano letters, **2013**, 13(2): 451-456.

[167] Kashkarov P K, Konstantinova E A, Matveeva A B, et al. Photovoltage and photo-induced charge trapping in porous silicon. Applied Physics A, **1996**, 62(6): 547-551.

[168] Khalilov U, Pourtois G, Duin A C T, et al. Self-limiting oxidation in small-diameter Si nanowires. Chemistry of materials, **2012**, 24(11): 2141-2147.

[169] Stöhr J. NEXAFS spectroscopy. Springer Science & Business Media, **2013**.

[170] Li D, Bancroft G M, Kasrai M, et al. X-ray absorption spectroscopy of silicon dioxide (SiO_2) polymorphs: The structural characterization of opal. American Mineralogist, **1994**, 79(7-8): 622-632.

[171] Sham T K, Coulthard I. Edge-jump inversion in the Si L3, 2-edge optical XAFS of porous silicon. Journal of synchrotron radiation, **1999**, 6(3): 215-216.

[172] Turishchev S Y, Terekhov V A, Kashkarov V M, et al. Investigations of the electron energy structure and phase composition of porous silicon with different porosity. Journal of electron spectroscopy and related phenomena, **2007**, 156: 445-451.

[173] Turishchev S Y, Parinova E V, Pisliaruk A K, et al. Surface deep profile synchrotron studies of mechanically modified top-down silicon nanowires array using ultrasoft X-ray absorption near edge structure spectroscopy. Scientific reports, **2019**, 9(1): 8066.

[174] Higashi G S, Chabal Y J, Trucks G W, et al. Ideal hydrogen termination of the Si (111) surface. Applied physics letters, **1990**, 56(7): 656-658.

[175] Lisovskii I P, Litovchenko V G, Lozinskii V B, et al. IR study of short-range and local order in SiO_2 and SiO_x films. Journal of non-crystalline solids, **1995**, 187: 91-95.

[176] Mori H, Miyamura Y, Endo T. Synthesis and characterization of water-soluble $SiO_{1.5}/TiO_2$ hybrid nanoparticles by hydrolytic co-condensation of triethoxysilane containing hydroxyl groups. Materials Chemistry and Physics, **2009**, 115(1): 287-295.

[177] Liao W S, Lee S C. Water-induced room-temperature oxidation of Si-H and -Si-Si- bonds in silicon oxide. Journal of applied physics, **1996**, 80(2): 1171-1176.

[178] Miyazaki S, Nishimura H, Fukuda M, et al. Structure and electronic states of ultrathin SiO_2 thermally grown on Si (100) and Si (111) surfaces. Applied surface science, **1997**, 113: 585-589.

[179] Shabalina A V, Izaak T I, Kharlamova T S, et al. Ag/SiO_x nanocomposite powders synthesized from colloids obtained by pulsed laser ablation. Colloids and Surfaces A: Physicochemical and Engineering Aspects, **2018**, 553: 80-88.

[180] Liao W S, Lee S C. Water-induced room-temperature oxidation of Si-H and-Si-Si-bonds in silicon oxide. Journal of applied physics, **1996**, 80(2): 1171-1176.

[181] Shabalov A L, Feldman M S. Optical and dielectric properties of thin SiO_x films of variable composition. Thin Solid Films, **1983**, 110(3): 215-224.

[182] Sella C, Chenot S, Reillon V, et al. Influence of the deposition conditions on the optical absorption of Ag-SiO_2 nanocermet thin films. Thin Solid Films, **2009**, 517(20): 5848-5854.